ALMA MATER STUDORIUM UNIVERSITÀ DI BOLOGNA

DOTTORATO DI RICERCA IN
ASTROFISICA

Ciclo XXXV

New Indicators of Star Cluster Dynamical Evolution

Presentata da: **Bhavana Bhat**

Coordinatore Dottorato:

Prof. Andrea Miglio

Supervisore:

Prof. Barbara Lanzoni

Co-supervisori:

Prof. Francesco R. Ferraro

Prof. Enrico Vesperini

Esame finale anno 2023

Settore Concorsuale: 02/C1 – Astronomia, Astrofisica, Fisica della Terra e dei Pianeti
Settore Scientifico Disciplinare: FIS/05 – Astronomia e Astrofisica

Abstract

In this thesis, we analyse a set of Monte Carlo simulations of globular clusters (GCs) with the aim to define new empirical parameters measurable from observations and able to trace the different phases of their dynamical evolution history. During the long-term dynamical evolution of collisional stellar systems, due to processes as mass segregation and dynamical friction, massive stars sink to the core of the cluster, losing their kinetic energy to low mass stars which move to the envelope. This eventually deprives the core of kinetic energy leading to Core Collapse (CC), an event where the density at the centre formally increases. to infinity. This runaway process is thought to be halted by hard binary systems, which act as heating sources, and it is followed by a post-CC phase of gravothermal oscillations, where the core undergoes cyclic expansions and contractions. Clearly, such an internal dynamical evolution corresponds to significant variations also of the structure of the system. However, a number of different factors, such as the central density, the primordial binary fraction, the content of dark remnants (black holes and neutron stars), the effects of an external tidal field, and so on, affect in a significant and complex way the time scales of the different phases of dynamical evolution, implying that clusters with same chronological (stellar) age can have different dynamical ages. In turn, the knowledge of the chronological age alone does not allow the correct and complete physical interpretation of star clusters, therefore calling for methods able to determine the stage of dynamical evolution they reached so far.

Until now, the classification of CC and post-CC clusters is mainly based on the detection of a central density cusp strongly deviating from the (flat, core-like) King model profile, which is usually adopted to reproduce the observed density distributions of GCs. However, the reliability of this diagnostic is limited by the fact that the central density cusp may diminish during post-CC gravothermal oscillations, or due to the “heating" effect of binary systems (which are known to reduce the "intensity" of CC), thus making difficult its detection through observations. Only a small percentage (15-20%) of Galactic GCs exhibit a central cusp in their star density profile and are thus classified as post-CC, despite the central relaxation time being shorter than their age in most cases. Other diagnostics of GC internal dynamics have been recently proposed in the literature, but their operational determination generally requires time-expensive and challenging observations (such as the measure of orbital anisotropy or the velocity dispersion profile of different stellar mass groups, the stellar mass function at different radial distances from the center, the quantification of central segregation of blue straggler stars), which can even be un-

feasible with the current generation of instruments, especially for the most distant and concentrated systems.

This thesis is thus devoted to define new indicators of dynamical evolution that are both reliable and relatively easy to determine from observed data. To this aim, we ran a large set of Monte Carlo simulations of GCs starting from different initial conditions (such as initial number of particles, compactness of the system, galactocentric distance, primordial binary fraction, and prescriptions for the retention of stellar-mass black holes). We first analyzed several time snapshots extracted at at various chronological (and dynamical) evolutionary ages from a few (five) runs. Then, we concentrated on a sample of snapshots all extracted at 13 Gyr from 46 different simulations, to mimic the population of Galactic GCs, which are essentially coeval (with chronological ages of 12-13 Gyr), but are evolving in different evolutionary stages. With the purpose to define parameters useful for observational studies, the analysis has been performed from the point of view of an observer. For instance, each simulated cluster has been projected onto a 2D plane, the binary systems have been treated as "stellar blends" (consistently with the fact that the two components cannot be individually resolved at the distances of Galactic GCs), and only stars brighter than ~ 1 magnitude below the main sequence turnoff point have been considered. The density profile has been determined as in observational works, from the number of stars per unit area at different distances from the center, and then fit with the King model family (which also provided us with a measure of the tridimensional half-mass radius of the cluster, r_h).

We thus investigated the normalized cumulative radial distribution (nCRD) drawn by all the (bright) cluster stars included within a projected distance from the center $R = 0.5r_h$, finding that its morphology varies in time (it becomes progressively steeper) according to the cluster's dynamical stage. To quantify these changes we defined three parameters: A_5, the area subtended by the nCRD within 5% of the half-mass radius, P_5, the value of the nCRD measured at the same distance, and $S_{2.5}$, the slope of the straight line tangent to the nCRD measured at $R = 2.5\%r_h$.

The analysis of different time snapshots extracted from the same simulation revealed that the three parameters evolve following the cluster's (chronological and) dynamical evolution: after an early phase in which they are essentially constant, their values rapidly increase, reach their maximum at the CC epoch, and slightly decrease in the post-CC phase, when they show some fluctuations but remains significantly larger than at the beginning. The progressive increase of the nCRD parameters is milder in simulations with non-zero primordial binary fraction. This is in agreement with the expectations, because binaries are known to make the gradual contraction of the cluster becomes milder and CC shallower. Nevertheless, the cluster dynamical evolution is still properly traced by the three parameters. For models with a larger initial retention of stellar mass BHs the evolution depends on the timescale of their subsequent dynamical ejection. An early dynamical ejection of BHs results in a long-term evolution of the three parameters similar to that found in systems with

no initial BH retention. Conversely, in the model that retains a large number of BHs for extended time (slow dynamical ejection of BHs), the system is characterized by a less concentrated structure and by the lack of significant temporal evolution of the three parameters which show constant values smaller than those observed in all the previous simulations. The smaller values of the three parameters found in this case might be used to indirectly infer the possible presence of BHs in the cluster.

The analysis of the large sample of 13 Gyr old snapshots extracted from simulations run from different initial conditions confirm that the nCRD parameters defined in this work are able to distinguish the majority of dynamically-young clusters, from dynamically-old systems. In fact, the latter show much higher values of A_5, P_5 and $S_{2.5}$ than the clusters in early stages of dynamical evolution, and even in excess than what expected from the King models that best fit their projected density profiles. The heating effect of stellar-mass and intermediate-mass black holes, which substantially delays CC, is fully confirmed by this analysis: all the corresponding snapshots have low values of the three parameters, indicating young dynamical ages. In a few cases we observe that clusters that, based on the time evolution of its 1% Lagrangian radius, have not reached CC yet but behaves like dynamically evolved systems, with high-intermediate values of the nCRD parameters, always exceeding the King model expectations. Their deeper analysis (in terms, e.g., of their current binary fraction, the epoch of ejection of black holes, the current amount of binaries including compact objects), together with the extension of similar analyses to a larger set of simulations and, especially, to observational data, will likely allow a further refinement of the use of the nCRD parameters as diagnostics of the dynamical stage of dense stellar systems.

Contents

Abstract iii

Contents vii

1 Introduction 1

1.1 Globular Clusters . . . 1

1.1.1 Internal dynamics . . . 1

1.1.2 Long term dynamical evolution . . . 3

1.2 Dynamical Indicators . . . 9

1.2.1 Density cusp . . . 10

1.2.2 Blue Straggler Stars . . . 11

1.3 MOCCA simulations . . . 14

2 New dynamical indicators 17

2.1 Initial Conditions and Methods . . . 17

2.2 Projected density profile . . . 20

2.3 The Normalized Cumulative Radial Distribution . . . 25

2.4 Defining the new parameters . . . 26

2.5 Sensitivity of the parameters to the assumptions . . . 30

2.6 Simulations with different initial conditions . . . 32

2.7 Discussion and summary . . . 33

3 Effect of Initial Binary fraction and Dark Remnants 37

3.1 Methods and Initial conditions . . . 37

3.2 Projected density profiles . . . 40

3.3 The nCRD dynamical indicators . . . 41
3.3.1 Normalised cumulative radial distribution (nCRD) . . . 41
3.3.2 The A_5, P_5 and $S_{2.5}$ parameters . . . 43
3.4 Zooming on the deviations from King models . . . 46
3.5 Effect of dark remnants on the nCRD dynamical indicators . . . 49
3.6 Discussion and summary . . . 50

4 Survey of simulations at 13 Gyr 55
4.1 Methods and Initial Conditions . . . 55
4.2 Comparison of survey simulations with the Harris catalog . . . 57
4.3 nCRD Parameters . . . 60
4.3.1 Construction of nCRD and nCRD parameters . . . 61
4.3.2 Reference models and samples . . . 65
4.3.3 nCRD parameters of survey simulations . . . 66
4.3.4 nCRD parameters as diagnostics of dynamical evolution . . . 72
4.4 Discussion and summary . . . 77

5 Conclusions 79
5.1 Summary . . . 79
5.2 Discussion and Future Perspectives . . . 82

Appendix 84

A NGC 6440 85

Bibliography 107

Chapter 1

Introduction

1.1. Globular Clusters

Globular clusters (GCs) are dense, spherical configurations of $\sim 10^5$ stars that orbit around the center of a galaxy. They are among the oldest systems (e.g., Gratton et al. 1997; Chaboyer 1998) in our universe where stars can be individually observed and are essentially fossils of galaxy formation. Understanding them is crucial to improve our understanding of galaxy formation scenario and conditions in the early universe. We have observed 150 Milky Way GCs (Marín-Franch et al. 2009; Forbes & Bridges 2010; Harris 1996)) aging from 10 to 13 Gyr. They are mainly found in the halo and the bulge of the Galaxy. They experienced only one major burst of star formation, which is confirmed by the homogeneity in iron abundance. Hence, they are ideal laboratories to probe stellar evolutionary theory. [1]High density at the centre of GCs (up to 10^6 stars/pc^3) provides the conditions under which the evolution of stars is gravitationally influenced by the other objects in the system. In fact, due to the close proximity of stars in these dense environments, they are more likely to interact through dynamical processes such as tidal interactions, three body encounters, direct collisions, also triggering the exchange of material in binary systems. These interactions can have a significant impact on stellar evolution, and the long term dynamical evolution of GCs.

1.1.1 Internal dynamics

GCs are ideal cosmic laboratories for understanding multi-body dynamics because of their outstanding densities at the centre, and their proximity to us (allowing

[1]Spectroscopic and photometric evidence of light-element abundance spreads testifies a more complex formation, with subsequent generations of stars formed from the ejecta of a previous population of 4-6 $M_\odot$ objects (see Bastian & Lardo, 2018, for a review) However, this should have happened in a timescale of just a few Myr and does not affect the use of GCs as benchmarks for the stellar evolution theory.

individual stars to be resolved in observations). They are collisional stellar systems, where frequent gravitational interactions among stars significantly alter the overall energy budget, bringing the cluster toward a thermodynamically relaxed state in a timescale (the relaxation time) that can be significantly shorter that its age (eg. Meylan & Heggie, 1997). The two-body relaxation time scale (t_{2b}) is given by (Binney & Tremaine, 1987):

$$t_{2b} = n_{2b} t_{cross}, \tag{1.1}$$

where t_{cross} are crossing time which is the time needed for a typical star to cross the system, and n_{2b} is the number of crossings before the star changes its velocity by a quantity equal to itself, respectively. The relaxation time could be expanded as follows:

$$t_{2b} = \frac{\sigma(r)^3}{8\pi G^2 \langle m \rangle \rho(r) \ln \Lambda}, \tag{1.2}$$

where $\sigma(r)$ is the velocity dispersion at a distance r from the centre, G is the gravitational constant, $\langle m \rangle$ is the mean stellar mass, $\rho(r)$ is the local density and $\ln \Lambda$ is the Coulomb logarithm. This expression could be approximated for a stellar system with N stars with identical mass to:

$$t_{2b} \simeq \frac{0.1N}{\ln N} t_{cross}. \tag{1.3}$$

This represents the time scale needed for a system to completely loss memory of it's initial conditions. In other words, after a time equal to t_{2b} it's no longer possible to derive the velocities or orbits of the stars within the system from the initial conditions such as gravitational potential, or spatial distribution, or velocity dispersion, and so forth. For massive systems like galaxies, where $N \simeq 10^{11}$, the relaxation time is $\sim 10^7$ Gyr, which is far greater than their age. Thus, they are considered as collisionless systems. In the case of systems like GCs, with N $\simeq 10^5 - 10^6$, the relaxation time is less than 1 Gyr which is short in comparison to the age of Galactic GCs (GGCs). This makes star clusters collisional systems on a scale of Hubble time. Hence, stellar encounters play a crucial role in determining the dynamical evolution of GCs and their present-day internal structure. Indeed they have to be taken into account for the physical description of these systems.

From (1.2) it is evident that the relaxation time depends on local quantities, varying between low values in the dense core of GCs, to much larger values towards the tidal radius. Two important quantities used in theoretical and observational studies are the relaxation times defined at core radius (R_c) and at half-mass radius (r_h) of the cluster. The central relaxation time (computed at R_c) is given by (Djorgovski 1993):

$$t_{rc} = 1.491 \times 10^7 yr \frac{k}{\ln(0.4N)} \langle m \rangle^{-1} \rho_{M,0}^{1/2} R_c^3, \tag{1.4}$$

where $k \simeq 0.5592$, and $\rho_{M,0}$ is the central mass density in units of $M_\odot/\mathrm{pc}^{-3}$. The half-mass relaxation time (at $r = r_h$) is given by (Djorgovski 1993):

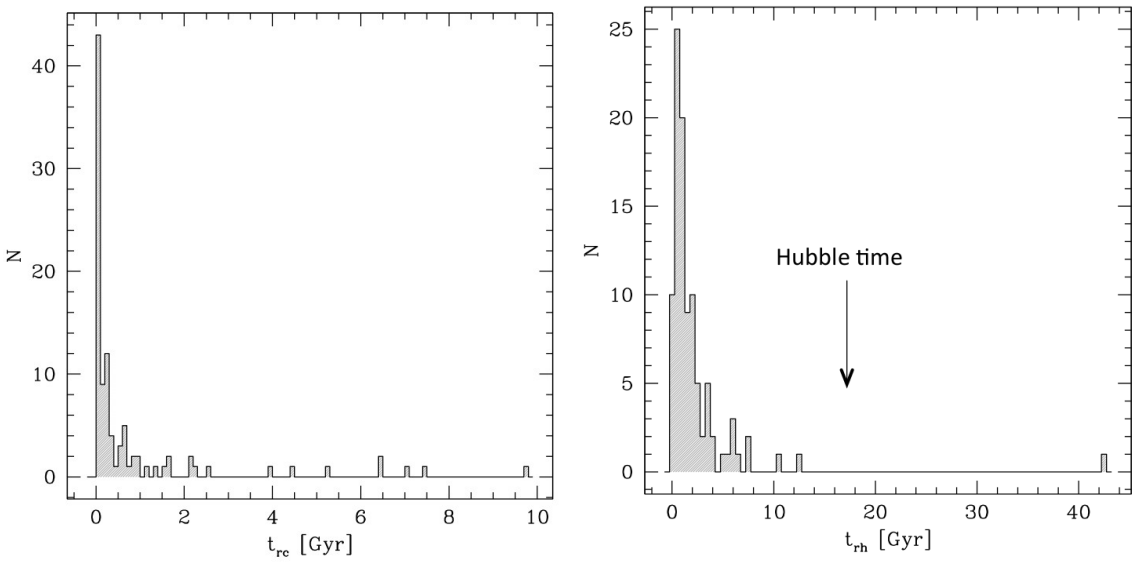

Figure 1.1: Distribution of central and half-mass relaxation times of GGCs (Harris 1996).

$$t_{rh} = 2.055 \times 10^6 yr \frac{1}{\ln(0.4N)} \langle m \rangle^{-1} M_{cl}^{1/2} r_h^3, \tag{1.5}$$

where M_{cl} is the total cluster mass in $M_\odot$. Assuming a mean stellar mass $\langle m \rangle = 1/3 M_\odot$, the distributions of t_{rc} and t_{rh} for the $\sim$ 150 GGCs is shown in Figure 1.1.

1.1.2 Long term dynamical evolution

Early phase of violent relaxation

The first important phase in the evolution of a star cluster lasts up to a few Myr and is mainly dominated by the effect of stellar evolution. This phase is characterized by the expulsion of the residual primordial gas, from which the cluster itself was formed. In some cases, because of mass loss due to stellar evolution (winds from massive stars and Type II supernova explosions), the system undergoes rapid dissolution (see, e.g., Applegate, 1986; Chernoff & Shapiro, 1987; Chernoff & Weinberg, 1990; Fukushige & Heggie, 1995; Portegies Zwart et al., 1998). As a consequence, early cluster dissolution preferentially destroys low-mass clusters in the initial phase. Boily & Kroupa (2003) showed, by means of numerical simulations, that a cluster can lose up to 70% of its mass without undergoing complete dissolution. However, in most cases a cluster undergoes significant expansion and needs to be initially much more compact than observed today to survive this phase (Baumgardt & Kroupa 2007). Because of the significant and irregular mass loss, the gravitational potential of the system can change in a timescale shorter than the crossing time. This

induces the so-called violent relaxation, first studied by Lynden-Bell (1962, 1967), Hénon (1964) and King (1966). During this phase, energy is redistributed without encounters between stars, because the variations in potential directly change the orbits of the stars. Finally, since early cluster dissolution preferentially destroys low-mass clusters, the initial phase may play an important role in the evolution of the mass function of GC systems, significantly flattening its low-mass end (see Vesperini, 2010, and references therein).

Dynamical Friction and Mass segregation

In the next phase, as the expansion due to the mass loss from stellar evolution ends, the two-body relaxation process predominates and determines the structural properties of the system. In this phase, the cluster can be described as made of two distinct regions, an inner isothermal sphere (the core) and an outer halo (Spitzer 1987). The inner region is characterized by an almost uniform density profile, and contains typically about half of the cluster mass, while the surrounding halo is populated by stars preferentially moving in radial orbits. There is a considerable mass loss due to two-body relaxation in the case of clusters that are under the influence of an external tidal field, as some stars attain escape velocities by encounters within the system (eg.Giersz & Heggie 1994; Vesperini & Heggie 1997). This process is referred as evaporation.

At the same time, as the stars exchange energy with each other by their tendency to energy partition, the most massive stars tend to transfer kinetic energy to low mass stars accelerating them, and the low mass stars preferentially populate the outer regions of the cluster (gradually evaporating). The massive stars that have slowed down by to dynamical friction, sink progressively towards the center occupying the cluster core. This process leads to a stratification of the various mass populations, from high-mass to low-mass stars as the radial distance from the centre increases. This way, the stars are segregated by mass. Mass segregation progressively brings changes in the internal cluster structure and in the radial distribution and content of stars with different masses. The level of dynamical evolution of the system can therefore be traced observationally by the radial distribution of heavy objects, like Blue Straggler Stars (see Section 1.2.2). Note that this process has a significant effect on the cluster core, to begin with, and the effect reaches larger distances (beyond the half-mass radius) progressively with time.

Core Collapse and Gravothermal oscillation

The continuous transfer of kinetic energy from the core to the outskirts (massive stars colliding with low mass stars and sinking towards centre) leads to a runaway contraction of the core itself, with a substantial increase of its density virtually toward infinity: the so-called "core-collapse" (hereafter, CC; see, e.g., Spitzer, 1987; Meylan & Heggie, 1997). According to the Virial Theorem, this phenomenon is self-

sustained, because, as the system contracts, stellar encounters become more frequent and the "flow" of kinetic energy from the core to the envelope increases (see, e.g., Hénon 1961, and also the reviews by Meylan & Heggie 1997; Heggie & Hut 2003). Therefore, in absence of energy sources in the core, this process would lead in a finite time to a diverging central density.

The formation and hardening of binary systems (both primordial and dynamically formed) in the core provides the system with the necessary energy to halt CC. When a star interacts with a binary system, the binary can shrink and release energy to the cluster, ceasing the collapse. Clusters that host a considerable fraction of heating sources, such as primordial binaries or stellar mass black holes (BHs), could delay CC or avoid CC completely (see Section 1.1.2). From the observational point of view, CC substantially modifies the density profile of a GC, because the central density significantly increases. Finally, during the phase leading to the cluster CC, both the central (especially) and the half-mass relaxation time (much less) decrease with time. It is predicted (Chernoff & Shapiro, 1987) that post-CC clusters are preferentially located near the Galactic centre where the tidal field is stronger: this implies that GCs have smaller sizes and, thus, shorter relaxation times which rapidly drive them towards CC.

The last phase of the cluster dynamical evolution (usually called the "post-CC phase") is characterized by several episodes of central density increase, followed by stages during which the cluster rebounds toward a structure with lower density and a more extended core. The series of expansions and contractions experienced by cluster core is called gravothermal oscillations (e.g., Bettwieser & Sugimoto, 1984; Meylan & Heggie, 1997). During this process, the cluster structural parameters such as half-mass radius fluctuates around a constant equilibrium value. Investigations about the stability conditions of this process have been carried out by many groups (Goodman, 1987; Cohn et al., 1989) who provided quantitative criteria for the core and the whole system to be stable during this phase. The theoretical understanding of the onset of gravothermal oscillations is still a matter of debate (Breen & Heggie 2012).

Overall, the long-term internal dynamical evolution tends to generate compact clusters, making large-core systems to naturally evolve toward objects with progressively smaller core radius. Concurrently, the radial distribution of stars with different masses progressively varies in time (the most massive objects migrating to the center), and the high-density cluster environment may facilitate the formation of exotic species that are not predicted by the stellar evolution theory (such as blue straggler stars, millisecond pulsars, low-mass X-ray binaries, intermediate-mass black holes; e.g., Ferraro et al. 1997b; Ransom et al. 2005; Pooley et al. 2003).

Effect of Dark Remnants on Dynamics

GCs are million-body systems containing stars with different masses. While at the moment of cluster formation stellar masses varied between $0.08 M_{\odot}$ (the lower limit for the hydrogen thermonuclear burning), to $\sim 100 M_{\odot}$ (the Eddington limit) following the so-called initial mass function (IMF), as the system gets older more massive stars die, and only lower and lower mass stars keep shining. In particular, all the stars more massive than the current MS-TO mass in a GC either became BHs, or neutron stars, or white dwarfs, depending on the initial mass of their progenitors. Tens to thousands of BHs are expected to form in dense stellar environments like in GCs (Kulkarni et al., 1993). Observationally, the presence of stellar-mass BHs and neutron stars (collectively referred to as dark remnants: DRs) in GCs is confirmed (e.g., Strader et al., 2012; Chomiuk et al., 2013; Giesers et al., 2018, 2019, and references therein). However, at least a fraction of these objects is predicted to be ejected from the system either at birth (natal kicks from supernova explosion) or later on, through process known as dynamical ejection. The rate of dynamical ejections is highly dependent on the properties of the cluster, such as its density and the number of BHs present. Indeed, the exact number of neutron stars and BHs in present-day GCs is poorly constrained and, many authors have addressed the problem of the fraction of neutron stars (Davies & Hansen, 1998; Pfahl et al., 2002) and BHs (Sigurdsson & Hernquist, 1993; O'Leary et al., 2006; Repetto et al., 2012; Sippel & Hurley, 2013) retained during the evolution of the cluster (the so-called "DR retention problem"). If the GC two-body relaxation time is sufficiently long, a substantial stellar mass BH subsystem can survive up to a Hubble time or longer (Rodriguez et al., 2016b; Wang et al., 2016).

DRs are thought to substantially influence the cluster dynamics and structural properties depending on the retained fraction. These objects, being much more massive than the average, rapidly segregate to the cluster cores, where they form binary or multiple-BH subsystems and decouple from the rest of the GC, in a process that is commonly referred to as the Spitzer mass-segregation instability(Spitzer 1969). Stars interacting with these dark remnant binary systems in the centre are pushed on wider orbits, causing the expansion of the cluster core. In turn, they can begin to dynamically heat up the "normal" stars in the cluster's core (Sigurdsson & Hernquist, 1993; Mackey et al., 2007; Morscher et al., 2015). This significantly inhibit the mass segregation of less massive stars in the system (Alessandrini et al. 2016) delaying the CC phase (Merritt et al., 2004; Mackey et al., 2008). In some cases, the BH subsystem gets dynamically ejected eventually and the cluster evolution in the absence of heating sources is dominated by two body relaxation, leading to CC and post-CC phases. If a significant population of BHs is retained for a long time, they continue to heat up the core and the cluster remains dynamically young for most of it's lifetime. The presence of a BH subsystem can also lead to the dissolution of tidally filling star clusters due to the loss of dynamical equilibrium (Giersz et al. 2019). This leads to the formation of "dark clusters", i.e., systems composed of

stellar mass BHs surrounded by an expanding halo of luminous stars.

Intermediate-mass black holes (IMBHs) are BHs with masses in the range ofa few 10^2 –$10^5 M_\odot$. They have been sought out for a long time as they could provide the missing link between stellar-mass BHs and supermassive-BHs. The presence of IMBHs in the cores of some GGCs has been debated for a long time. There are many theoretical and observational arguments in favour of the formation of IMBHs in the centres of Galactic GCs (e.g., Lützgendorf et al., 2013; Askar et al., 2017, references therein), with no firm observational evidence. There are few plausible formation scenarios for IMBHs. They could be remnants of hypothesized metal-free Population III stars that formed in the early Universe (Madau & Rees, 2001) or they may form via dynamical processes in star clusters (Miller & Hamilton, 2002; Giersz et al., 2015). In the scenarios explained in Giersz et al. (2015), the IMBH makes up for more than 50% of the cluster mass at 12 Gyr. The presence of a central IMBH is another mechanism that can affect the dynamical evolution of star clusters. In the presence of this object, a shallow central cusp in the radial density profile is predicted and it has also been suggested they could produce a central cusp in the velocity dispersion profile of the GC (Bahcall & Wolf, 1976; Baumgardt et al., 2005; Miocchi, 2007; Noyola & Baumgardt, 2011). The interplay between their formation mechanisms and the dynamical evolution of the host cluster is yet to be understood thoroughly, but also the presence of an IMBH is thought to delay CC and make it shallower. This is indeed a still an active field of research.

King Model

Due to the recurrent gravitational interactions among stars, the distribution of stellar velocities in collisional systems eventually follows the Maxwell-Boltzmann function. This is assuming that the star cluster has experienced two-body relaxation after which it has completely lost memory of it's initial conditions. Taking into account the three most important elements of GC structure, namely, dynamical equilibrium, two-body relaxation and tidal truncation[2], equilibrium models based on the lowered Maxwellian distribution were constructed which successfully fit the surface-brightness profiles of GCs: these are commonly known as King models (King 1966). The phase-space distribution function of King model is given by:

$$f(E) = \begin{cases} \rho_0 (2\pi\sigma^2)^{-3/2} (e^{E/\sigma^2} - 1) & \text{if E}>0 \\ 0 & \text{if E} \leqslant 0 \end{cases} \tag{1.6}$$

where ρ_0 is the central density, σ is the one-dimensional velocity dispersion and E the energy per unit mass in the mean potential $\Psi(r)$, so that :

[2]GCs are tidally truncated because of the presence of the external tidal field from the host galaxy.

$$E = \Psi(r) + \frac{v^2}{2}. \tag{1.7}$$

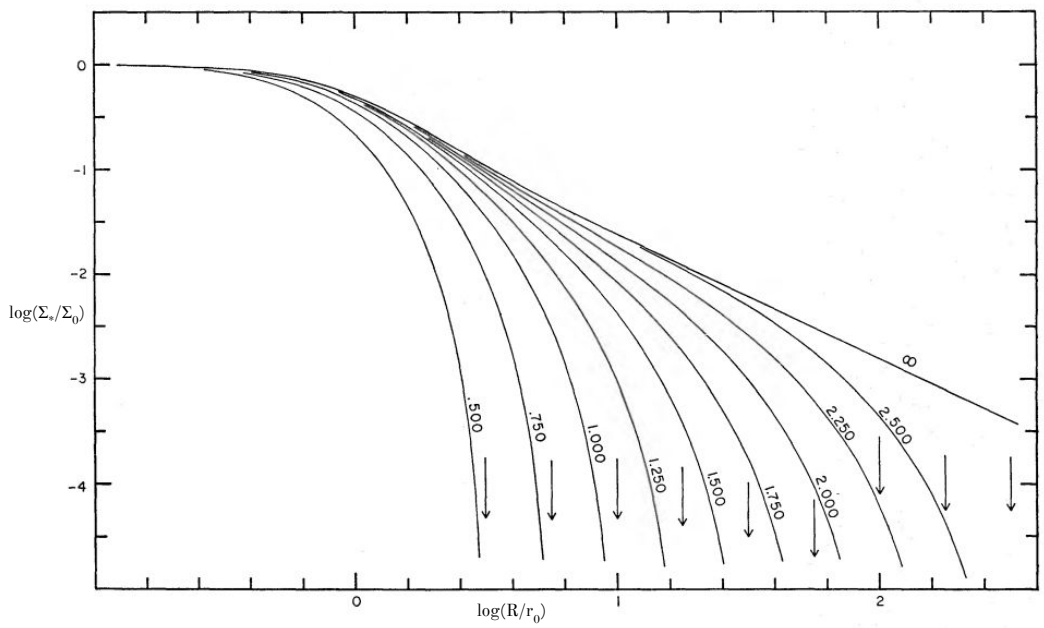

Figure 1.2: Logarithm of the projected density (normalized to its central value) for King models. Different curves are obtained for different values of W_0 (the labels on each curve mark the corresponding values of the concentration parameter c). The radius is normalized to the King radius r_0. From King (1966).

Since GCs drift in the gravitational potential of the host galaxy, at a certain distance from the cluster center, the galactic gravitational potential dominates over the one of the GC itself. Theoretically, a tidal radius (r_t) is defined as the radius beyond which the stars are not bound anymore to the cluster. The potential Ψ is defined so that $\Psi(r_t)$=0. The King model family has a characteristic scale length, usually called King radius, which is defined as:

$$r_0 = \sqrt{\frac{9\sigma^2}{4\pi G\rho_0}}. \tag{1.8}$$

The dimensionless parameter W_0, which is proportional to the central potential of the model, or, alternatively, the concentration parameter defined as:

$$c = \log\left(\frac{r_t}{r_0}\right) \tag{1.9}$$

unambiguously determine the shape of the profile. Figure 1.2 shows the projected density profile of a few King models calculated for c ranging from 0.5 to 2.5 (see the labels beside each curve). The radial coordinate along the x-axis is normalized to r_0. Hence, each curve is characterized by a different value r_t, which is marked by the arrows. As apparent, the King model family is characterized by a constant density in the center of the system. Other characteristic quantities of GCs are: the core radius (R_c), i.e., the distance from the center at which the surface density (or brightness) is equal to half of its central value; the half-mass radius (r_h), i.e., the distance from the center that includes half the total mass; the half-light radius (r_{hl}), i.e., the distance from the center that includes half the total projected luminosity. A parameter that quantifies how closely packed stars are in a GC is the central luminosity density ν_0, expressed in $L_\odot/\mathrm{pc}^3$, which is commonly assumed to differ from the central mass density for just a constant factor, namely, the mass-to-light ratio (M/L). For old stellar systems as GGCs are, $M/L \simeq 3$ (e.g., Maraston, 1998).

1.2. Dynamical Indicators

The characteristic timescale of dynamical evolution depends in a very complex way on various internal and external quantities, like the cluster total mass, size, central density, binary fraction, ans well as its orbit within the galactic potential well, and so on. Hence, it can significantly differ even in clusters of the same chronological (stellar) age and, within the same system, from high- to low-density regions. Because of such a complexity, the observational identification of the evolutionary stage reached by a cluster (i.e., its "dynamical age") is hard and may lead to ambiguous conclusions. Of course, this may significantly hamper efforts aimed at linking the theoretical predictions concerning the dynamics of star clusters with observations.

Determining the dynamical evolutionary stage of star clusters is important not only to have a complete physical understanding of these systems, but also because internal dynamical processes can have a significant impact on their stellar population and observational properties. For instance, blue straggler stars and millisecond pulsars are not predicted by the stellar evolution models of single objects, but they are originated by dynamical processes involving direct stellar collisions and/or the evolution of binary systems (e.g., McCrea, 1964; Hills & Day, 1976; Bhattacharya & van den Heuvel, 1991; Sills et al., 1997). Hence, their frequency and their properties depend on the dynamical stage of the system and can be used to get information on the internal dynamics of GCs (see, e.g., Freire et al., 2004; Ransom et al., 2005; Ferraro et al., 2009a; Verbunt & Freire, 2014; Ferraro et al., 2018a, 2019). In addition, other events such as neutron star and white dwarf mergers are thought to be enhanced in CC clusters, with important implications for our understanding not only of the internal dynamics of the system itself, but also, for example, of the rate of type Ia supernovae, and the origin of short gamma-ray bursts (see, e.g., Grindlay et al., 2006; Rodriguez et al., 2016a; Kremer et al., 2021, see discussion in Ye et al.

2020).

Up to recently, the characterization of the dynamical age of GCs was essentially based on their structural morphology. In fact, the classification of GCs as CC or post-CC systems has been mainly based on the detection of a steep power-law cusp in the central portion of the density profile (see Djorgovski & King 1984; Ferraro et al. 2003, 2009). Also another frequently used indicator, the central relaxation time (t_{rc}), is estimated from the measure of structural parameters such as the core radius and the central density, following the analytical expression quoted in eq.(1.4). However, GGCs provide the advantage that stars can be resolved and studied individually, thus offering additional possibilities to investigate the internal dynamical state of the system. In principle, either specific classes of objects, or the entire cluster population can be used as probes of the cluster dynamical evolution. Indeed, a lot of work in this direction has been done over the last decades. Several theoretical works, mainly based on the results of extensive N-body simulations, recently suggested that radial variations of the stellar mass function, the presence of orbital anisotropy, and the velocity dispersion profile as a function of stellar mass can be used to infer the level of energy equipartition and the dynamical state of GCs (e.g., Baumgardt & Makino, 2003; Tiongco et al., 2016; Bianchini et al., 2016; Webb & Vesperini, 2017; Bianchini et al., 2018). In turn, these diagnostics are becoming measurable in an increasing number of GGCs, especially thanks to multi-epoch HST observations and improved procedures of data analysis, which allow high-precision photometry and proper motion measurements for stars down to a few magnitudes below the MS-TO. Recent examples of this kind of studies can be found, e.g., in Libralato et al. (2018, 2019), and Cohen et al. (2021). However, these approaches require observations that, even in the Gaia era, are still very challenging for most GGCs (due to their high central densities and relatively large distances from Earth). Alternative diagnostics of GC internal dynamics are provided by the properties of their blue straggler stars (BSSs) and they offer the advantage to be more easily measurable from observations (e.g., Ferraro et al., 2018a).

In the following sections, we discuss in more details both the “traditional" and the BSS dynamical indicators.

1.2.1 Density cusp

Although for most of the observed GCs the density profile is reproduced very well by the King model family, in a few cases the inner part significantly deviates from a constant behavior. Indeed the classification of GGCs as CC or post-CC systems has been traditionally based on the detection of a steep power-law cusp in the central portion of the density profile (see Djorgovski & King 1984; Ferraro et al. 2003, 2009a), strongly exceeding from the flat-core behavior of the King model. Figure 1.3 shows the notable example of M30 (NGC 7099), with a steep inner cusp clearly detected both in the number density profile (red circles in the main panel),

and in the surface brightness profile (red circles in the inset). This diagnostic, however, has been found to be not fully reliable and univocal in properly assessing the level of dynamical evolution reached by star clusters. In fact, the cusp may be significantly reduced during the post-CC gravothermal oscillations, or due to the occurrence of other processes (e.g., depending on the binary fraction) that may contribute to significantly decrease the depth of CC, or it can be hardly detectable from observations. Trenti et al. (2010), for instance, showed how a system in its gravothermal oscillation phase can look like a non-PCC cluster from the point of view of its concentration. Also, the GCs hosting a central IMBH are predicted to have a central shallow cusp in their density profiles.

As a matter of fact, only a small fraction (15-20%) of the entire population of GGCs displays a central cusp in the star density profile which identifies these objects as clusters in the Post-CC phase (Djorgovski & King, 1986; Chernoff & Djorgovski, 1989; Djorgovski & Meylan, 1994), in spite of the fact that the central relaxation time is sensibly shorter than the age in most of the cases (see the compilations by Djorgovski 1993 and Harris 1996).

1.2.2 Blue Straggler Stars

The intense dynamical activity and the repeated interactions between stars in GCs allow the formation of numerous exotic objects, such as millisecond pulsars, cataclysmic variables, low mass X-ray binaries, and Blue Straggler Stars (BSSs). Being generated by direct collisions or mass-transfer activity in binaries, BSSs turn out to be significantly heavier ($\sim 1.2 M_{\odot}$) than the average stellar mass ($m \sim 0.3 M_{\odot}$). This makes them powerful gravitational probes of key physical processes (such as mass segregation and dynamical friction) characterizing the dynamical evolution of star clusters. In addition, BSSs are easy to distinguish from the other cluster populations, given their distinctive position in the CMD: they are located along an extrapolation of the cluster main sequence toward bluer colors and brighter magnitudes, than the MS-TO point. Hence, they are ideal test particles to probe the internal dynamical evolution of stellar systems.

Indeed, the radial distribution of BSSs with respect to a population of "normal" (lighter) cluster stars has been used as "dynamical clock" to efficiently measure the dynamical age of stellar systems (Ferraro et al., 2012; Lanzoni et al., 2016; Ferraro et al., 2018a, 2020). The original definition of the dynamical clock has been done in terms of the number of BSSs normalized to the number of giant or horizontal branch stars, in different radial bins around the cluster center. The distributions observed in a large sample of GGCs turned out to be either constant, or bimodal (with a central peak, a minimum, and an external rising branch), or unimodal (with a central peak and a steadily decreasing trend for increasing radius). This allowed the grouping of the observed clusters in three families corresponding to different levels of dynamical evolution (see Figure 1.4): *Family I* clusters are those showing

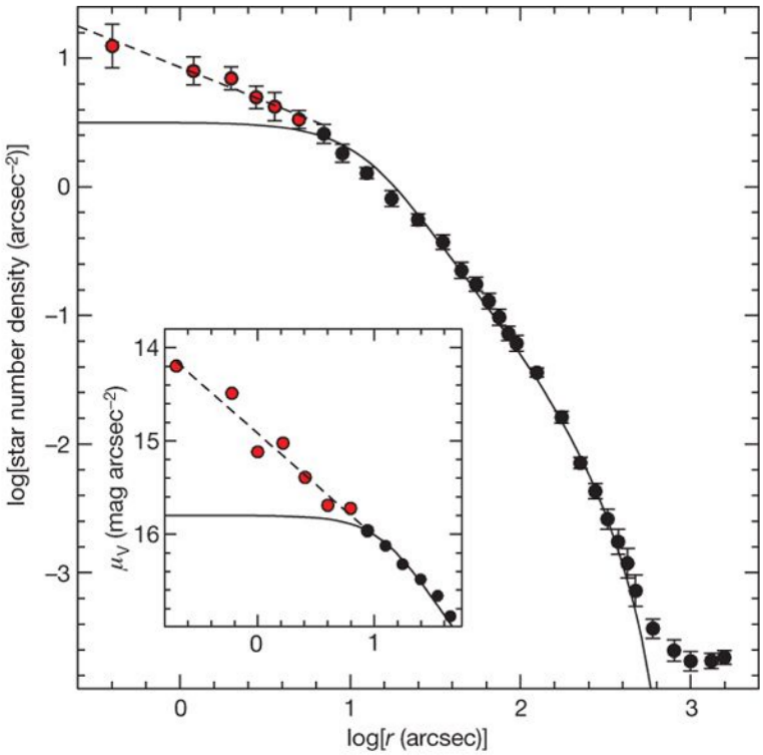

Figure 1.3: Projected density profile obtained from resolved star counts (main panel) and surface brightness profile (inset) of the GGC M30 (NGC 7099). The black circles are well fitted with the King model represented by solid black line, while a clear deviation from a flat-core behavior is well apparent in the innermost regions (red circles). The inner density cusp is well fitted by a power-law function with slope= -0.5 (black dashed line). From Ferraro et al. (2009a)

a flat distribution (BSSs are not centrally segregated with respect to lighter stars), indicating that dynamical friction did not segregate BSSs toward the cluster centre yet; *Family II* clusters are of intermediate dynamical age, with the minimum of the observed distribution indicating the radial distance out to which dynamical friction has been efficient; *Family III* clusters are the dynamically oldest systems, where also the most external BSSs have already sank to the center because of the action of dynamical friction (see Ferraro et al., 2012). The dynamical clock has been later refined with the introduction of the A^+ parameter, defined as the area enclosed between the cumulative radial distribution of BSSs and that of a lighter, reference population (Alessandrini et al., 2016). As shown in the left panel of Figure 1.5, due to their larger mass, BSSs segregate to the cluster centre more rapidly than the reference population: their cumulative radial distribution (blue lines) progressively becomes steeper than that of lighter stars (red lines) for increasing time (from the top to the bottom panel), which correspondingly makes the enclosed area (A^+) also increasing. As shown in Lanzoni et al. (2016) the two definitions of the dynami-

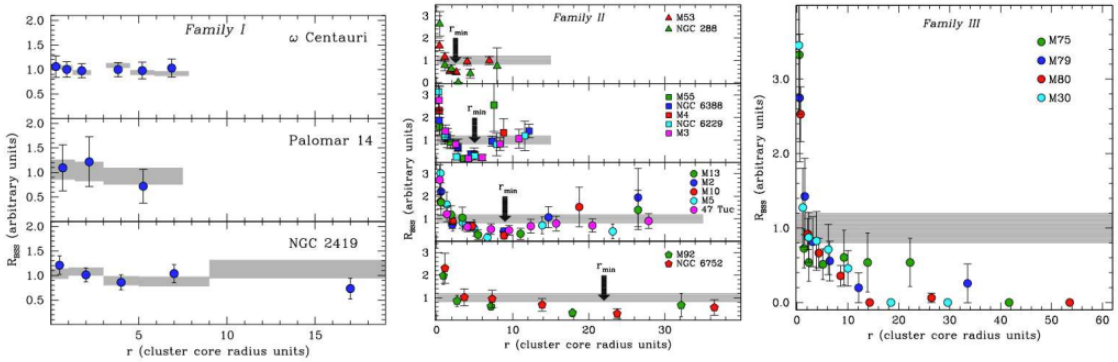

Figure 1.4: Radial distribution of BSSs (colored symbols) compared to that of normal cluster stars taken as reference (grey strips) in three main "dynamical families": Family I = dynamically young clusters (left panel), Family II = dynamically intermediate-age clusters (central panel), Family III = dynamically old clusters (right panel). From Ferraro et al. (2012).

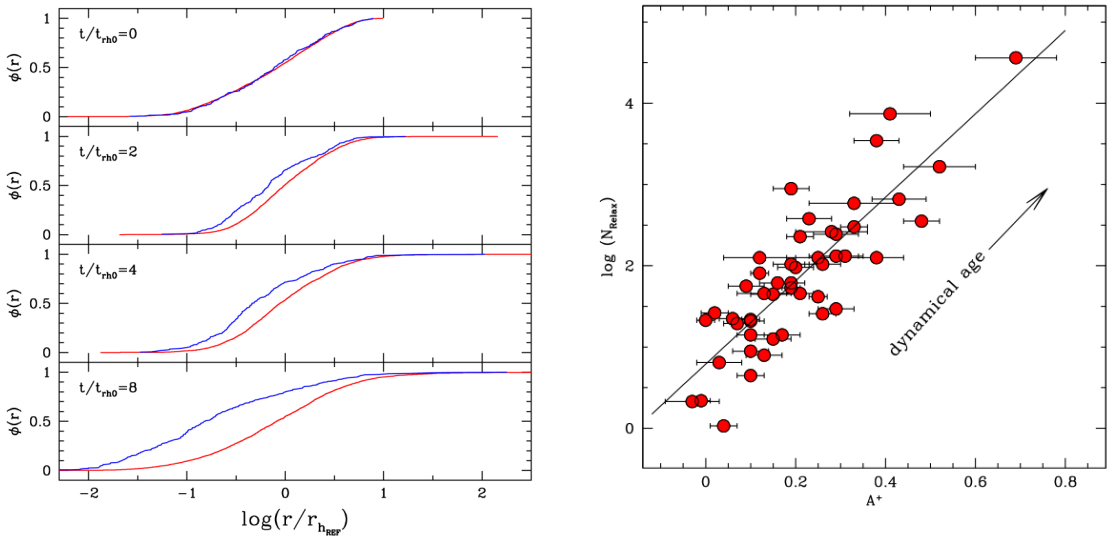

Figure 1.5: Left panel: cumulative radial distributions of BSSs (blue lines) and reference stars (red lines) as a function of time (from top to bottom). The area enclosed between the two curves increases with time and corresponds to the value of the A^+ parameter (from Alessandrini et al. 2016). Right panel: number of current central relaxation times as a function of the A^+ parameter for a sample of 48 observed GGCs (from Ferraro et al. 2020).

cal clock well correspond each other, the latter one having the main advantage of not needing arbitrary choices about radial binning. The efficiency of A^+ as powerful dynamical indicator has been further confirmed by the observation of a strong correlation between A^+ and the number of relaxation times occurred since cluster formation ($N_{\rm relax}$) [3] that has been found from the analysis of $\sim 1/3$ of the entire GGC population (Ferraro et al., 2018a; see Figure 1.5). Interestingly, the same correlation is also followed by a by a sample of old GCs in the Large Magellanic Cloud (Ferraro et al., 2019) and two young cluster in the Small Magellanic Cloud (Dresbach et al., 2022).

BSSs have been found to also trace the occurrence of CC and probe the time when it happened. In fact, a double BSS sequence has been detected in the post-CC cluster M30 (Ferraro et al. 2009a; see Figure.1.6), and it has been interpreted as the manifestation of the two formation processes, with the bluest sequence being populated by collisional BSSs generated by an enhanced activity of gravitational interactions during CC. Moreover, the measure of the luminosity extension of the blue sequence provided the first empirical dating of the CC event, suggesting that it happened 1-2 Gyr ago in M30 (see Ferraro et al. 2009a; Portegies Zwart 2019). Since then, the double BSS sequence has been discovered in several additional post-CC clusters (see the cases of NGC 362 in Dalessandro et al. 2013, M15 in Beccari et al. 2019, and NGC 6256 in Cadelano et al. 2022), thus strengthening the link between this feature and the CC event.

1.3. MOCCA simulations

In this thesis, in order to investigate the long-term dynamical evolution of star clusters with different initial properties, we make use of a Monte Carlo code, called MOCCA. MOCCA, stands for MOnte Carlo Cluster simulAtor. It is at present one of the most advanced numerical codes for stellar dynamical simulations, and is capable of following the evolution of real size star clusters with a detail comparable to that of N-body simulations, but orders of magnitude faster (several hours for number of particles, $N = 2 \times 10^6$).

Modeling dense star clusters is challenging due to the collisional nature of stars within these systems. Although modern numerical codes such as HiGPUs (Capuzzo-Dolcetta et al., 2013), PhiGRAPE (Harfst et al., 2008), ph4 (McMillan et al., 2012), frost (Rantala et al., 2021), and the well-known NBODY series (Aarseth, 2003, 2012) and its derivatives (NBODY6++GPU, Wang et al. 2015) provide high accuracy in modeling, they require months or even years to evolve clusters with 10^6 particles for about 10 Gyr using graphic processing units (GPUs; e.g. Heggie, 2014; Wang et al., 2016; Rantala et al., 2021). A faster approach is through Monte Carlo method,

[3] $N_{rmrelax}$ is defined as the ration between the chronological age (12 Gyr) and the central relaxation time of each cluster, determined as in eq.(1.4).

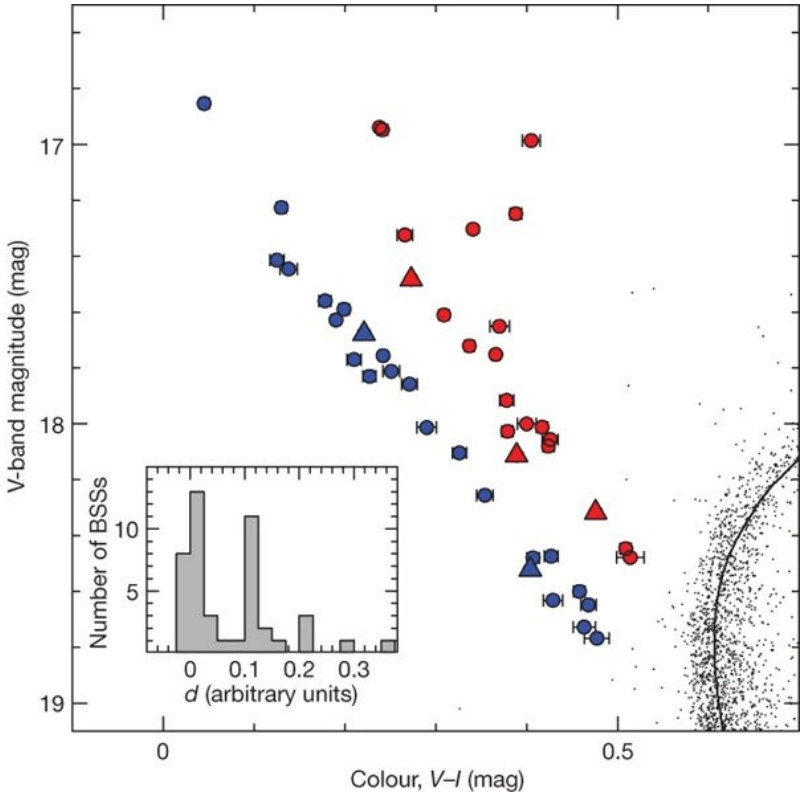

Figure 1.6: BSS region in CMD of M30. The selected BSSs are plotted as circles, with the red and blue colours distinguishing the red and the blue BSS sequences, respectively. The two sequences are separated in magnitude by $\delta V \approx 0.4$ mag and in colour by $\delta(V_I) \approx 0.12$ mag.

which leverages a statistical treatment of stellar dynamics, where the cumulative effect of many distant two-body encounters is modeled as a single effective scattering between neighboring particles. Currently, there are two efficient Monte Carlo codes capable of modeling realistic populations of star clusters and they are CMC (Joshi et al., 2000) and MOCCA (Giersz, 1998). MOCCA is broadly comparable with CMC although there are some differences in the choices of the dynamical time step and other aspects of stellar evolution and collisions. The MOCCA code has been developed for more than 20 years (Giersz, 1998, 2001, 2006; Giersz et al., 2008; Giersz et al., 2013; Hypki & Giersz, 2013) and is characterized by high speed, modularity and detailed information about each and every object in the system.

MOCCA incorporates most of the processes that are important during the evolution of a stellar system. The relaxation processes are treated using the method described by Hénon (1971), that was significantly improved by Stodolkiewicz (1982, 1986). The code consists of the following ingredients: SSE and BSE codes (Hurley et al., 2000, 2002) for treating binary and stellar evolution, while strong binary–single and binary–binary interactions are handled by the FEWBODY code (Fregeau et al.,

2004). The binary formation in three-body interactions is described in Giersz (2001). Stars are escaping from the cluster according to the description given by Fukushige & Heggie (2000). Escape processes are not instantaneous but take place (through Langrangian points) after some delay. By default, supernova natal kick velocities for NSs and BHs are assigned according to a Maxwellian distribution, with velocity dispersion of 265 kms^{-1} (Hobbs et al., 2005). In some of the models, BH natal kicks are modified according to the mass fallback procedure described by Belczynski et al. (2002). This prescription leads to higher average of BH mass and also reduces their natal kicks which results in higher retention fractions in the simulated cluster models (Arca Sedda et al., 2018; Askar et al., 2018). To model the Galactic potential, MOCCA assumes a point mass with total mass equal to the mass of the galaxy enclosed within the Galactocentric radius where the simulated cluster is placed in a circular orbit.

MOCCA follows all binaries, except extremely soft ones, which are artificially disrupted in binary–single dynamical interactions according to a prescription derived from Heggie (1975, equation 4.12). Except binaries, higher hierarchies are not allowed, as triples and quadruples are artificially disrupted into binaries and single stars (see Hypki & Giersz, 2013).

The MOCCA-SURVEY which consists of a large number of star cluster models simulated with the MOCCA code starting from a large variety of initial conditions, well reproduces the observational properties of the Galactic GCs (Askar et al., 2016, , see their fig. 1). Indeed, MOCCA code is used to create a set of models that are representative of observed Milky Way GCs in this thesis in Chapter 4.

In essence, MOCCA is ideal for performing large surveys and for carrying out detailed studies of collisional systems.

Chapter 2

New dynamical indicators

Mainly based on:
Bhat et al. (2022), ApJ, 926, 118

In this chapter, we analyze the time evolution of a "synthetic GC" obtained from a Monte Carlo simulation run, with the specific aim of defining suitable diagnostics of dynamical aging from a new perspective, i.e., by using the entire population of evolved stars. We provide the definition of three new parameters and test their effectiveness in distinguishing clusters in the pre-CC phase, from those experiencing post-CC evolutionary stages, thus tracing the dynamical aging of the system up to CC and beyond. The chapter is organized as follows. In Section 2.1 we describe the initial conditions of the Monte Carlo simulation run, and the (observational) approach adopted in the following analysis. Section 2.2 discusses the method used to determine the projected density profile and the best-fit King (1966) model of each extracted snapshot. In Section 2.3 we present the assumptions adopted to build the normalized cumulative radial distributions of cluster stars and discuss the dependency of their morphology on the simulation evolutionary time. This is then used in Section 2.4 to define three new empirical parameters able to trace the internal dynamical evolution of stellar systems. Their dependency on the adopted assumptions is discussed in Section 2.5. The summary and conclusions of the work are presented in Section 2.7.

2.1. Initial Conditions and Methods

In this work we focus our attention on the dynamical evolution of a star cluster followed with a Monte Carlo simulation run with the MOCCA code (Hypki & Giersz 2013; Giersz et al. 2013). The code includes the effects of binary and stellar evolution (modeled with the SSE and BSE codes; Hurley et al. 2000, 2002) with supernovae kicks assumed to follow a Maxwellian distribution with dispersion equal to 265 km/s

(Hobbs et al., 2005), the effects of two-body relaxation and a tidal truncation. The initial conditions of the simulation have been chosen well within the range of values observed for GGCs, with the main aim to provide us with a system that experiences all dynamical evolutionary phases and reaches CC within 12-13 Gyr from formation. Since the prime goal is to put forward the definition of new dynamical indicators, in the following we will present the detailed analysis of this specific run. However, two additional simulations, run from slightly different initial conditions, are discussed in Section 2.6. The simulated cluster has initially 500K single stars with masses ranging between $0.1 M_{\odot}$ and $100 M_{\odot}$ following a Kroupa (2001) mass function. The initial total mass of the system is $\sim 3.2 \times 10^5 M_{\odot}$, while it is approximately half this value after 12 Gyr of evolution. The stars are initially distributed as a King (1966) model with dimensionless central potential $W_0 = 6$, and the cluster is tidally underfilling, with a tridimensional half-mass radius $r_h = 2$ pc and a Jacobi radius set equal to 61 pc (corresponding to the value the cluster would initially have if orbiting at a Galactocentric distance equal to 4 kpc). No primordial binaries are included in this run, although binary stars dynamically form as the system approaches the CC phase. Since the code includes prescriptions for stellar evolution, it provides for every star at any evolutionary time not only the mass and the three components of position and velocity, but also the magnitude in two photometric bands (namely the V and B band), from which a color-magnitude diagram (CMD) of the stellar content at any epoch can be built.

The simulation follows the cluster evolution for ~ 16 Gyr from its formation. Although this is larger than the Hubble time, it allows us to follow the cluster dynamical evolution also after CC, which occurs at 12.8 Gyr (see below). In Figure 2.1 we show the time evolution of the cluster's 1% Lagrangian radius ($r_{1\%}$, i.e., the radius including 1% the total cluster's mass): the temporal variation of this radius illustrates well the various phases of the cluster's dynamical evolution and, in particular, the CC and post-CC phases. The effects of mass loss due to stellar evolution cause the cluster to initially expand as shown by the early increase in $r_{1\%}$. Then, after ~ 2 Gyr from formation, two-body relaxation starts to drive the evolution of the cluster central region leading it to a progressive contraction, with $r_{1\%}$ shrinking by approximately a factor of 7 in 10 Gyrs. The figure shows that the contraction phase is characterized by an initial "slow phase" ($r_{1\%}$ shrinks by a factor of 2 in approximately 8 Gyrs) and a final "rapid phase" (a factor 4 shrinking, from 0.25 pc to 0.07 pc, in less than 3 Gyrs). At this time, $r_{1\%}$ reaches its minimum value: this is the CC event, occurring at a time $t_{\rm CC} = 12.8$ Gyr. Later, a phase characterized by gravothermal oscillations is clearly distinguishable in the figure, as cyclic expansions and contractions of the 1% Lagrangian radius. Of course, during this evolution, not only the central region, but the entire cluster structure varies with time. To carefully investigate these changes, we extracted 38 time snapshots sampling different evolutionary phases of the system, as marked by the vertical dotted lines in Figure 2.1. In order to easily and immediately link each snapshot to the corresponding evolutionary phase, we adopted the following color code: *green* for snapshots be-

longing to the early slow contraction phase, *cyan* for snapshots belonging to the final rapid contraction phase, *blue* for snapshots sampling the CC phase, and *yellow* for snapshots probing the post-CC gravothermal oscillations epoch.

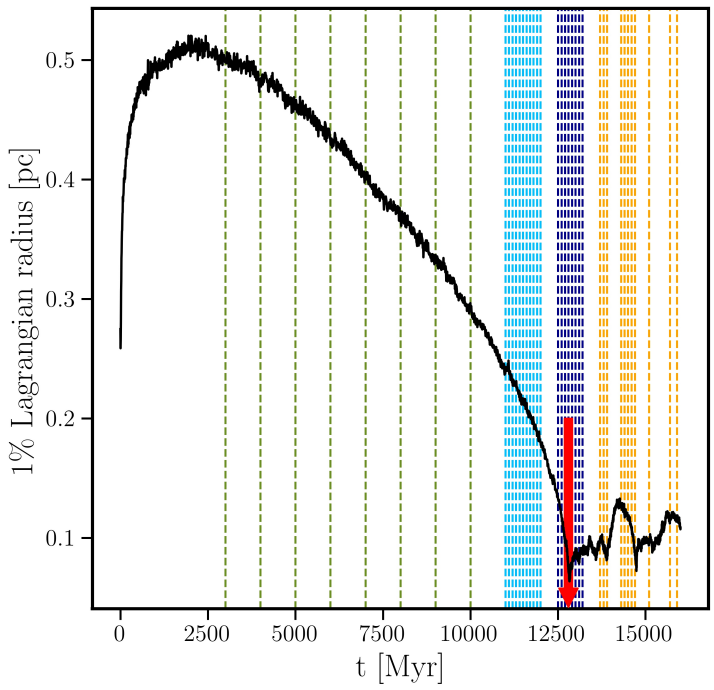

Figure 2.1: Time evolution of the 1% Lagrangian radius (in pc) of the simulated cluster (black line). The vertical lines correspond to the 38 time snapshots analyzed in this work, color-coded as follows to mark different evolutionary stages: green, cyan, blue and yellow for early, pre-CC, CC, and post-CC, respectively. The time of CC ($t_{\rm CC}$ = 12.8 Gyr) is marked with a large red arrow.

In the following analysis, each time snapshot has been studied from an "observational perspective", i.e., as if the simulation output was the product of real observations. This is meant to allow the definition of parameters that can be realistically derived and measured in observational investigations. Thus, procedures and standard strategies, as well as approximations routinely adopted in dealing with observational data, were applied to the snapshots. To this purpose, each snapshot has been projected on a 2D plane and the distances of all the stars from the cluster's center have been transformed from parsecs to arcseconds assuming that the system is at 10 kpc from the Sun, which is the typical distance of GGCs (Harris, 1996; Baumgardt & Vasiliev, 2021). We also limited most of the analysis only to stars that are brighter than 0.5-1 magnitudes below the MS-TO, in agreement with the threshold adopted in many observational studies to avoid photometric incompleteness biases and to

deal with samples of equal-mass stars (see, e.g. Lanzoni et al., 2007b, 2010; Lanzoni et al., 2019; Miocchi et al., 2013).

2.2. Projected density profile

As a first step of our analysis, we studied the projected density profile of the simulated cluster at different epochs, to verify whether a central cusp develops at $t_{\rm CC}$, as expected, and how it evolves with time. To this purpose, we followed the same procedure adopted in several observational works determining the radial distribution of stellar number counts per unit area, $\Sigma_*(R)$, instead of the surface brightness profile (e.g. Miocchi et al., 2013; Lanzoni et al., 2019). Summarizing: *(i)* only stars brighter than one magnitude below the MS-TO (i.e. with $V < V_{\rm TO} + 1$) have been taken into account; *(ii)* the sampled area has been divided into concentric annuli centered on the cluster center, assumed to be at coordinates (0,0), and *(iii)* each annulus has been typically partitioned into four sub-sectors. The exact number of annuli and sub-sectors is chosen as a compromise between including a sufficiently large number of stars to provide enough statistics, and a good radial sampling of the profile. Thus, it was set according to the (time-evolving) structure of the system. The projected cluster density at every radial distance from the center was then determined as the average number density of particles in the adopted sub-sectors, and its uncertainty was estimated from the variance among the sub-sectors. For the sake of illustration, in Figure 2.2 we show the projected star density profile obtained for two representative snapshots: one determined at $t = 7$ Gyr, during the pre-CC evolution (left panel), the second obtained for $t = 13.8$ Gyr, slightly after CC(middle and right panels). As expected, the central portion of the former is flat, while a significant density cusp, following a steep power-law behavior, is clearly visible toward the cluster center in the post-CC case.

Following what is commonly done in observational works (e.g. Miocchi et al., 2013; Lanzoni et al., 2019), we then searched for the single-mass King (1966) model that best fits the density profile obtained in the various snapshots. We explored a grid of models with dimensionless parameter W_0 (which is proportional to the gravitational potential at the center of the system) varying between 4 and 10.75 in steps of 0.05, corresponding to a concentration parameter c spanning the interval between 0.84 and 2.5. This parameter is defined as $c = \log(r_t/r_0)$, where r_t is the truncation or tidal radius of the system, and r_0 is the characteristic scale-length of the model named "King radius". The latter is often identified with the core radius R_c, which is the observationally accessible scale length corresponding to the distance from the center where the projected density is equal to half the central value. Indeed, they are quite similar, especially for large values of W_0 or c: the ratio R_c/r_0 varies between ~ 0.82 for $c = 0.84$, and ~ 0.99 for $c = 2.5$. We adopted the χ^2 approach described in detail in Lanzoni et al. (2019, see also Miocchi et al., 2013) to determine the best-fit solution (i.e., the one minimizing the residuals between the model and the

"observed" profile) and to estimate the uncertainties of the best-fit parameters.

In agreement with what is found observationaly for most GCs, we conclude that the King model family well reproduces the projected density profiles of pre-CC systems, while it shows a clear inconsistency in the innermost region of CC and post-CC snapshots. Figure 2.2 illustrates the result for the pre- and a post-CC cases discussed above. The best-fit King model is shown as a thick red line, while its uncertainty is represented by the shaded area and corresponds to the set of King models built by varying the fitting parameters within their uncertainty ranges. The King model function excellently reproduces the observed profile at any distance from the cluster center for the pre-CC snapshot (left panel). Conversely, being constant at small radii by construction, it cannot properly describe the central density cusp observed at $t = 13.8$ Gyr, after CC (central panel). Hence, in the presence of a central density cusp two different approaches are possible: either (1) to fit the entire density profile and search for the model providing the best solution regardless of its inadequacy in the region close to the center, or (2) to exclude from the fit the innermost portion of the density profile (here we assumed $R < 5''$ as a reasonable value). The central panel of Figure 2.2 corresponds to approach (1), while the right-hand panel shows the result of approach (2). The latter, combined with a linear fit to the innermost data points (oblique dashed line in the figure), clearly allows a much better description of the complex shape of the star density profile of CC and post-CC systems, but it depends on the (arbitrary) choice of the size of the region to be excluded from the King fit and it provides parameters (as R_c, r_h and c) that are not representative of the real cluster structure. Approach (1) clearly provides a poor representation of the central density profile, but it offers the advantage to be free from arbitrariness, thus allowing a coherent analysis of the density profile irrespective of the cluster dynamical stage.

Although defining a core region (with constant density) is formally meaningless for CC and post-CC systems, the time behavior of R_c and c obtained from approach (1) is qualitatively consistent with that of the 1% Lagrangian radius. This is illustrated in Figure 2.3, showing that the core radius progressively decreases to a minimum value at $t_{\rm CC}$, then stays almost constant for increasing time, similarly to the trend of $r_{1\%}$ shown in Figure 2.1. The concentration parameter c displays the opposite behavior and when the power law cusp develops, during and after CC, it reaches values larger than ~ 2. The time evolution of these parameters is in agreement with previous findings (e.g. Trenti et al., 2010; Heggie et al., 2006). Indeed a concentration parameter $c \sim$ 2-2.5, together with the the presence of a central cusp in the density profile, are the two diagnostics commonly used in the literature to classify a GC as CC or post-CC (see, e.g., Djorgovski & King 1984; Lugger et al. 1995; Ferraro et al. 2009a).

To properly explore the development and transformation of the central cusp in the simulations, we show in Figure 2.4 the star density profile of the latest 16 snapshots, sampling the last 6 Gyr of evolution (from 10 to 16 Gyr). To facilitate

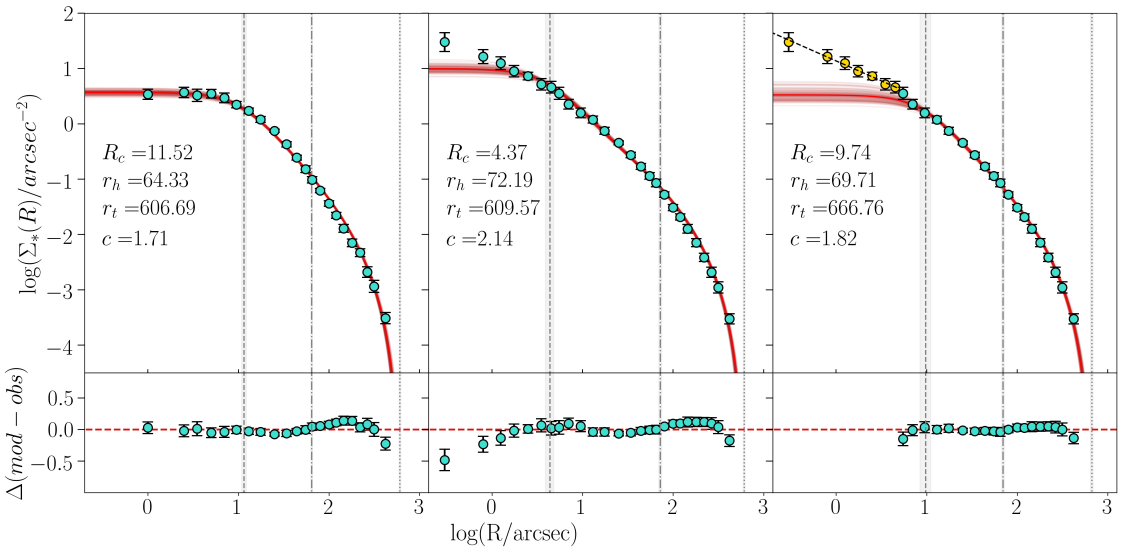

Figure 2.2: Projected density profile (colored circles), obtained as number of stars per unit area in different concentric annuli around the cluster center, for two simulation snapshots: a pre-CC cluster at $t = 7$ Gyr (left panel), and a post-CC system at $t = 13.8$ Gyr (central and right panels). The thick red line corresponds to the best-fit King model, while the shaded area marks its uncertainty (see Section 2.2 for the details). The bottom panels show the residuals between the observations and the best-fit King model. For the post-CC snapshot, two different approaches have been adopted to determine the best-fit King solution: (1) the entire observed profile has been considered (central panel, cyan circles), (2) only the data points beyond 5″ from the center have been included in the fit (right panel, cyan circles), while the innermost portion of the profile (yellow circles) has been described through a linear fit (black dashed line). The positions of the core, half-mass and tidal radii are marked, respectively, by a dashed, dotted-dashed, and dotted vertical line, and their values are labelled in the legend together with that of the concentration parameter.

the comparison, all the profiles have been vertically shifted until their density at $R = 65''$ matches the one measured in the $t = 10$ Gyr snapshot, with 65″ (~ 3 pc) roughly corresponding to the value of the tridimensional half-mass radius of the 10 Gyr best-fit King model, which is represented in all panels as a black solid line. The color code is the same adopted in Figure 2.1 to flag the dynamical stage of the selected snapshots. The first two panels show that ~ 3 and 2 Gyr before CC, respectively, the star density profile is well reproduced by the King model. The third panel samples the CC event and the setting of the cusp. The remaining 13 panels probe the gravothermal oscillation phase. As can be seen, once set, the central cusp remains visible in the whole post-CC evolution (yellow profiles). This is the first relevant result of the present analysis, since it clearly demonstrates that the central

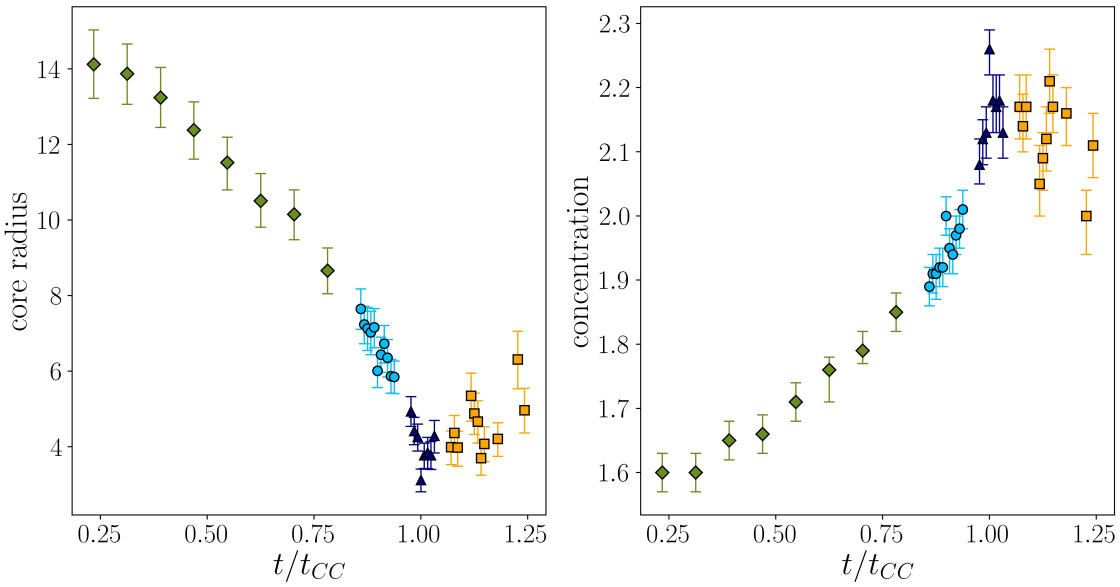

Figure 2.3: Time evolution of the core radius (left panel) and concentration parameter (right panel) as obtained from the King model fit to the entire star density profile of all the extracted snapshots. Different colors and symbols mark different evolutionary stages: green diamonds, cyan circles, blue triangles and yellow squares for early, pre-CC, CC, and post-CC, respectively (the color code is the same as in Figure 2.1).

cusp, once set, never disappears, in spite of the subsequent core radius oscillations. Hence, we can conclude that the density profile of star clusters is characterized by the presence of a central cusp also during the post-CC gravothermal oscillation phase.

However, the simulation also shows that the cusp's slope varies in time during the post-CC stage and the cusp becomes shallower during the expansion phases of gravothermal oscillations, thus rising the problem of its operational detectability and proper characterization. Indeed, the cusp detection and its correct measure are among the most critical issues from the observational point of view. The photometric incompleteness of the catalog, which becomes increasingly severe in the innermost cluster regions, artificially decreases the number of resolved stars close to the center. Thus, an appropriate assessment of the level of completeness of the observational sample is a key step to firmly establish the existence and the entity of the cusp. If the density profile is built with methods similar to that described above, but too shallow observations are used, the resulting low statistics may force the use of too large radial bins, which directly affects the ability of detecting the cusp. Also the exact definition of the innermost cluster region where the cusp manifests itself

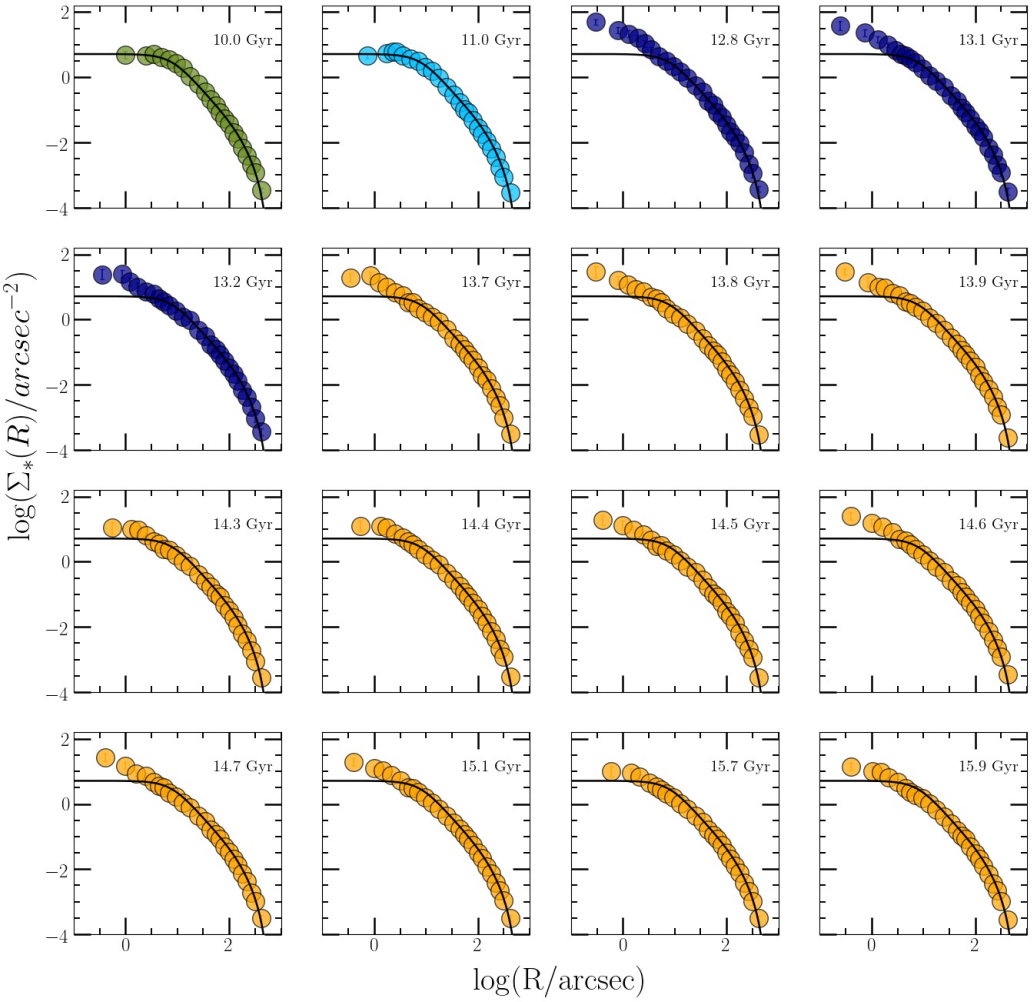

Figure 2.4: Comparison among the projected star density profiles measured during the latest stages of dynamical evolution, illustrating the appearance and persistence of the central cusp. All the profiles are normalized to the density measured at $R = 65''$ in the 10 Gyr snapshot, and the black solid line is the best-fit King model to the 10 Gyr density profile. The color code is as in Figure 2.1: cyan for pre-CC snapshots, blue for the CC phase, and yellow for post-CC stages and the snapshot time is labelled in each panel.

can affect the significance of the deviation from a King (centrally flat) model. This region is not known *a priori* and different assumptions about its extension might

lead to either an over-, or under-estimate of the cusp steepness. All this raises the need for new indicators of the internal dynamical state of dense stellar systems, not depending on the detection of a central density cusp or lack thereof.

2.3. The Normalized Cumulative Radial Distribution

Similar to the route followed to refine the definition of the "dynamical clock" based on BSSs (compare, e.g., Ferraro et al., 2012 with Lanzoni et al., 2016 and Ferraro et al., 2018a), here we explore a new way to infer the dynamical evolutionary stage of a GC using the normalized cumulative radial distribution (nCRDs) of its stellar population. In particular, for every simulation snapshot, we consider all the stars brighter than a threshold $V_{\rm cut}$ located within a projected distance R_n from the center, and we determine their nCRD. By construction, this function varies between 0 (at $R = 0$) and 1 (at $R = R_n$), describing, for each value of R, the percentage of stars within that distance from the center (i.e., the number of stars counted within R normalized to the total number of stars within R_n). The magnitude cut has the purpose of mimicking the analysis of observed data sets, where it is needed to avoid photometric incompleteness biases and/or is set by the exposure time of the available images. Consistently with many observational studies, we adopted $V_{\rm cut} = V_{\rm TO} + 0.5$. The choice of a normalization radius (R_n) has the aim to refer the analysis to the same *physical* region in all snapshots, thus allowing a direct comparative evaluation of the effects of dynamical evolution in clusters of different sizes and in different dynamical stages. We built the nCRDs for several values of R_n, concluding that $R_n = 0.5 \times r_h$ is the best choice, because it maximizes the morphological differences that dynamical evolution imprints on the nCRD (see below), while still providing large statistics. Indeed, $0.5 \times r_h$ is a distance from the center small enough to be highly sensitive to dynamical evolutionary effects (which are strongest in the most central regions) and large enough to include large samples of stars. We emphasize that r_h is defined as the (tridimensional) radius of the sphere that includes half the total cluster mass, while $R_n = 0.5 \times r_h$ is the projected distance from the center within which selecting the stars to build the nCRD. While r_h is not directly observable, its value is unambiguously obtained from the King model that, in projection, best-fits the observed density profile. To avoid the arbitrariness of approach (2) to the fit of the star density profile (see discussion in Section 2.2), for all the snapshots we adopted the value of r_h obtained from the King model that best reproduces the entire density distribution (see an example in the central panel of Figure 2.2).

Figure 2.5 shows the nCRDs of all the considered snapshots, plotted with different colors according to the dynamical state, as in Fig.2.1. As can be seen, the nCRDs differ one from the other and they do not appear to be randomly arranged: a nice

progression of color groups following the aging sequence defined in Fig.2.1 is clearly visible, from green (early stages), to cyan, blue, and yellow (late, post-CC stages). This indicates that the nCRD of the cluster population is sensitive to the parent cluster dynamical age. As a consequence, the dynamical stage of a GC should be measurable from an appropriate parametrization of the morphology of its nCRD.

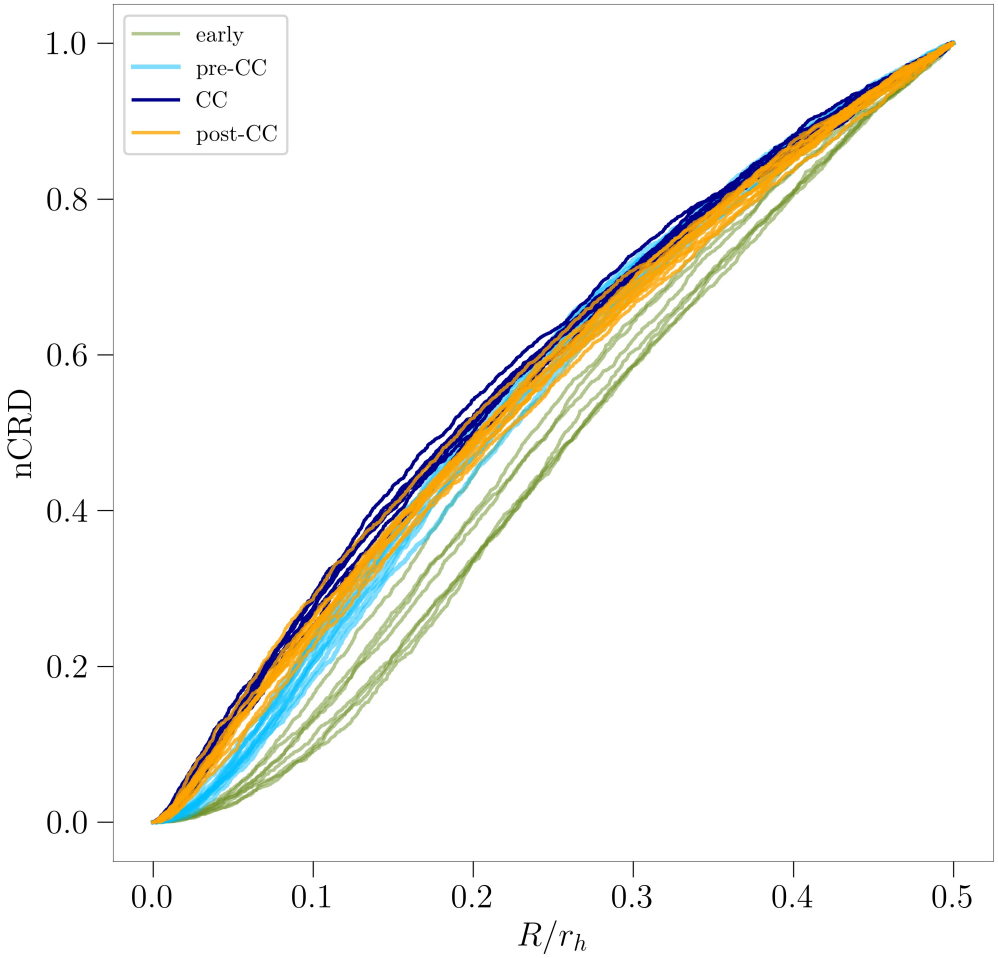

Figure 2.5: Normalized cumulative radial distributions of all the stars with $V \leqslant V_{\rm TO}+0.5$ and $R < 0.5\times r_h$, for all the analysed simulation snapshots. The nCRDs are plotted according to the color code adopted in Fig. 2.1: from early times (green), to pre-CC stages (cyan), the CC phase (blue), and the post-CC gravothermal oscillation epoch (yellow).

2.4. Defining the new parameters

The result shown in Figure 2.5 clearly shows that the cluster dynamical aging is imprinted in the morphology of the nCRD of its stellar population. Both the per-

centage of stars within a given distance from the cluster center and the growth rate of the nCRD as a function of the clustercentric distance appear significantly different at different stages of dynamical evolution. Hence, both these quantities, in principle, could be used to quantify the dynamical state of a GC. Not surprisingly, the differences among the nCRDs appear more pronounced in the innermost radial portion of the system, where the effects of dynamical evolution are known to be stronger. We thus defined the following three parameters to quantify the nCRD differences:

1) A_5 – It is defined as the area subtended by each nCRD between the center ($R = 0$) and a projected distance equal to 5% the tridimensional half-mass radius ($R = 0.05 \times r_h$), as illustrated by the shaded region in the left-hand panel of Figure 2.6. Because of the progressive increase of the central density during dynamical evolution, A_5 is expected to increase with time.

2) P_5 – It is defined as the value at $R = 0.05 \times r_h$ of the nCRD defined as above and it is illustrated in the central panel of Figure 2.6. The progressive contraction of the system toward CC translates into a centrally steeper nCRD and, as a consequence, also the value of this parameter is expected to increase as a function of the cluster dynamical age.

3) $S_{2.5}$ – It is defined as the slope of the straight line tangent to the nCRD at a projected distance equal to 2.5% the half-mass radius ($R = 0.025 \times r_h$). Operationally, a polynomial function (in the form $y = a \times x^3 + b \times x^2 + c \times x$, with $x = R/r_h$) is fitted to the nCRD to smooth out its noisy behavior, and $S_{2.5}$ is the slope of the straight line tangent to the polynomial (see the red and the blue lines, respectively, in the right panel of Figure 2.6). Since our analysis showed that the most relevant changes in the growth rate of the nCRD occur in the very internal region of the system, $S_{2.5}$ has been defined at an even smaller projected distance from the center with respect to the other two parameters (namely, at 2.5%, instead of 5%, the half-mass radius). It quantifies the radial growth rate of the nCRD and, similarly to A_5 and P_5, it is expected to increase as function of the cluster dynamical age.

Following the definitions above, we measured the three parameters for all the snapshots under investigation. To estimate their uncertainties we took into account the dominant source of error, namely the uncertainty of the half-mass radius as obtained from the King fit to the density profile. To this end, for every snapshot we re-determined the nCRD using all the stars with $V < V_{\rm cut}$ included within $R_n = 0.5 \times (r_h + \epsilon_h^+)$, where ϵ_h^+ is the upper error on r_h, and we measured the corresponding values of the three parameters. The difference between this value and that obtained for $R_n = 0.5 \times r_h$ is then adopted as upper error on each parameter. To estimate the lower uncertainty we repeated the analogous procedure adopting $R_n = 0.5 \times (r_h - \epsilon_h^-)$, ϵ_h^- being the lower error on r_h. Figure 2.7 shows the time evolution of A_5 (top panel), P_5 (central panel), $S_{2.5}$ (bottom panel). The

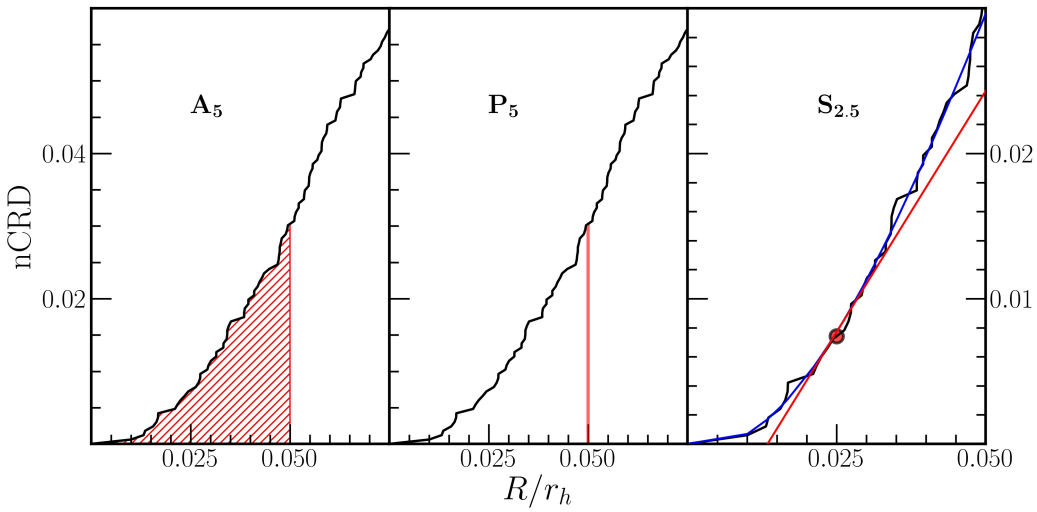

Figure 2.6: Definition of the three new diagnostics of dynamical evolution based on the nCRDs of the cluster stellar population shown in Figure 2.5. A_5 is the area subtended by the nCRD within a projected distance equal to 5% the half-mass radius (red shaded region in the left panel). P_5 is the percentage of stars measured at $R = 0.05 \times r_h$, corresponding to the value of the nCRD at this clustercentric distance. $S_{2.5}$ is defined as the slope of the straight line tangent to the nCRD at $R = 2.5\%$ the half-mass radius, as illustrated in the right panel: operationally, it is measured from the tangent line (red line) at $R = 0.025 \times r_h$ (large red circle) to the polynomial function that best reproduces the nCRD (blue line).

time is normalized to $t_{\rm CC}$, which is also marked by the vertical red dashed line, and the snapshots are plotted according to the color code defined in Figure 2.1. As expected, all the parameters show an increasing trend with time. In addition, the trend is strikingly similar in the three cases: an almost constant behavior is observed at the early evolutionary times (green points), then a rapid increase occurs during the pre-CC stage (cyan points), up to the achievement of maximum values at the CC epoch (blue points), followed by the post-CC gravothermal oscillations stage during which the parameters moderately fluctuate, but remain stable slightly below the maximum reached at $t_{\rm CC}$ (yellow points). To elaborate, A_5 remains constant around $A_5 = 0.001$ for most of the time ($t \lesssim 0.8 t_{\rm CC}$), then it rapidly increases by a factor of 7 at CC, and it slightly decreases and fluctuates around $A_5 \sim 0.005$ later on. Similarly, the P_5 parameter stays essentially constant around $P_5 \sim 0.03$ in the early epochs, then the increasing stellar density in the cluster central regions increases it by a factor of 5 at CC, and finally the parameter stabilizes (with some fluctuations) around $P_5 \sim 0.12$ during the post-CC phase. An analogous evolutionary pattern is observed also for $S_{2.5}$: it is stable at $S_{2.5} \sim 0.3$ at early times, then it shows a rapid increase, by a factor of 6, reaching $S_{2.5} \sim 1.8$ at CC, and it further settles around

$S_{2.5} \sim 1.3$, with the usual fluctuations, during the gravothermal oscillation stage.

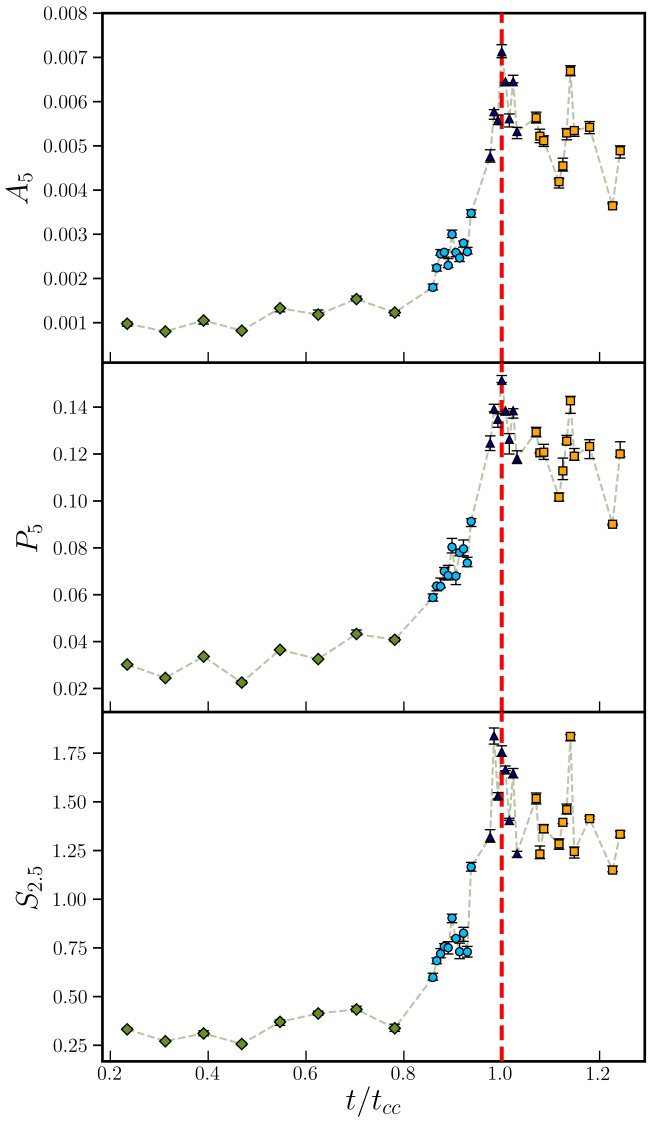

Figure 2.7: Time evolution of the nCRD parameters defined as in Figure 2.6 (see also Section 2.4): A_5 (top panel), P_5 (central panel) and $S_{2.5}$ (bottom panel). Time is normalized to $t_{\rm CC}$, which is also marked by the vertical red dashed line. The symbol shapes and colors are as in Figure 2.3. All the three parameters show a increasing trend with time, reaching the peak value at CC (blue triangles) and then remaining large and essentially constant, with some fluctuations, during the late, gravothermal oscillation stage (yellow squares).

2.5. Sensitivity of the parameters to the assumptions

Of course, the exact shape of the nCRD (and, consequently, the values of the newly defined parameters) depends on the assumptions used for its construction, in particular the values of radial distance (R_n) and the magnitude cut ($V_{\rm cut}$) adopted for the star sample selection. In this section we thus explore the effects of modifying these values.

The (small) importance of varying R_n can be already caught from the size of the errors associated to each parameter (see error bars in Fig. 2.7). However, we also investigated the effect of a stronger variation, starting from the evidence that the King model best-fitting a pre-CC snapshot (in particular, the one extracted at 10 Gyr) well reproduces also the density profile observed at later times once the central cusp is excluded (see Fig. 2.4). We thus assumed $R_n = 0.5 \times 65''$ for all snapshots, this value being half the cluster half-mass radius at 10 Gyr. The corresponding values of the three parameters are shown as triangles in Figure 2.8. The comparison with the values obtained by assuming the best-fit half-mass radius of each snapshot (circles, the same as in Fig. 2.7) clearly confirms that the impact of R_n is negligible, at least for variations as large as $\sim 15\%$ of its value.

As for the magnitude cut, the results shown so far have been obtained by adopting a relatively bright threshold, just half magnitude below the MS-TO: $V_{\rm cut} = V_{\rm TO} + 0.5$. This was done to allow the observational measure of the nCRD parameters also in high-density GGCs, where reaching deeper limits with a reasonable level of completeness in the innermost regions of the system is still very hard, even with HST data. However, a fainter magnitude cut would include a significantly larger sample of stars, thus offering the advantage of a larger statistics. We thus explored the nCRDs obtained with $V_{\rm cut} = V_{\rm TO} + 2$ and measured from them the three parameters defined above, to check whether they trace more or less efficiently the cluster dynamical aging. Figure 2.9 shows the comparison between the time evolution of A_5 as obtained for the two magnitude cuts: $V_{\rm cut} = V_{\rm TO} + 0.5$ in black, a limit 1.5 magnitudes fainter in red. As can be seen, the overall trend is perfectly consistent in the two cases, thus confirming that the increase of the A_5 parameter as a function of time does not depend on the details of its own definition, but traces, instead, the structural changes of the nCRD due to the effects of dynamical evolution. Indeed, the trend during the early and pre-CC phases is virtually indistinguishable in the two cases, except for a less noisy behavior for $V_{\rm cut} = V_{\rm TO} + 2$ due to the increased statistics. Instead, the sensitivity of A_5 during the CC and the post-CC phases appears systematically reduced in the case of the deeper magnitude cut, with an increase of a factor of ~ 5 (instead of ~ 7) with respect to the values measured in the early snapshots. This is consistent with the fact that assuming a fainter magnitude threshold corresponds to including stars of smaller masses in the analysis, which are less affected by the dynamical evolutionary processes occurring in the cluster center. Analogous dependencies on the adopted magnitude cut are also found for

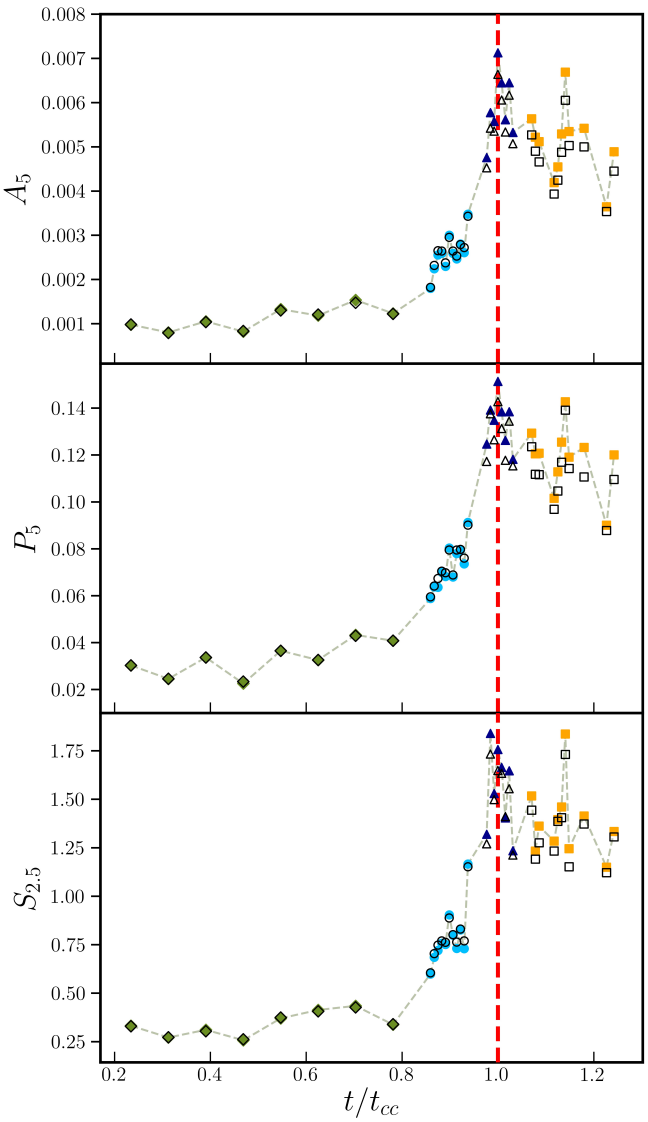

Figure 2.8: Comparison between the parameters obtained from nCDRs built using $R_n = 0.5 \times r_h$ (colored solid symbols, the same as in Fig. 2.7), and those obtained from nCDRs built using $R_n = 0.5 \times 65''$ (empty symbols).

the parameters P_5 and $S_{2.5}$. Hence, as global result, we conclude that the sensitivity of the nCRD parameters to the cluster dynamical evolution tends to decrease with fainter magnitude cuts, and $V_{\rm cut} = V_{TO} + 0.5$, in spite of smaller numbers of stars, looks as the best compromise between large enough statistics and good efficiency to distinguish among different dynamical evolutionary stages.

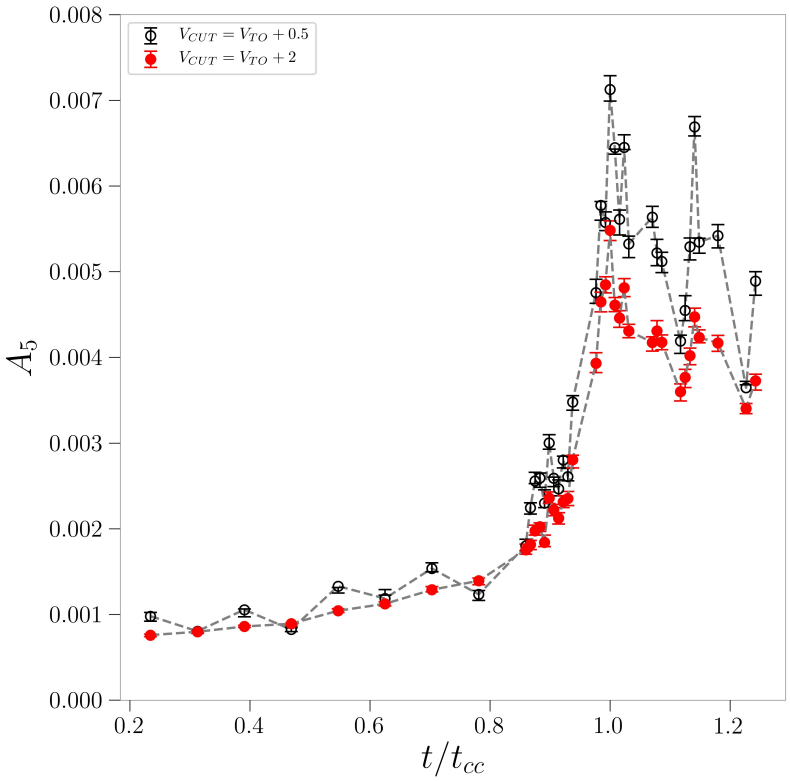

Figure 2.9: Time evolution of the A_5 parameter measured from the nCRDs built with different magnitude cuts: $V_{\rm cut} = V_{\rm TO} + 0.5$ (empty black circles) and $V_{\rm cut} = V_{\rm TO} + 2$ (solid red circles).

2.6. Simulations with different initial conditions

The parameter space of possible initial conditions for realistic simulations of GCs is huge, including variations in the initial values of W_0, scale radii, number of stars, primordial binary fraction, dark remnant retention fraction. Hence, the next chapters will be devoted to accurately explore the effects that different initial conditions can have on the values of the three proposed new indicators and their time evolution.

In this section we present just a first investigation of this issue, by analyzing two additional simulations where only one initial condition is varied at a time, with respect to the reference run discussed in the main text (hereafter, REF run). In the first one (hereafter, W05 run), we changed the value of the King dimensionless potential ($W_0 = 5$), while keeping the same initial number of stars and half-mass radius, and assuming the same galactocentric distance as in the reference simulation. In the second run (hereafter, 250K run), we have followed the evolution of a system with half of the number of particles (N=250K) and kept the same W_0, half-mass radius, and galactocentric distance used for the REF simulation. The initial mass

in the W05 run is the same as in the REF model, while it is $\sim 1.6 \times 10^5 M_\odot$ initially in the 250K simulation (and $\sim 5.7 \times 10^4 M_\odot$ at 12 Gyr). Figure 2.10 shows the time evolution of the 1% Lagrangian radius of these two simulations. The overall trend is very similar to that shown in Figure 2.1 for the REF run. However, CC occurs earlier (at $t_{CC} = 9.7$ Gyr) in the case of the less massive cluster (250K run; left panel), while it is delayed by almost 1 Gyr for the initially less concentrated cluster (W05 run, where $t_{CC} = 13.4$ Gyr; right panel). The vertical lines mark the time snapshots extracted from these simulations, which have been analyzed following the same procedures and adopting the same assumptions discussed in the main text for the REF simulation.

The resulting time dependence of the three parameters is shown in Figure 2.11, where the yellow circles correspond to the 250K simulation, the blue circles refer to run W05 and, for the sake of comparison, we overplotted also the results of the REF simulation in green (same points as in Figure 2.7). Along the x-axis, the time is normalized to the respective values of t_{CC}. The comparison shows that the differences among the adopted initial conditions have a negligible effect on both the absolute values and the time dependence of the three parameters, thus further reinforcing the conclusion that A_5, P_5, and $S_{2.5}$ are powerful indicators of GC internal dynamical evolution.

2.7. Discussion and summary

In this chapter we have presented the first results of a study aimed at defining new empirical parameters that use the inner radial distribution of cluster stars to characterize the different dynamical evolutionary phases experienced by dense stellar systems. To this end, we have used a Monte Carlo simulation following the 'typical' dynamical evolution of a GC, from an initial progressive contraction of the core, to the CC event, and the gravothermal oscillations during the post-CC phase.

A total of 38 time snapshots sampling these different stages have been extracted from the simulation and analyzed by closely following the steps usually taken in the analysis of an observational data set. We used only projected (instead of three-dimensional) quantities and a reasonable cut in magnitude to mimic the observational approach, where photometric incompleteness and/or exposure times can severely limit the extension in magnitude of the sample. In addition, the same approach used in observational works has been applied to the numerical data for determining the star density profile and its best-fit King solution. The analysis of the star density profiles extracted from the simulation shows that the central cusp developing during CC is not erased by the subsequent gravothermal oscillations; hence the central cusp remains as a stable feature and characterizes the star density profile also during the post-CC phase. However, a preliminary inspection of the simulations shows that the slope of the central cup can vary during the post-CC phase and its operational detectability from observed data may present some difficulties.

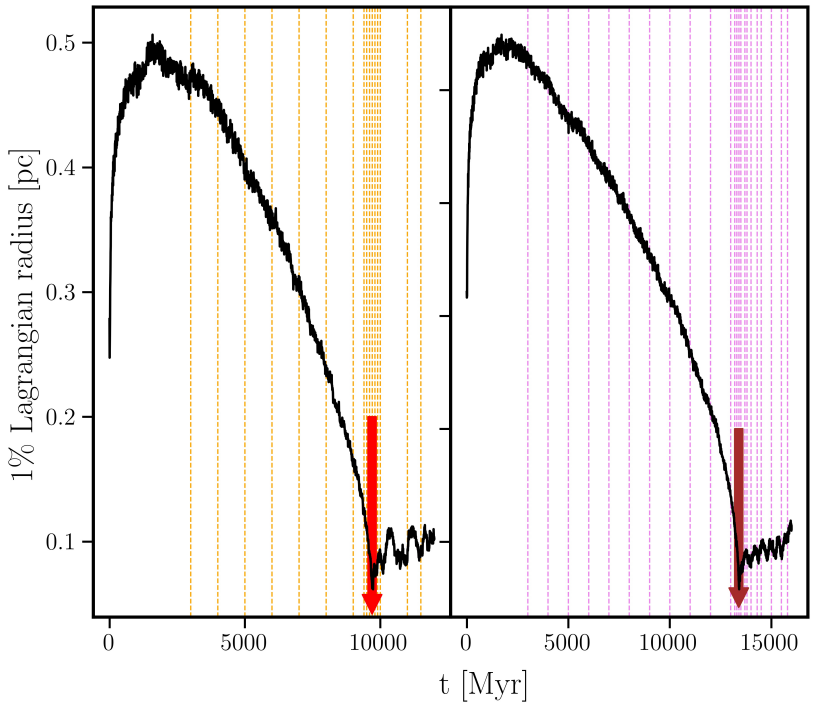

Figure 2.10: Time evolution of the 1% Lagrangian radius (in pc) in 250K simulation (yellow, left panel) and the W05 run (magenta, right panel). The vertical lines correspond to the time snapshots for which we determined the values of A_5, P_5 and $S_{2.5}$ shown in Figure 2.11. The CC time is marked with a large red arrow: $t_{\rm CC} = 9.7$ Gyr in the 250K run (left panel), $t_{\rm CC} = 13.4$ Gyr in the W05 simulation (right panel).

We then used the simulation to explore new ways of determining the dynamical evolutionary stage of star clusters from the global properties of their stellar population (instead of specific exotic species such as, e.g., BSSs). To this purpose we constructed and analyzed the nCRD of each snapshot using all the stars brighter than 0.5 magnitude below the MS-TO and located within a projected distance $R_n = 0.5 \times r_h$ from the center (see Section 2.3). These showed an intriguing level of sensitivity to the dynamical evolution of the cluster. Indeed, the shape of the nCRDs varies significantly as a function of the cluster dynamical state and allows a clear identification of the various fundamental stages of a cluster evolution (the pre-CC, the CC, and the post-CC phases). We have introduced three parameters (named A_5, P_5 and $S_{2.5}$) that quantify the morphological changes of the nCRD as a function of time and turned out to be effective diagnostics of the cluster dynamical age. The three parameters show similar trends with time, mirroring the host cluster dynamical evolution. After an early phase (lasting ~ 8 Gyr in our simulation) in which they are essentially

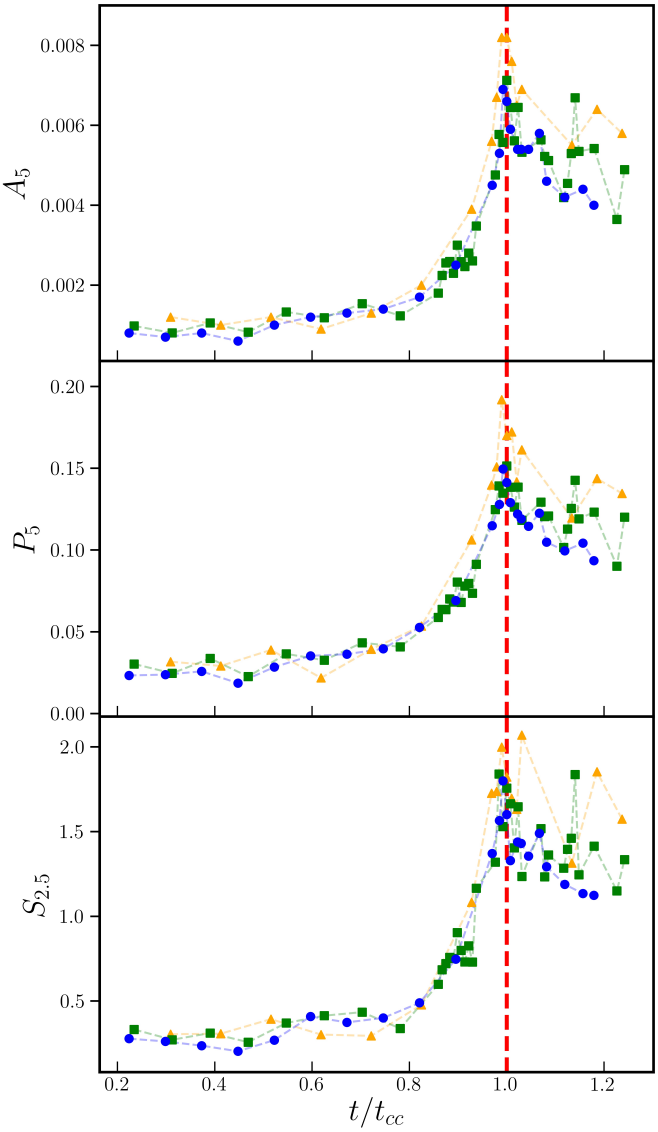

Figure 2.11: Time evolution of the nCRD parameters in simulations 250K (yellow triangles), W05 (blue circles), and REF (green squares, the same points as in Figure 2.7). From top to bottom, the three panels refer to parameters A_5, P_5 and $S_{2.5}$. Time is normalized to each respective value of $t_{\rm CC}$.

constant, they rapidly increase reaching a maximum at the CC epoch. We estimate that as the cluster approached CC, they grow by a factor of 5-7. The post-CC evolution yields to a slight decrease of the values of all the parameters. However, in spite of some fluctuations, their average value remains significantly larger than those typical of the pre-CC phase. From an observational point of view this is one of the most relevant aspect. Indeed, the fact that the values of the parameters in the post-CC stages remain significantly larger than those in the early phases offers

the concrete possibility of clearly distinguishing highly evolved GCs also in those cases where the central density cusp detection is uncertain.

After this first exploratory work, in the following chapters we will broaden the range of initial conditions and study their impact on the empirical parameters defined here. We will also include populations of primordial binaries, which are known to halt the core contraction earlier in the cluster evolution and at lower concentrations (see, e.g., Vesperini & Chernoff, 1994; Trenti et al., 2007; Chatterjee et al., 2010). The main differences between the values of A_5, P_5, and $S_{2.5}$ in simulations with and without primordial binaries are expected during the advanced phases of the evolution, towards CC and post-CC, when the milder contraction of the clusters with primordial binaries might lead to a different and/or less extreme evolution of these parameters. The study presented here will also be further extended to explore the effects of different retention fractions of dark remnants (neutron stars and black holes; see, e.g., Alessandrini et al., 2016; Giersz et al., 2019; Kremer et al., 2020, 2021; Gieles et al., 2021, for some studies on the dynamical effects of dark remnants).

Chapter 3

Effect of Initial Binary fraction and Dark Remnants

Mainly based on:
Bhat et al. (2023), ApJ, 945, 164

This chapter is specifically aimed at quantifying the effect of primordial binaries and stellar-mass black holes on the time evolution of the three parameters defined in Chapter 2. The chapter is organized as follows. In Section 3.1 we describe the initial conditions of the Monte Carlo simulation runs and the methodology adopted in the following analysis. In Section 3.2 we present the determination of the projected star density profile and the adopted King fit procedure. Section 3.3 describes the method and assumptions used for the construction of the nCRDs, and the definition and properties of the three nCRD dynamical indicators in the case of three different fractions of primordial binaries. In Section 3.4 nCRD parameters are compared with the expected values of the same parameters from the King model. Section 3.5 is devoted to the analysis of the effects induced by a sub-system of black holes. The summary and conclusions of the work are discussed in Section 3.6.

3.1. Methods and Initial conditions

In this chapter, we use five Monte Carlo simulations performed with MOCCA code (Hypki & Giersz, 2013; Giersz et al., 2013) to thoroughly follow the dynamical evolution of GCs with different primordial binary fractions and dark remnant retention fractions. In addition to two-body relaxation and tidal truncation effects, the code also models stellar and binary evolution by means of the SSE and BSE codes (Hurley et al., 2000, 2002), thus providing, for each star at any evolutionary time, not only the position and the velocity, but also the mass, and the $B-$ and $V-$ band magnitudes. One of the simulation is the same as presented in Chapter 2, and

it is used here for comparison purposes. It initially has 500K stars with masses ranging between $0.1M_{\odot}$ and $100M_{\odot}$, following a Kroupa (2001) mass function, and distributed as a King (1966) model with dimensionless central potential $W_0 = 6$. Supernova kicks are assumed to follow a Maxwellian distribution with dispersion equal to 265 km s^{-1} (Hobbs et al., 2005). The cluster is tidally underfilling, with a three-dimensional half-mass radius $r_h = 2$ pc and a Jacobi radius equal to 61 pc (corresponding to the value that the system would initially have if orbiting at a Galactocentric distance $R_g = 4$ kpc). No primordial binaries are included in this run, which will be referred as "BF0" throughout the chapter. Two other simulations have been performed using the same initial conditions except for their primordial binary fraction; these simulations start with a total number of single and binary stars, $N = N_s + N_b = 500$ K and binary fraction, $N_b/(N_s + N_b)$ equal to 10% and 20% in the runs that will be referred to as "BF10" and "BF20", respectively. The distribution of binary properties (as mass ratio, period and eccentricity) are set according to the eigenevolution procedure described in Kroupa (1995) and Kroupa et al. (2013). The same initial conditions as those of the BF0 model, but with a reduced kick velocity for stellar black holes, have been used also in the fourth simulation (which we name "DRr"). The fifth simulation, hereafter referred to as "DRe", has slightly different initial conditions: the initial cluster density profile follows that of a King model with $W_0 = 7$, $r_h = 1$ pc, $R_g = 2$ kpc. It starts with 10% primordial binary fraction and similar to the DRr run, it has a reduced kick velocity for the stellar mass black holes. With the DRr and DRe simulations we explore the effect of dark remnants (retained black holes) on the cluster evolution and the time dependence of the three parameters introduced in Chapter 2. The initial conditions of all the simulations are listed in the Table 3.1.

While the analysis of the DRr and DRe simulations is addressed separately in Section 3.5, Figure 2.1 shows the time evolution of the 1% Lagrangian radius ($r_{1\%}$, i.e., the radius including 1% of the total cluster mass) for the BF0, BF10, and BF20 runs. This clearly illustrates the evolution of the cluster's inner structure and how it is affected by the presence of binary systems. In all cases, an initial expansion (driven by heavy mass loss from young, massive stars) is followed by a phase where two-body relaxation becomes dominant. This leads to a progressive contraction of the core, which culminates in the CC event when $r_{1\%}$ reaches the lowest value (red arrows in the figure). The CC time, t_{CC}, is approximately equal to $t_{\rm CC} = 12.8$ Gyr, $t_{\rm CC} = 14.4$ Gyr, and $t_{\rm CC} = 13.7$ Gyr for the BF0, BF10, and BF20 simulations, respectively. As apparent and as expected, the overall effect of primordial binaries is to reduce the depth of CC and quench the post-CC gravothermal oscillations. In fact, if no primordial binaries are present, the system undergoes a phase of deep CC, until enough binaries are dynamically formed in the core and stop the contraction. Conversely, in a cluster with substantial primordial binaries, the core contraction is hindered by binary burning (binaries acting as energy sources), which prevents the system from undergoing deep CC. Indeed, Figure 2.1 shows that the rapid phase of deep contraction immediately before CC is almost bypassed, and the CC event

is reached in a smoother way in the BF10 and BF20 runs. While $r_{1\%}$ shrinks by a factor of 8 in the BF0 simulation, the factor is reduced to ~ 3 in the BF10 run, and to 2.5 in the case of 20% primordial binaries. A clear phase of gravothermal oscillations, during which $r_{1\%}$ undergoes cyclic expansions and contractions, is well distinguishable after CC in the BF0 simulation, while it is absent in our simulations with primordial binaries.

To more quantitatively examine the impact of primordial binaries on the cluster dynamical evolution, in the following sections we extend the same analysis presented in Chapter 2 (for the BF0 run) to the BF10 and BF20 cases. Here we summarize the main aspects of the work, while more details about the adopted procedures can be found in the previous chapter. As in Chapter 2, we have extracted different time snapshots corresponding to various phases of the cluster dynamical evolution in the three runs. They are marked in Figure 2.1 with vertical dashed lines, color-coded as follows: *green* color for the early slow contraction phase, *cyan* for the subsequent phase leading to CC, *blue* for the CC phase, and *yellow* for the the post-CC phase. Following the approach adopted in Chapter 2, every snapshot is assumed to be a possible configuration of a real cluster observed in different stages of its dynamical evolution, and to be as much as possible consistent with real cases, the analysis of the simulated data has been done from the point of view of an observer. Thus, standard procedures and approximations adopted in observational works have been applied: in each snapshot, the simulated cluster is projected onto a 2D plane, and a distance of 10 kpc from the observer has been assumed to transform the distances from the centre of the system from parsecs to arcseconds. In addition, binary systems have been treated as "stellar blends", consistently with the fact that the two components cannot be individually resolved at the distances of Galactic GCs. Hence, the magnitude of each binary system has been determined by summing up the luminosities of the two stellar components.

Table 3.1: Initial conditions of the simulations

Name	W_0	BF	r_h(pc)	R_g(kpc)	other
BF0	6	0	2	4	..
BF10	6	10	2	4	..
BF20	6	20	2	4	..
DRr	6	0	2	4	Reduced kick velocity for black holes
DRe	7	10	1	2	Reduced kick velocity for black holes

Values of the dimensionless central potential (W_0), binary fraction (BF), half-mass radius (r_h), and Galactocentric distance (R_g) adopted as initial conditions in the five Monte Carlo simulations analyzed in this chapter (see their name in the first column).

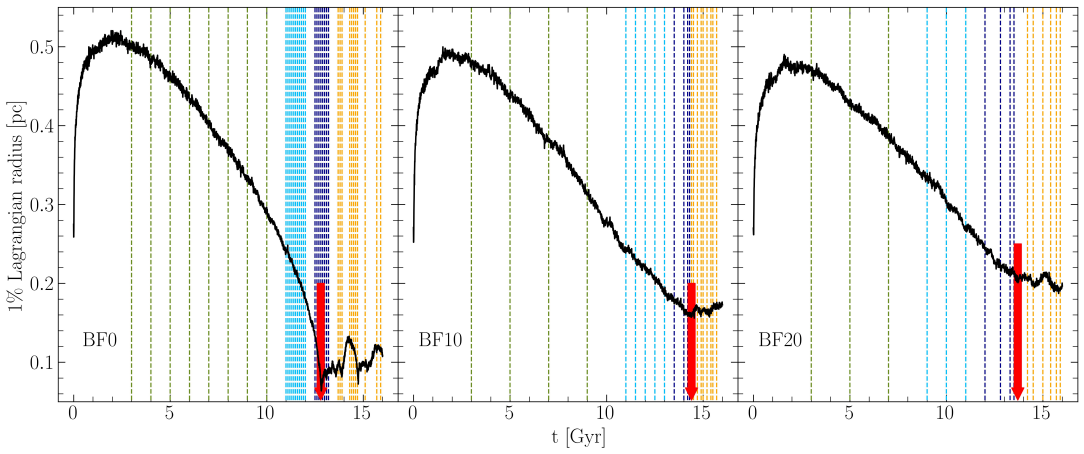

Figure 3.1: Time evolution of the 1% Lagrangian radius (black line) of the three simulations differing only in their primordial binary fraction: no primordial binaries in run BF0 (left panel), 10% and 20% initial binary fractions in simulations BF10 and BF20 in the central and right panels, respectively. The vertical lines in each panel mark the time snapshots extracted and analyzed in each run, color-coded following the different evolutionary stages of the system: green, cyan, blue and yellow colors for early, pre-CC, CC, and post-CC phases, respectively. The time of CC ($t_{\rm CC}$ = 12.8, 14.4, and 13.7 Gyr for BF0, BF10, and BF20, respectively) is marked with a large red arrow in all the panels.

3.2. Projected density profiles

As part of the analysis, we first investigate the effect of different initial binary fractions on the development and evolution of an inner density cusp through various epochs of the cluster dynamical evolution. To construct the density profile of each extracted snapshot, we followed the same procedure described in Chapter 2 and adopted in several observational works (e.g., Miocchi et al., 2013). It essentially consists of counting the number of stars in concentric annuli around the cluster center, and dividing it by the area of each radial bin. We then used a χ^2 method to determine the King (1966) model best-fitting the "observed" density profile, by exploring a grid of models with dimensionless parameter W_0 (which is proportional to the gravitational potential at the center of the system) varying between 4 and 10.75 in steps of 0.05. This corresponds to a concentration parameter c spanning the interval between 0.84 and 2.5, with c being defined as the logarithm of the ratio between the truncation or tidal radius of the system (r_t), and the King radius r_0, which is the characteristic scale-length of the model: $c = log(r_t/r_0)$. The King model profile well describes the density distribution of the simulated clusters, except for the snapshots close to and beyond CC, when a density cusp develops in the center. In these cases, the model still provides a very good fit to the external portion of the profile (cyan circles and red lines in Figure 3.2), while the trend in the innermost

$\sim 5''$ is better fitted with a power-law (yellow circles and dashed lines in the figure). A density cusp always develops around the CC phase in all the simulations, and, once formed, it never disappears. However, while it is prominent in the BF0 run, it becomes shallower and sometimes hardly distinguishable in the cases of 10% and, ever more so, 20% primordial binaries. Thus, the slope of the density cusp developed in the CC stage is affected by the binary content of the cluster, consistently with the effect discussed above on the time evolution of the 1% Lagrangian radius (Fig. 2.1): star clusters with larger primordial binary fractions experience shallower CC and develop less steep cusps in the star density profile at the CC epoch (see also Vesperini & Trenti, 2010).

Of course, while properly reproducing the external portion of the density profile, the King parameters obtained from the fit after the exclusion of the innermost $5''$ cannot be used as an appropriate description of the overall cluster structure. In addition, the choice of $5''$ is somehow arbitrary, and by changing this value, also the resulting best-fit King model may change. To overcome these issues, we thus determined the King models that best-fit the entire density profile of each snapshot, and we adopted the corresponding structural parameters in the following analysis (for more details, see Section 3.1 and Figure 2 in Chapter 2).

3.3. The nCRD dynamical indicators

Here we extend the analysis presented in Chapter 2 to the case of GCs including a population of primordial binary systems, to test how the newly defined dynamical indicators, quantifying the morphology of the nCRD of cluster stars, depend on the primordial binary fraction. In the following, we therefore adopt the same methodology fully described in Chapter 2 and aimed at making the three parameters well measurable from observations.

3.3.1 Normalised cumulative radial distribution (nCRD)

For each extracted snapshot, to build the nCRD we selected all the stars brighter than $V_{\rm cut} = V_{\rm TO} + 0.5$ (with $V_{\rm TO}$ being the $V-$band magnitude of the main-sequence turn-off point), and located within a projected distance equal to $0.5 \times r_h$ from the centre. In the case of binary systems, we considered the combined magnitude of the two components, since all binaries remain unresolved (they are observed as stellar blends) at the distance of GCs. These choices are motivated by the fact that the same procedure will be applied in future investigations to observational data, for which proper magnitude selections are needed to avoid problems of photometric incompleteness, and a common radial cut in units of a physical scale-length (as r_h) is required to allow the comparison among stellar systems of different intrinsic sizes. More specifically, we defined $x = R/r_h$ and considered all the magnitude-selected stars located between $x = 0$ and $x = 0.5$. For any value of x, the nCRD is equal to

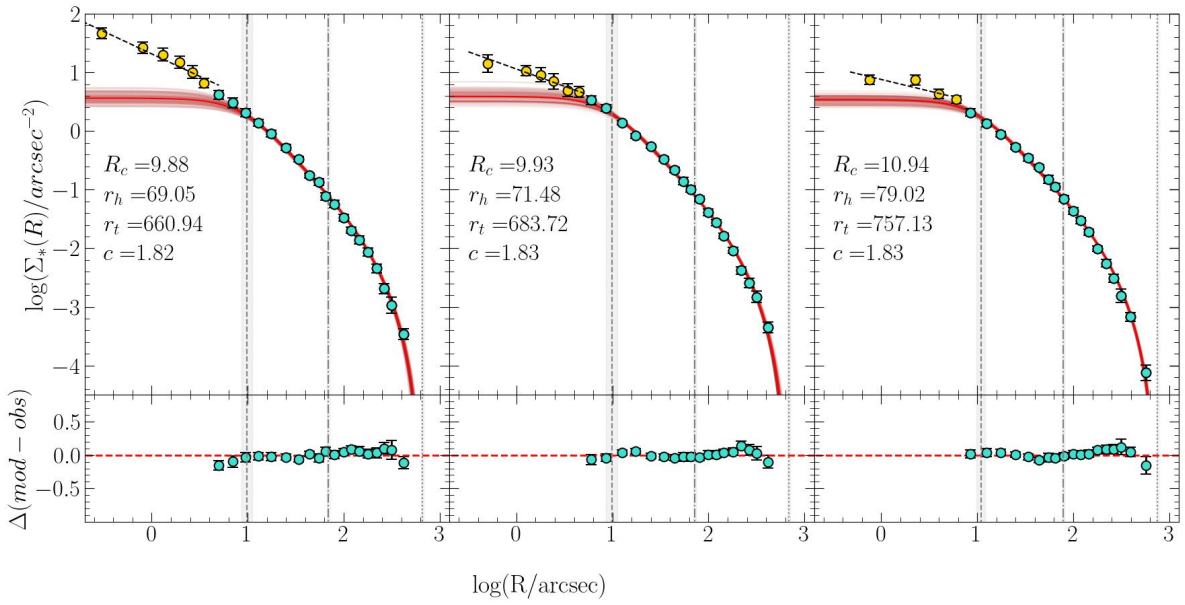

Figure 3.2: Projected density profile for the snapshots extracted at $t_{CC} = 12.8, 14.4$ and 13.7 Gyr in the BF0 (left panel), BF10 (central), and BF20 (right) simulations, respectively. The red solid lines correspond to the King models that best-fit the density profiles beyond 5″ from the center (cyan circles), while the innermost cusps (yellow circles) are best-fit by the dashed straight lines. The red shaded regions correspond to the uncertainty of the best-fit model. The vertical dashed, dotted-dashed and dotted lines mark, respectively, the core, half-mass and truncation radii calculated from the best-fit King models (see also the labels). The bottom panels show the residual between the best-fit model and the "observed" density profile.

the number of stars within x and is normalized by the total number of selected stars. Hence, by construction, the nCRD is a curve that monotonically increases from 0 at the centre ($x = 0$), to 1 at $x = 0.5$. The steeper it is, the more concentrated are the selected stars toward the center of the system.

Figure 3.3 shows the nCRDs thus obtained for all the snapshots extracted from the three simulations, color-coded as in Fig. 2.1. Clearly, the morphology of the nCRDs changes with time following the cluster dynamical evolution, with shallower curves (less centrally segregated stars) for early evolutionary times (green lines), and increasingly steeper functions for more advanced dynamical stages. These morphological differences are stronger in the BF0 case, and become progressively less pronounced in the BF10 and BF20 runs. This is another manifestation of the different depth of CC in the three cases (see Figure 2.1). In fact, in the absence of a primordial population, the binaries present in the cluster are limited to those dynamically generated in the core during the most advanced stages of evolution.

Hence, they have little effect on the progressive segregation of cluster stars toward the center. Conversely, in a system with a substantial fraction of primordial binaries, binary burning provides the energy needed to halt core collapse earlier. Thus, the primordial binary fraction does affect the extent of morphological differences imprinted in the nCRD by the internal dynamical evolution of the system.

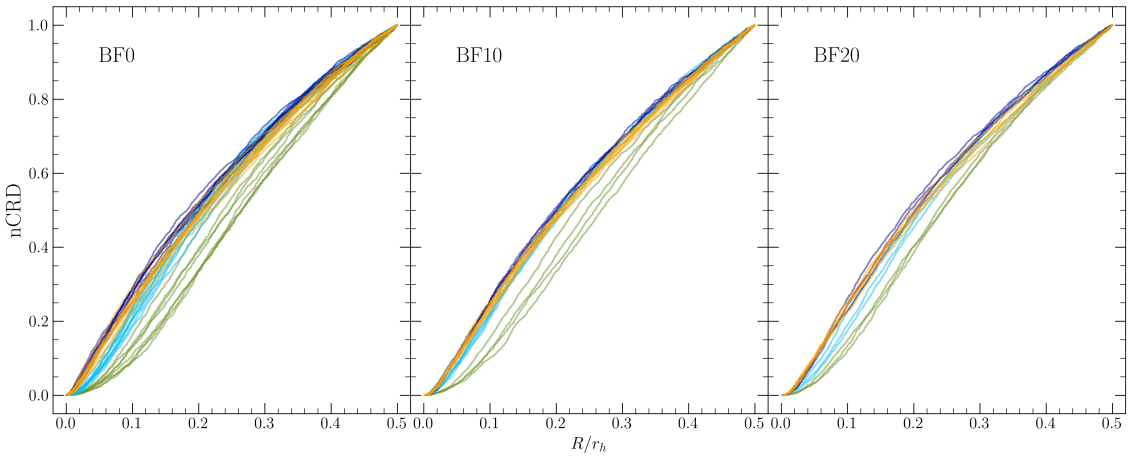

Figure 3.3: Normalised cumulative radial distributions (nCRDs) of stars brighter than $V = V_{\rm TO} + 0.5$ and located within $0.5 \times r_h$ from the center, for all the snapshots analysed in the BF0, BF10 and BF20 simulations (left, central and right panels, respectively). The color coding is the same adopted in Fig.2.1: early times (green), pre-CC stages (cyan), CC phase (blue), and post-CC epoch (yellow).

3.3.2 The A_5, P_5 and $S_{2.5}$ parameters

In Chapter 2 we defined[1] the following three parameters quantitatively describing the temporal variations of the nCRD caused by the cluster dynamical evolution:

- A_5 is the area subtended by each nCRD between the center and a projected distance equal to 5% r_h (hence, between $x = 0$ and $x = 0.05$, with $x = R/r_h$);
- P_5, is the value of the nCRD at 5% r_h ($x = 0.05$), which corresponds to the fraction of selected stars located within this distance from the centre;
- $S_{2.5}$ is the slope of the straight line tangent to the nCRD at 2.5% r_h (at

[1]While the definitions of the three parameters are exactly the same as in Chapter 2, we emphasize that here they are computed by using distances normalized to the half-mass radius $x = R/r_h$, while in Chapter 2 the adopted normalization was $0.5 \times rh$. This has no impact on the results and on the time evolution of the parameters; the only difference is that the values of A_5 plotted here are half of those published in Chapter 2, and those of $S_{2.5}$ are approximately twice the previous ones.

$x = 0.025$). More specifically, it is the slope of the tanget to the third-order polynomial function that best-fits the nCRD (the fit being introduced to smooth out the noisy behavior of the nCRD itself).

They are all defined in the very central region of the cluster, to best sample the radial distance where the dynamical effects responsible for the central density growth during the core contraction and the CC phase are most relevant, and the nCRD morphological differences are maximized. The major source of error for the parameters is the uncertainty in the value of the half-mass radius derived from the King models. However, as discussed in Chapter 2, the size of these errors is negligible and they are therefore ignored here.

By construction, these parameters quantifies the evolution of the nCRD and they increase as a function of the cluster dynamical age. This is clearly shown in Figure 3.4 (top, middle and bottom panels for the A_5, P_5, and $S_{2.5}$ parameters, respectively). In the early dynamical phases (green symbols), each parameter shows a nearly constant behavior, taking essentially the same (small) values regardless of the primordial binary fraction. Then, they increase in the pre-CC phase (cyan symbols), reach a peak at the CC epoch (blue symbols), and shows some fluctuations during the post-CC stage (yellow symbols), never receding to the initial low values. The gradual growth with time of the parameters is most pronounced in the BF0 simulation (left panels), and becomes milder for larger binary fractions (central and right panels). This is indeed expected for the same reasons discussed above, reflecting the shallower CC and the lack of gravothermal oscillations in the models with 10% or 20% primordial binary fraction. Nevertheless, the clear increasing trend with time confirms the effectiveness of these parameters as proper tracers of the dynamical aging of the system.

For a deeper investigation of these dynamical indicators and to allow a direct comparison with observations, we removed the explicit dependence on time by plotting one parameter against another. The three possible combinations are shown in Figures 3.5, 3.6, and 3.7, where the dashed lines are the polynomial fits to the distributions of points in the BF0 case (left panels), and they are reported for reference also for the BF10 and BF20 runs in the central and right panels, respectively. As shown by these figures, the measured values gradually move from the bottom-left to the top-right corner of each diagram for increasing dynamical age, up to CC (i.e., from green, to cyan, to blue colors). Then, in the post-CC stage (yellow symbols) they tend to be smaller than or mixed with those obtained during CC. The point distributions follow essentially the same relation (dashed lines in the figures) in all the simulations, irrespective of the binary fraction. In principle, then, just from the measure of two parameters, these diagrams allow one to understand whether a stellar system is in an early, intermediate or advanced stage of dynamical evolution, although the range of values sampled by the parameters decreases for increasing binary fraction, due to the milder contraction of the core. This illustrates the complexity of univocally deriving the internal dynamical stage of the cluster if

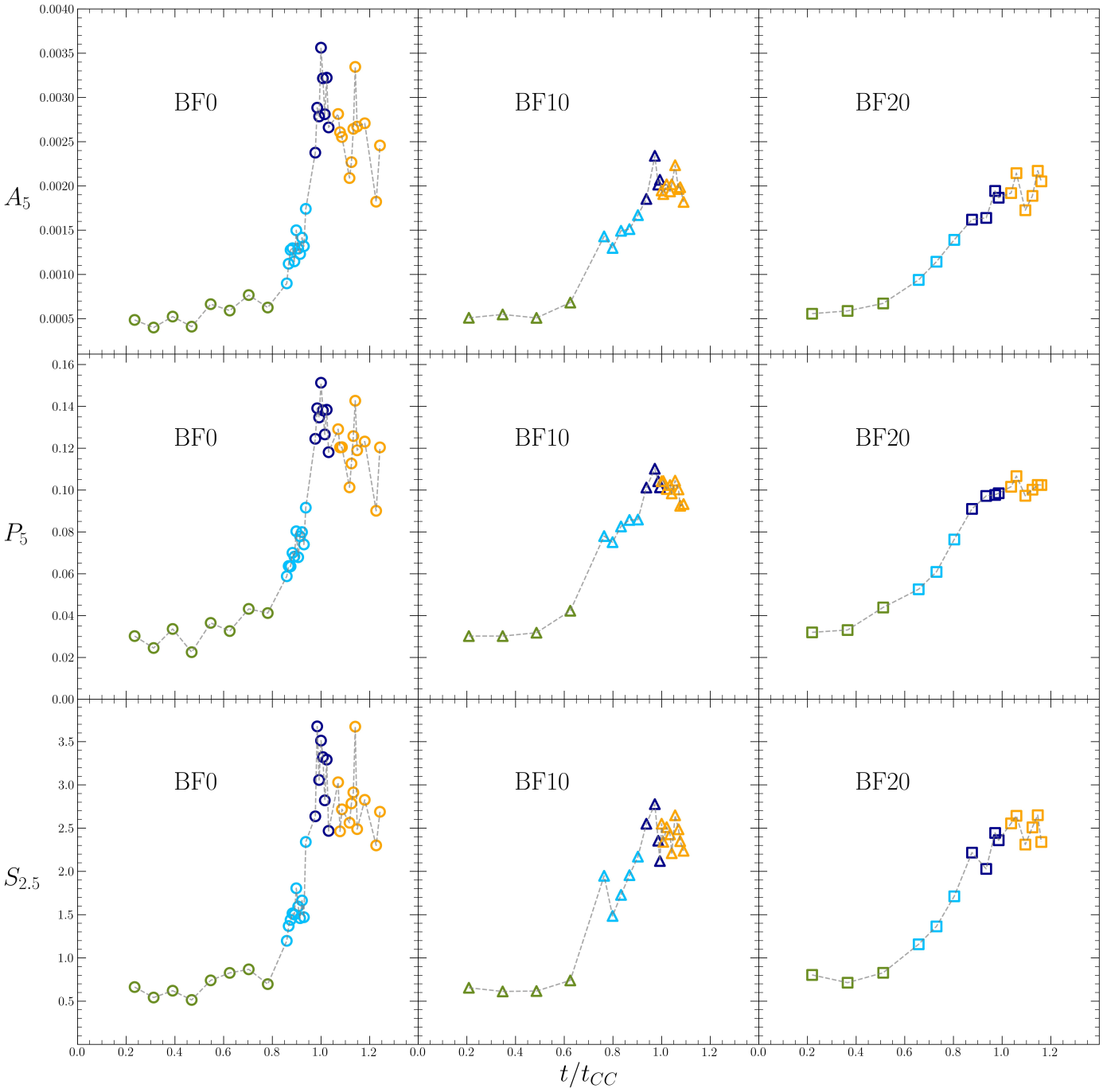

Figure 3.4: Time evolution of the A_5, P_5 and $S_{2.5}$ parameters (top, middle, and bottom panels, respectively) in the BF0, BF10, and BF20 simulations (left, central, and right panels, respectively). Time is normalised to the CC time of the corresponding simulation. The color code is the same as in Fig. 2.1.

the primordial binary fraction is unknown. Nevertheless, these diagrams also show that some useful information can still be obtained. In fact, irrespective of the binary fraction, the bottom-left corner of these plots is exclusively populated by dynamically young systems (green symbols), and the largest values found for the BF20 run correspond to quite evolved systems also in the other cases. In addition, if in an observed cluster one measures values of A_5, P_5 and $S_{2.5}$ that fall in the top-right corner of these diagrams, a large binary content can be excluded, and the cluster is likely to be in a quite advanced stage of dynamical evolution.

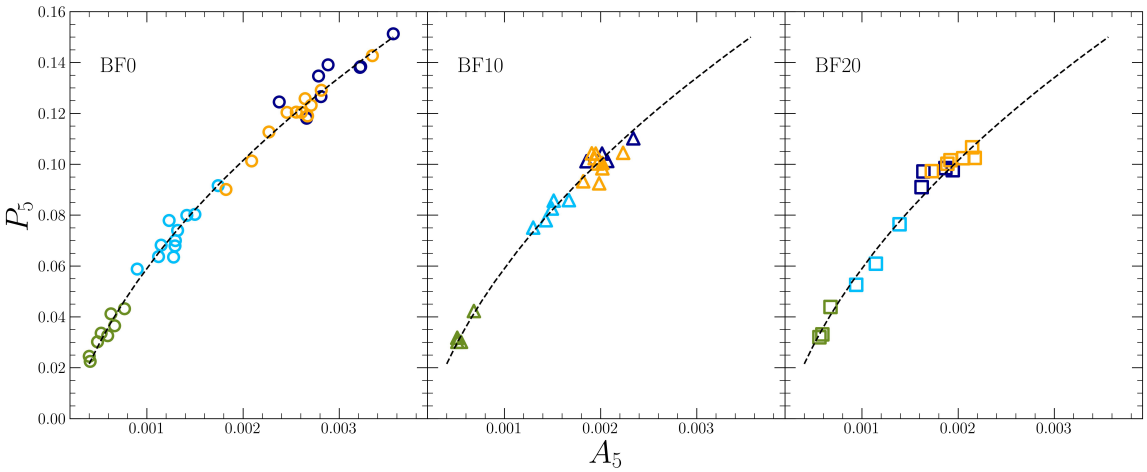

Figure 3.5: P_5 parameter plotted against A_5 for the BF0, BF10, and BF20 simulations (left, central, and right panels, respectively). The color code is the same as in all previous figures. The black dashed lines are the polynomial fit to the distribution obtained in the BF0 run, reported for reference also in the central and right panels.

[htb]

3.4. Zooming on the deviations from King models

By definition, the nCRD traces the projected radial distribution of stars with respect to the cluster center. Thus, it strictly depends on the projected density distribution of the system. In turn, the latter is commonly described through the King model family, which provides very good fits for clusters in early dynamical stages, while show significant discrepancies in the central regions for dynamically evolved systems (see Section 2.2 and, e.g., Figure 4 in Chapter 2). We therefore built the nCRDs by directly integrating the King model density profile for different values of the concentration parameter c between $\sim$ 1 and 2.5, and we used these functions to measure the three dynamical indicators defined above. The results obtained for the A_5 parameter are shown in Figure 3.8 as empty black circles. The colored

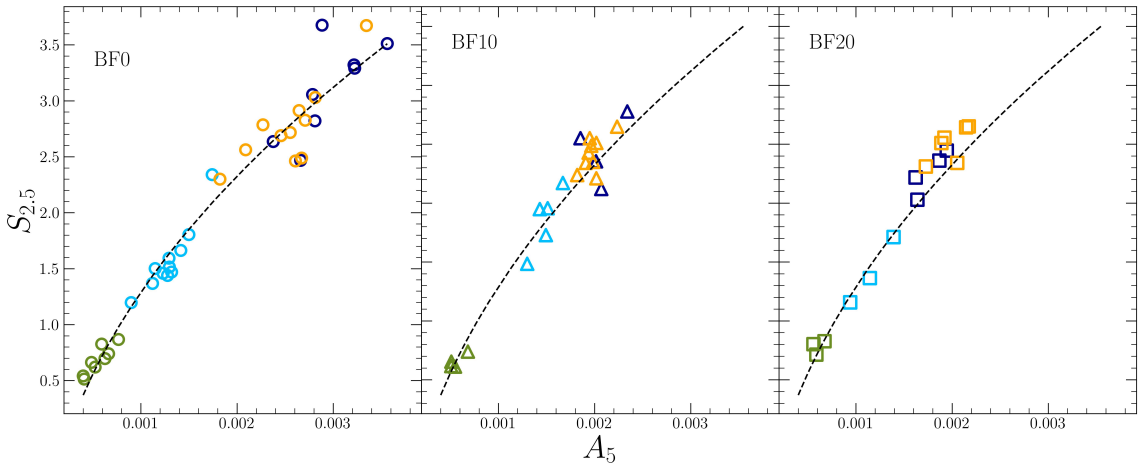

Figure 3.6: As in Fig. 3.5, but for the $S_{2.5}$ parameter plotted against A_5. trim=0 0 0 0

symbols in the figure correspond to the values determined from the actual nCRDs of the simulations, built as described in Section 3.3.2, plotted as a function of the concentration parameter of the King models that best-fit the "observed" density profiles for each extracted snapshot. The bottom panels show the relative difference between the parameter obtained from the actual nCRD and those obtained from the King model integration: $\epsilon = (A_5 - A_5^{\rm King})/A_5^{\rm King}$. This figure shows that, as expected from the gradual increase in concentration of the system, the values of both A_5 and c increase from early (green colors), to intermediate (cyan), to evolved dynamical stages (blue and yellow). In addition, in the very early phases of dynamical evolution (green symbols), the density distribution is properly reproduced by the King family, and the A_5 parameter measured from the actual nCRDs is essentially the same as that obtained from the King models, irrespective of the primordial binary fraction. Then, from the pre-CC stage (cyan) onwards, the two measures of A_5 start to differ: in fact, the growth of the stellar density toward the center of the system makes the nCRDs increasingly steeper, and the value of A_5 starts to systematically and growingly exceed the corresponding value of $A_5^{\rm King}$. Hence, the A_5 parameter can be used as a sort of magnifier to pinpoint clusters with density profile deviating from the King model distribution, well before the contraction of the system produces a measurable central cusp in the observed profile.

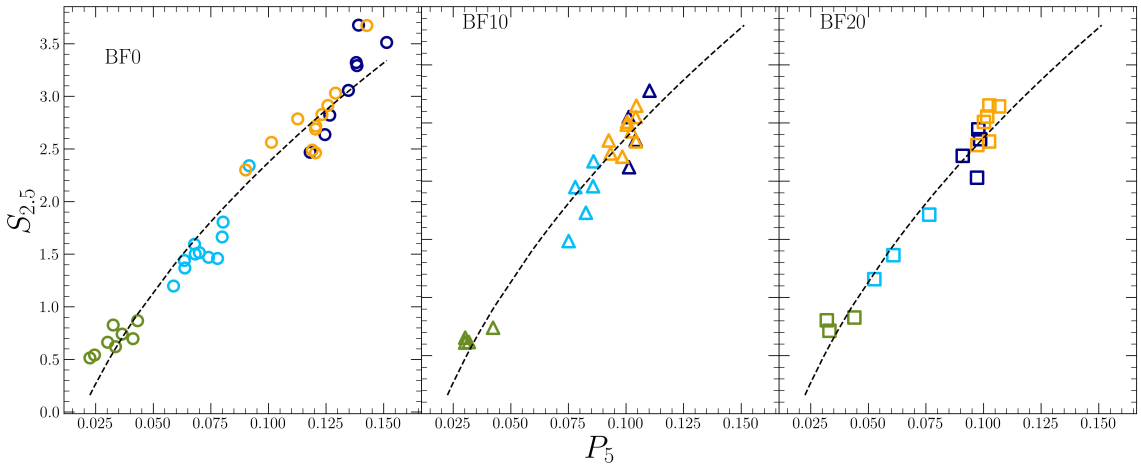

Figure 3.7: As in Fig. 3.5, but for the $S_{2.5}$ parameter plotted against P_5.

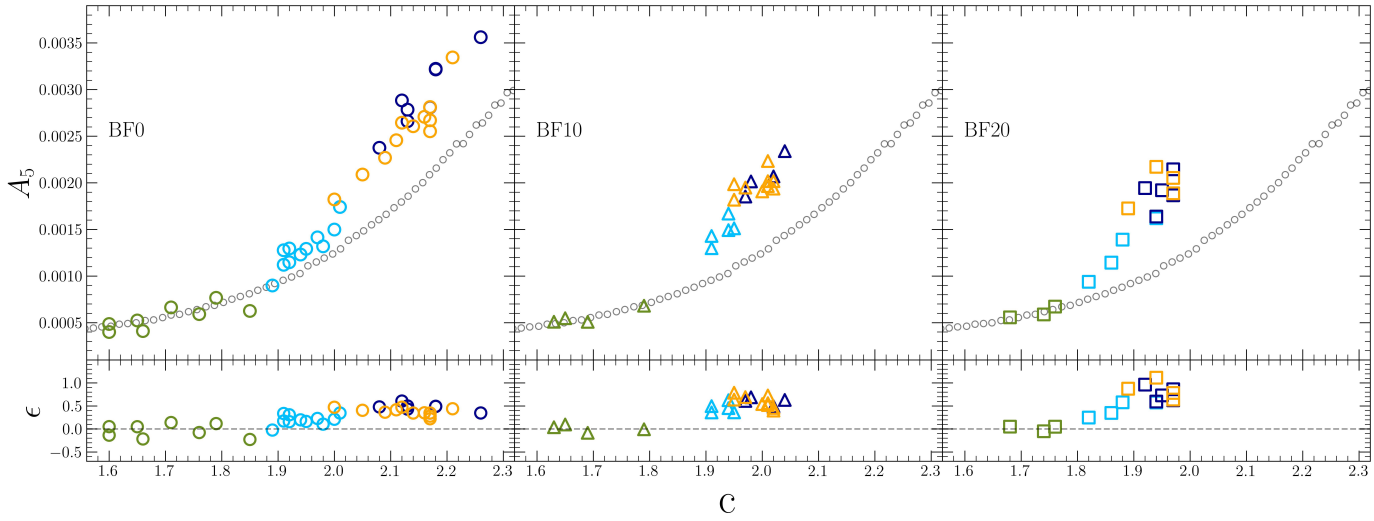

Figure 3.8: Values of A_5 measured from the direct integration of the King model density profile for different values of the concentration parameter c (black empty circles), compared to those obtained from the nCRDs of the extracted snapshots (colored symbols, the same as in the top row of in Fig. 3.4) plotted against the concentration parameter of the King models that best-fit the density profile of each simulation. The left, central and right panels refer to the BF0, BF10, and BF20 simulations, respectively. The bottom panels show the relative difference between the two measurements: $\epsilon = (A_5 - A_5^{\rm King})/A_5^{\rm King}$

3.5. Effect of dark remnants on the nCRD dynamical indicators

While the previous sections focused on the effects of primordial binary systems, here we discuss how the nCRD dynamical indicators are affected by the presence of dark remnants. To this end, we consider the DRr and DRe simulations where a reduced kick velocity for black holes is adopted according to the fallback prescription of Belczynski et al. (2002), thus significantly enhancing the fraction of BHs retained within the system potential well, with respect to the BF0, BF10, and BF20 simulations. The time evolution of the number of black holes for the DRr and DRe runs is shown in Figure 3.9. As apparent, the rate of ejection of black holes in the DRe simulation (green circles) is much higher than that of the DRr simulation (indigo circles).

Figure 3.10 shows the time evolution of 1% Lagrangian radius of the DRr and DRe runs (on left and right panel respectively), with the extracted time snapshots marked by vertical dashed lines. At odds with the simulations discussed so far (compare to Fig. 2.1), the evolution of $r_{1\%}$ in the DRr simulation shows an extended expansion phase lasting up to about 10 Gyr driven by the retained black holes. Such a long expansion phase is then followed by a gradual decrease of $r_{1\%}$, where two-body relaxation drives the cluster contraction. The system, however, never reaches the most advanced dynamical phases and the CC stage in a Hubble time. In the case of the DRe simulation (right panel of Fig 3.9), due to its higher rate of ejection, most of the black holes are ejected by $\sim$ 5 Gyr and, after that time, the cluster's inner regions contract until the collapse is halted by primordial binaries at about 13.7 Gyr; the post-CC stages are similar to the BF10 and BF20 models.

By adopting the same procedures described in Section 3.3.1, we computed the nCRDs for all the extracted snapshots of DRr and DRe. The nCRDs for DRr are shown in indigo lines and those of DRe in green lines on the left and right panels of Figure 3.11 respectively. In the same figure, they are compared to the nCRDs obtained from the BF10 run (pink lines). At all evolutionary times, the nCRDs corresponding to the DRr run are all clumped (hence, they essentially show the same morphology) and have much shallower slopes than the BF10 run, implying a much smaller percentage of stars also in the innermost regions, where the three dynamical indicators are defined. This is fully confirmed by the time dependence of A_5, P_5, and $S_{2.5}$ shown in Figure 3.12, where the values obtained from the DRr run (indigo diamonds) are compared to those measured in the BF10 and BF0 simulations (pink triangles and gold squares, respectively): the former always show much smaller values than the others, and they are almost independent of time, consistently with the lack of a significant structural evolution displayed by $r_{1\%}$ in Fig. 3.10. The shapes of the nCRDs of DRe evolve from having shallower slopes in the early snapshots (which are still affected by the expansion induced by the retained BHs), to having shapes indistinguishable from those of BF10 (at $t >= 7$ Gyr, when essentially all the

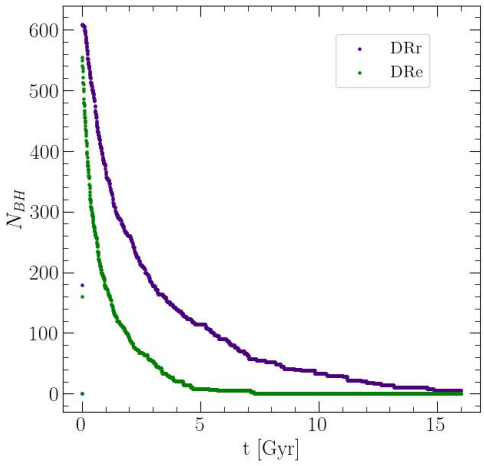

Figure 3.9: Time evolution of number of black holes in the two simulations with a large retention fraction of dark remnants: DRr (indigo circles) and DRe (green circles).

BHs have been ejected and the evolution becomes similar to that of BF10). Indeed, the time dependence of the dynamical indicators shown in Figure 3.12 for the DRe run (green circles) clearly starts from a low value similar to DRr run and follows an increasing trend like in BF0 and BF10 runs. In particular they are closer to the values of BF10 run. This reflects the fact that even though the cluster starts with a significant number of dark remnants (hence the nCRDs are shallow and the dynamical indicators have low values, like in DRr run), as the cluster looses all the black holes it undergoes standard dynamical evolution and the three dynamical indicators follow the trend of BF10 simulation which has no dark remnants.

3.6. Discussion and summary

In this chapter we have investigated the effects of different primordial binary fractions and dark remnant contents on the value of three parameters specifically defined by Chapter 2 to quantify the dynamical evolution of the structural properties of star clusters. The (expected) impact of the fraction of binaries and dark remnants on the dynamical evolution of the system translates in a corresponding effect on the time dependence of the three parameters.

In the DRr run (where the rate of BH ejection is very low), the expansion effect due to the retained black hole system dominates most of the cluster's dynamical evolution. As a consequence, no significant contraction of the cluster occurs (see left panel of Fig. 3.10), and the values of the three parameters remain essentially constant with time and always much smaller than those measured in all the other simulations (see Fig. 3.12), where the number of BHs is below a few units either from the beginning (BF0, BF10, and BF20 runs), or for most of the cluster life

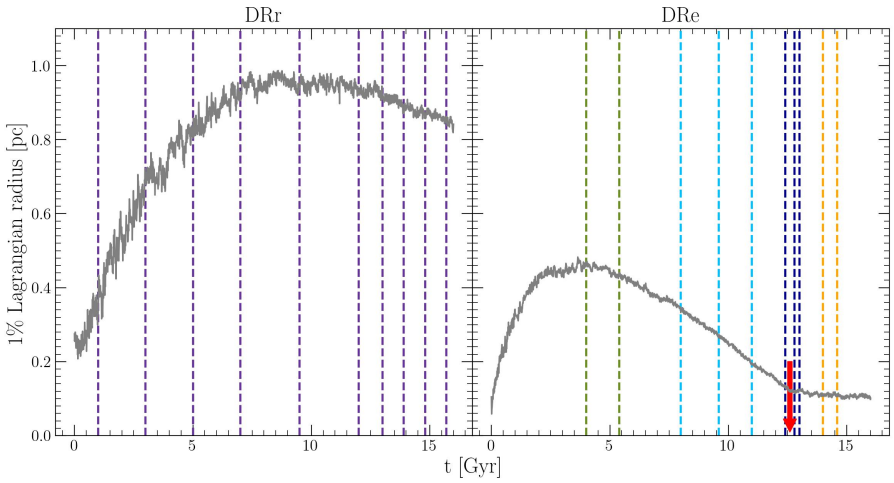

Figure 3.10: Time evolution of 1% Lagrangian radii in the two simulations with large retention fraction of dark remnants, DRr and DRe runs on left and right panels respectively. The vertical dashed lines in indigo color mark the ten time snapshots extracted from the DRr simulation and the vertical dashed lines with standard color code used in previous figures are the ten time snapshots extracted from DRe simulation.

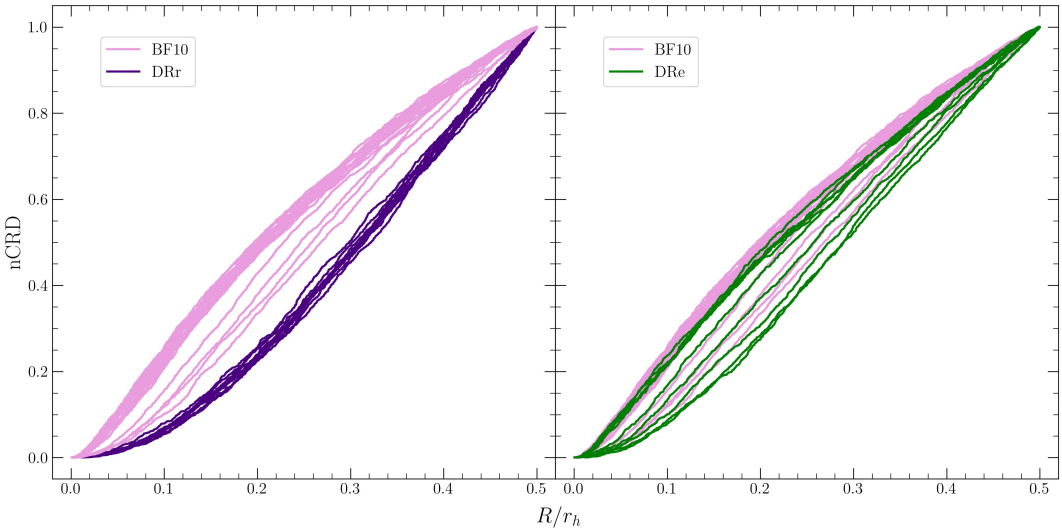

Figure 3.11: Normalised cumulative radial distributions for all the snapshots extracted from the DRr (indigo lines) and DRe (green lines) simulations on the left and the right panels respectively. They are compared to those obtained for the BF10 run (pink lines, the same as in the right panel of Fig. 3.3).

(DRe simulation). Hence, although in this case the nCRD parameters cannot help understanding the dynamical age of the cluster (also because it does not go across

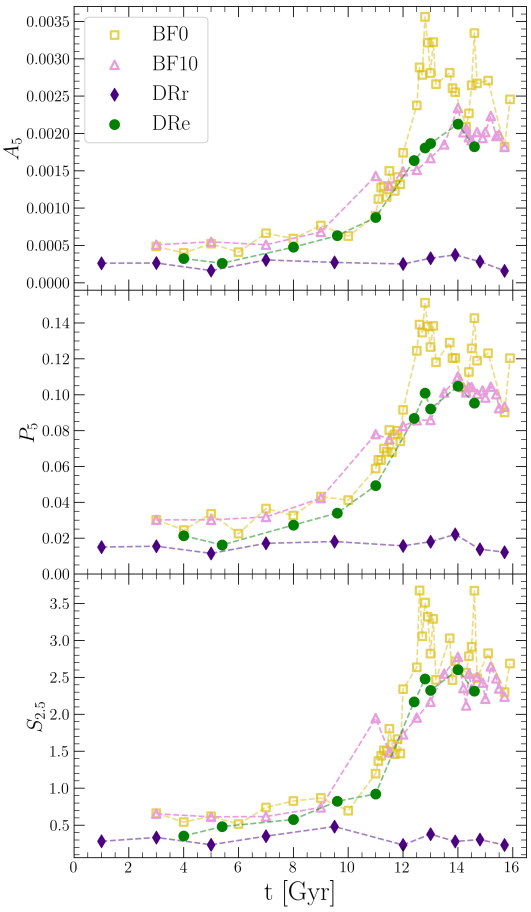

Figure 3.12: Time evolution of the A_5, P_5 and $S_{2.5}$ parameters for the DRr run (indigo diamonds) and the DRe run (green circles), compared to those measured in the BF10 and BF0 simulations (pink triangles and gold squares, respectively).

well-distinct dynamical phases), measuring such low values might be used as an indication that the system still includes a significant number of stellar-mass black holes (or, at least, that it retained a significant number of dark remnants for a large fraction of its life). The DRe run, which started with the same number of BHs as in the DRr simulation, but then ejected almost all of them during the initial ~ 5 Gyr of its evolution, essentially behaves as the models with no dark remnant retention. This implies that, while the three nCRD parameters cannot help disentangling among DRe and these latter cases, they allow us to determine the dynamical stage of star clusters with a high rate of BH ejection, even if they initially retained a large amount of these compact objects.

In the three models with different primordial binary fractions and no BH retention, the general trend is that the values of the three parameters gradually increase with time, and trace the internal dynamical evolution of the cluster. The time variations of A_5, P_5, and $S_{2.5}$ are most pronounced in the BF0 simulation, then become less

marked in systems including primordial binary stars reflecting the milder contraction of these clusters. Strictly speaking, this implies that to properly infer the dynamical age of a cluster, one needs not only to measure the values of these parameters, but also know the binary fraction of the system. Nevertheless, some general conclusions could be drawn even if this information is not available. In fact, Figs. 3.4−3.7 show that low values of the three parameters ($A_5 \lesssim 0.0006$, $P_5 \lesssim 0.04$, and $S_{2.5} \lesssim 0.08$) indicate young dynamical ages, irrespective of the binary content of the system. In addition, large values of the three parameters (as $A_5 \gtrsim 0.0023$, $P_5 \gtrsim 0.11$, and $S_{2.5} \gtrsim 2.7$) would univocally indicate a cluster in an advanced stage of dynamical evolution with no or very little primordial binaries. Indeed, the top-right corner of these diagrams is always empty in the BF10 and BF20 simulations, and this can be used as an indirect evidence against a large initial binary fraction in the system under analysis. Also the comparison between the values of A_5 measured from the nCRD and those expected from the King model distribution (Fig. 3.8) shows that this parameter is able to trace the progressive deviations from the King model expectations that occur during the late stages of dynamical evolution. Hence, in both theoretical and observational studies, A_5 can be used as a sort of magnifier to identify a dynamically old system well before its contraction produces a measurable central cusp in the density profile.

The analysis presented in this chapter confirms that the three nCRD parameters introduced in Chapter 2 are very useful tools to investigate the dynamical stage of stellar systems, even in the cases of a non-zero primordial binary fraction and in the case of clusters with a high rate of BH ejection. In this investigation the analyzed simulations follow the evolution of a given system over the cosmic time, while the GCs in our galaxy all have essentially the same, old age ($\sim$ 12- 13 Gyr), but are observed in different stages of their internal dynamical evolution. The forthcoming chapter will be thus devoted to the analysis of the nCRD parameters in a sample of simulated clusters generated from a broad range of different initial conditions (hence, subject to different rates of internal dynamical evolution), but all considered at the same chronological age of $\sim$ 13 Gyr.

Chapter 4

Survey of simulations at 13 Gyr

Mainly based on:
Bhat et al. (2023), in preparation

In the previous chapters, we have followed the dynamical evolution of simulated clusters over the course of their life time, analyzing the impact of different initial conditions individually. In this chapter, in order to investigate clusters in a diverse range of dynamical evolutionary stages but with the same chronological age, we will analyze a sample of Monte Carlo simulated systems with an age of 13 Gyr, run from a variety of initial conditions and hosting both primordial binary populations and DRs. This sample of simulations are representative of the Galactic population of GCs, which are observed today in different stages of dynamical evolution, after $\sim$ 13 Gyr since their formation. The chapter is organized as follows. In Section 4.1, we describe the initial conditions of all the the Monte Carlo simulations in the survey and the methodology adopted in the following analysis. In Section 4.2, we show the comparison between the structural parameters of survey simulations and those observed in the Galactic GC population (from the Harris catalog). Section 4.3.1 presents the nCRDs of survey simulations and recalls the definition of the three dynamical parameters. Section 4.3.2 describes the reference samples and reference models adopted for the analysis of the nCRD parameters, and Section 4.3.3 elaborates on the impact of the initial conditions of the simulations on the nCRD parameters. Finally, Section 4.3.4 discusses the ability of nCRD parameters to distinguish the clusters on the basis of their dynamical evolutionary stage. The summary and conclusion of the work are provided in Section 4.4.

4.1. Methods and Initial Conditions

For the purpose to trace the range of structural parameters observed in GGCs today, we ran 54 Monte Carlo simulations using the MOCCA code (Hypki & Giersz, 2013;

Giersz et al., 2013) starting with different initial conditions such as initial number of stars (N), galactocentric distance (R_g), ratio of half-mass radius to tidal radius (r_h/r_t), and a parameter (k) indicating a standard or a reduced kick velocity for stellar mass BHs (see below). We analyze all the simulations at 13 Gyr to access their dynamical stage at this time. MOCCA code takes into account the impact of binary and star evolution with SSE and BSE codes (Hurley et al., 2000, 2002), the effects of two-body relaxation, and a tidal truncation. It offers the information of position, velocity, mass, and B- and V-band magnitudes for each star at every time in the cluster evolutionary history. Three sets of simulations were run with initial number of stars N = 500k, 750k, and 1M, respectively. The stellar masses range between 0.1 and $100 M_{\odot}$ following a Kroupa (1995, 2003) initial mass function. The stars are initially distributed following a King model (King, 1966) with dimensionless central potential $W_0 = 7$. For half of the considered simulations (from here on these will be referred to as k=0 models), supernovae (SNe) natal kick velocities for BHs are assigned according to a Maxwellian distribution, with velocity dispersion of 265 kms^{-1} (Hobbs et al., 2005). For the other half (hereafter, k=1 models) the BH natal kicks were reduced adopting the mass fallback procedure described by Belczynski et al. (2002). Furthermore, the clusters were initially placed at different galactocentric distances: R_g = 2 kpc, 4 kpc and 6 kpc. Additionally, they are tidally underfilling to varying degrees characterized by the value of r_h/r_t, which are chosen to be 0.025, 0.05, and 0.1, and with the tidal radius of simulations with N=500K, 750K, 1M being fixed to $\sim$ 40 pc, $\sim$ 46 pc, and $\sim$ 50 pc, respectively. All the simulations start with 10% primordial binary fraction. To identify each of these simulation, we introduce a naming convention based on their initial conditions. For instance, N500_k0_Rg2_rp0.1 represents the simulation with initial conditions, N=500K, k=0, R_g = 2 and r_h/r_t=0.1. See 4.1 for the list of initial conditions used for all the simulation runs.

Table 4.1: Initial conditions of the simulations

N:	500k	750k	1M
k:	0	1	
R_g(kpc):	2	4	6
r_h/r_t:	0.025	0.05	0.1

Values of number of stars (N), BH kick velocity parameter (k), galactocentric distance (R_g), ratio of half-mass radius to tidal radius (r_h/r_t) adopted as initial conditions in the 54 Monte Carlo simulations analyzed in this investigation.

Figures 4.1−4.6 show the time evolution of 1% Lagrangian radius ($r_{1\%}$, i.e., the radius including 1% of the total cluster mass) of all the 54 simulations with initial conditions as listed in Table 4.1. The effect of different initial conditions is well

demonstrated by the temporal evolution of $r_{1\%}$. Only 46 of these simulated clusters survive until 13 Gyr, while the other 8 clusters get disrupted and they are marked by 'X' in the above mentioned figures. Among the surviving simulations, in only 6 cases the initial expansion driven by heavy mass loss from young, massive stars is followed by a phase where two-body relaxation becomes dominant, making $r_{1\%}$ to contract progressively and leading to the CC and post-CC phases: these are simulations N500_k0_Rg2_rp0.05, N500_k0_Rg2_rp0.1, N500_k0_Rg4_rp0.025, N500_k0_Rg6_rp0.025, N500_k1_Rg25_rp0.025, N750_k0_Rg4_rp0.025). In 3 other runs, namely in N500_k0_Rg2_rp0.025, N750_k0_Rg2_rp0.025, N1_k0_Rg2_rp0.025, after the initial phase of expansion due to the stellar evolution, the time evolution of $r_{1\%}$ shows a peculiar behavior, due to the presence of an IMBH of mass, M> $300M_{\odot}$. The remaining simulations either undergo contraction due to two-body relaxation and reach CC beyond 13 Gyr (e.g., N750_k0_Rg2_rp0.05), or show an extended expansion phase for a significant fraction of their lifetime (e.g., N500_k1_Rg6_rp0.025,N500_k1_Rg4_rp0.05), while 2 of them (N750_k1_Rg6_rp0.1,N1_k1_Rg6_rp0.1) show a unusual behaviour in $r_{1\%}$ due to the presence of large number of stellar mass BHs. Altogether, the survey shows a large variety of dynamical evolutionary histories, which is well convenient for the current analysis.

With the aim to explore the impact of different initial conditions on the long term dynamics of star clusters and their effects on the behavior of the nCRD parameters discussed in the previous chapters, here we apply the same methodology to the 13 Gyr snapshots extracted from each simulation (which are marked by the vertical red line in Figures 4.1-4.6). The underlying idea is that the 46 snapshots taken from this survey are representative of the population of GGCs, which are in different dynamical stages due to their different initial and environmental conditions. As in the previous studies, the analysis of the 46 snapshots is done from the point of view of an observer. Thus, standard procedures and approximations adopted in observational works have been applied: in each snapshot,the simulated cluster is projected onto a 2D plane, and a distance of 10 kpc from the observer has been assumed to transform the distances from the centre of the system from parsecs to arcseconds. Besides, for binary systems, magnitudes are computed by summing up the luminosities of both components analogous to treatment of "stellar blends" in the observed GGCs where they can't be resolved.

4.2. Comparison of survey simulations with the Harris catalog

In this section, we compare the structural parameters of the 13 Gyr snapshots of simulation survey with those of the GGC population from the Harris (1996) catalog, to verify whether the artificial systems resemble the real ones.

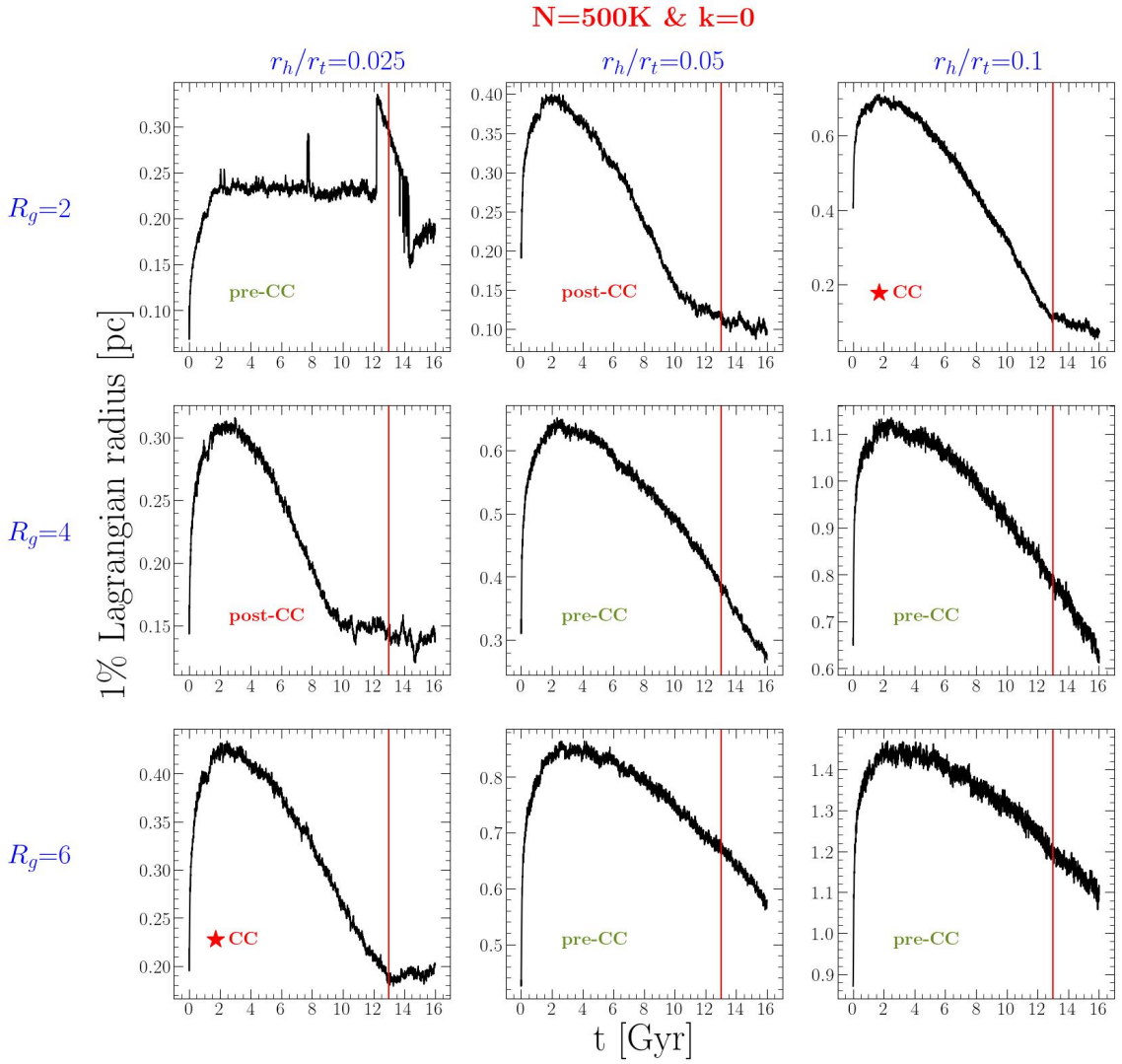

Figure 4.1: Time evolution of 1% Lagrangian radius for the simulation runs with initial conditions N=500 K, k= 0 and different values of R_g=2, 4, 6 and r_h/r_t=0.025, 0.05, 0.1 (see labels). The red vertical line at 13 Gyr marks the time snapshot the simulation used for analysis. The dynamical evolutionary stage of the simulated cluster at 13 Gyr, as shown traced by the evolution of 1% Lagrangian radius, is labelled in each panel as: “pre-CC", “CC" and “post-CC".

To determine the structural parameters, we construct the number density profile of each snapshot and search for its best-fit King model using the same methods adopted in observational works and outlined in Section 2.2. We find that the King profile fits quite well the density profiles of most (80%) of the snapshots of survey, with the exclusion of the ones that are close to and beyond CC, when a density cusp develops in the center. These density cusp are shallow compared to the case of the BF0 simulation presented in Chapter 2, consistent with the fact that these

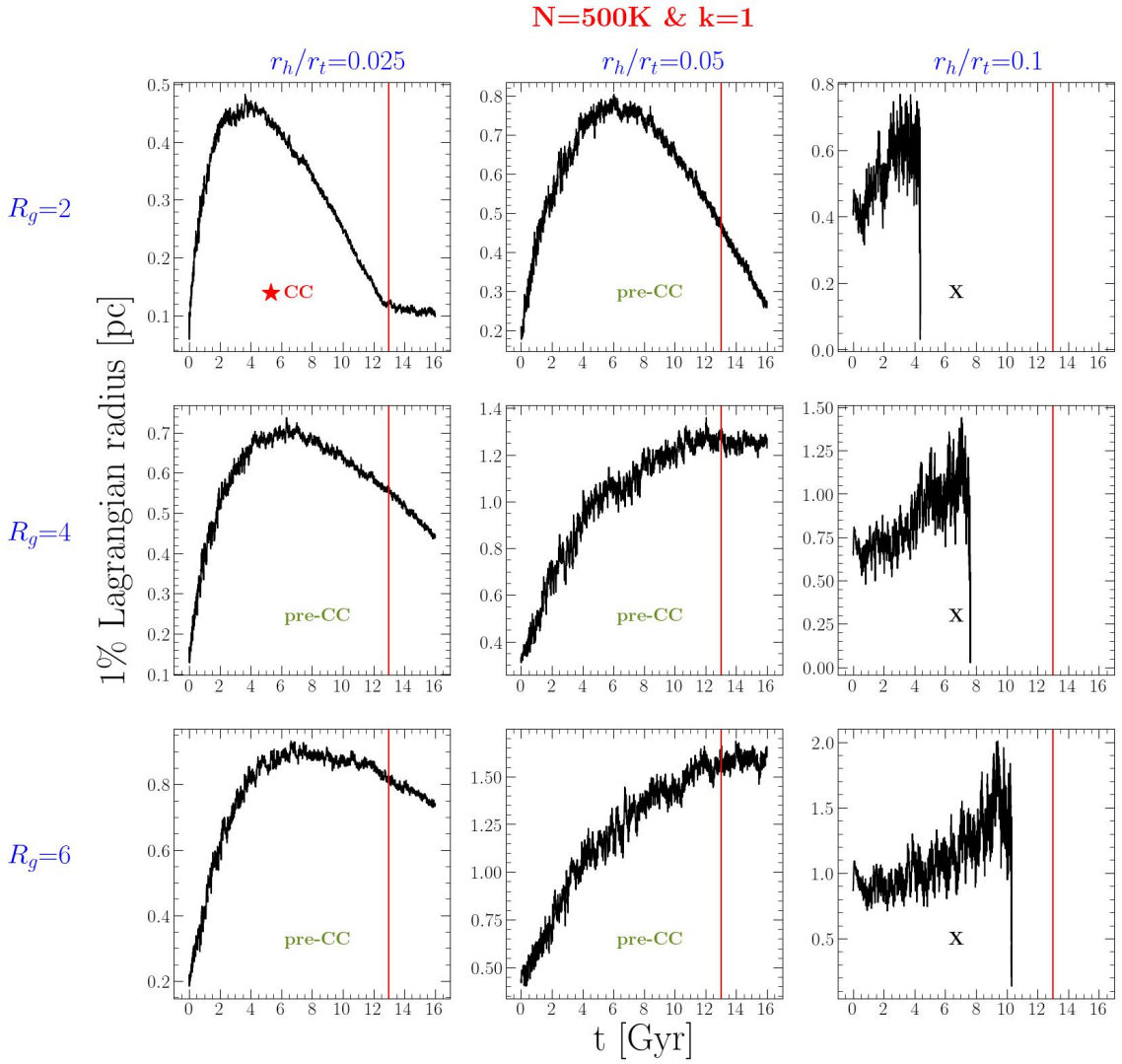

Figure 4.2: Time evolution of 1% Lagrangian radius for the simulation runs with initial conditions N=500 K, k= 1 and the adopted values of R_g and r_h/r_t (see labels).

runs started with 10% binary fraction and DRs. As discussed above, for the sake of homogeneity and reproducibility, and to avoid arbitrariness, the cusps are not excluded from the King fits.

In Figure.4.7, we have plotted core radius against half-light radius, and concentration against core radius for the survey simulations (red circles) and for GGCs from the Harris catalog (grey circles) in left and right panels respectively. It is quite evident that the survey simulations effectively sample the parameter space populated by GGCs, although some more simulations covering the low concentration, high R_c and high r_{hl} regimes would help improving the comparison. Although, the simulations considered here start from the high central potential (proportional to concentration), W0= 7 even after 13 Gyrs of evolution, they don't populate the low concentration

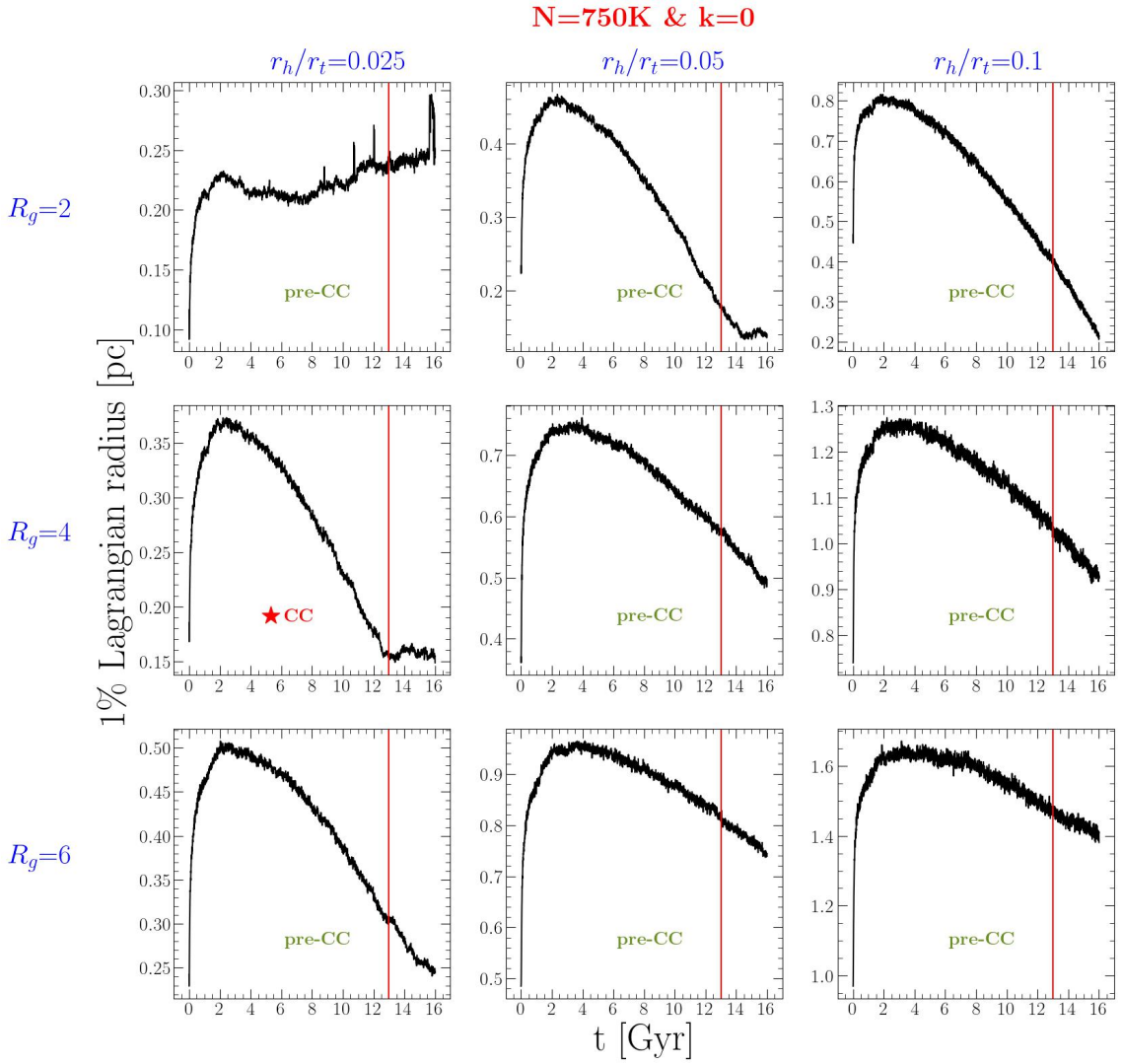

Figure 4.3: Time evolution of 1% Lagrangian radius for the simulation runs with initial conditions N=750 K, k= 0 and the adopted values of R_g and r_h/r_t (see labels).

regime. However, simulations starting with W_0 values smaller than considered here ($W_0 < 5$) could potentially populate this regime, for the scope of our analysis, the survey simulations at 13 Gyr can be considered as representative of the GGC population.

4.3. nCRD Parameters

In this section we apply to the simulation snapshots the same analysis procedures presented in Chapter 2 for the determination of the three nCRD parameters. Thereby, we evaluate to what extent the dynamical indicators describe the

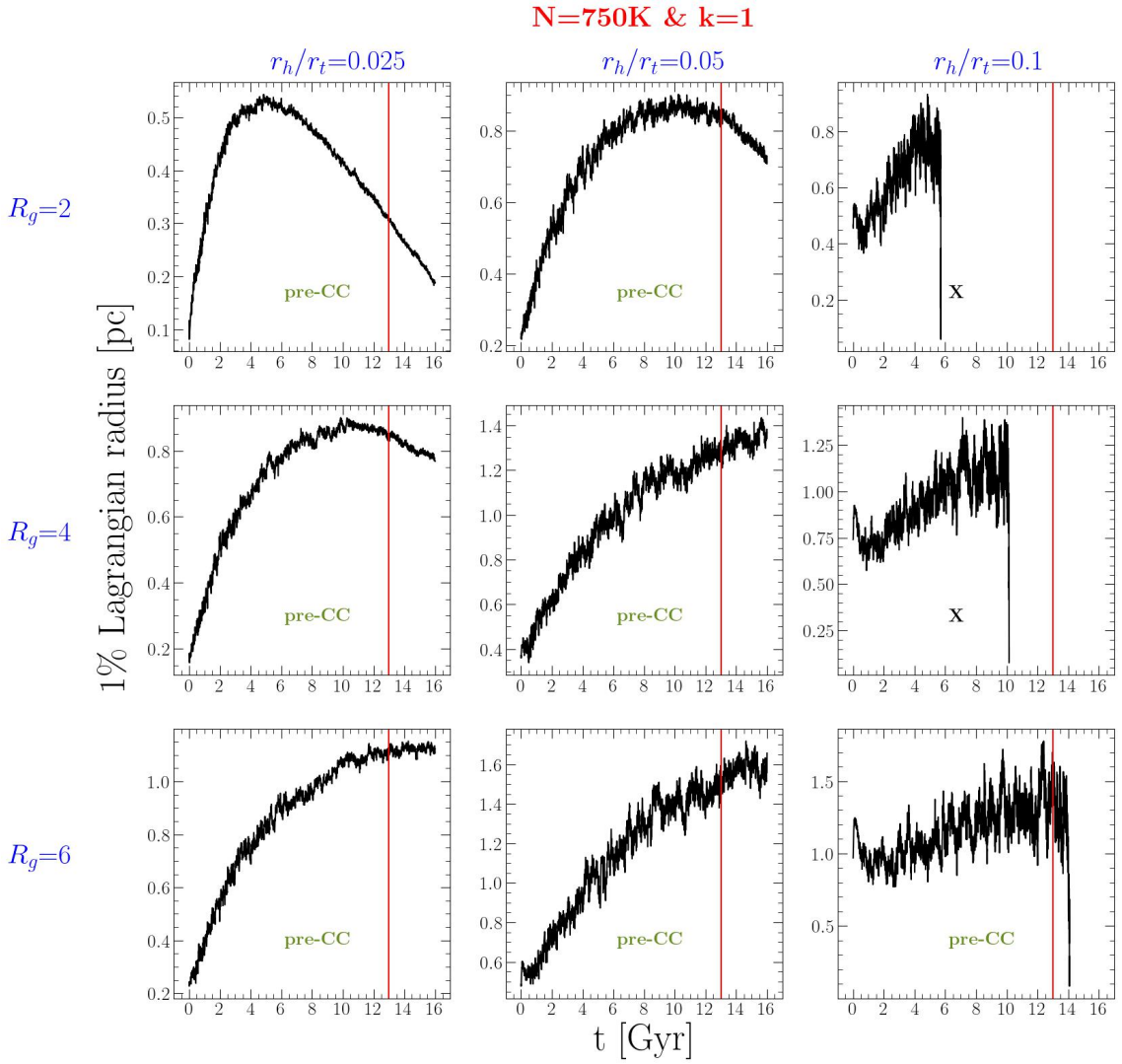

Figure 4.4: Time evolution of 1% Lagrangian radius for the simulation runs with initial conditions N=750 K, k= 1 and the adopted values of R_g and r_h/r_t (see labels).

dynamical evolutionary stage attained by the simulated clusters, which started with different initial conditions and contents (DRs+ primordial binaries).

4.3.1 Construction of nCRD and nCRD parameters

For each extracted snapshot, to build the nCRD we selected all the stars brighter than $V_{cut} = V_{TO} + 0.5$ (with V_{TO} being the $V-$band magnitude of the main-sequence turn-off point), and located within a projected distance equal to 0.5 $\times r_h$ from the centre.

Figure 4.8 shows the nCRDs of all the analysed snapshots (left panel), and their zoom into the innermost region ($R < 0.1 r_h$). As well apparent, especially in the cen-

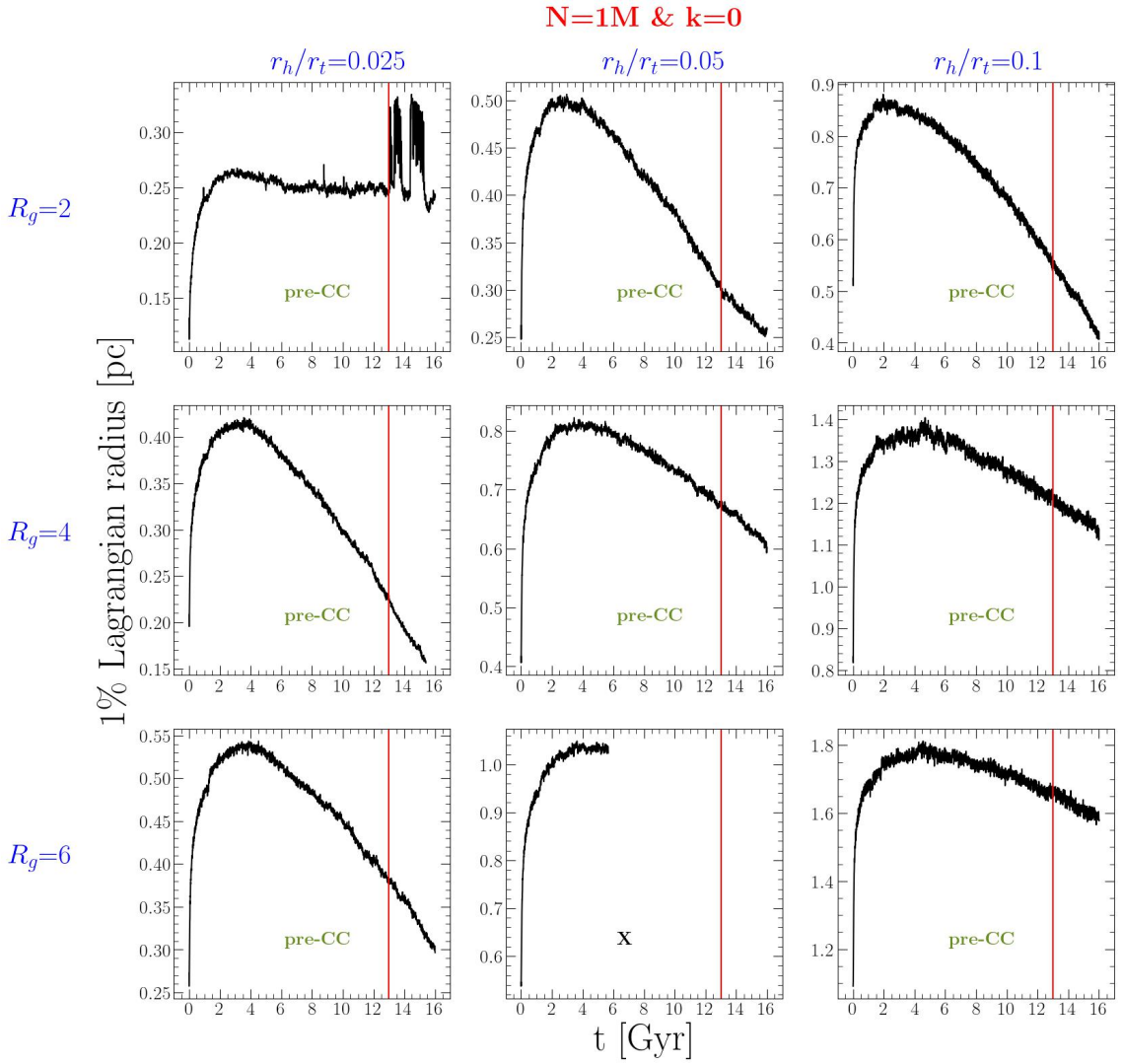

Figure 4.5: Time evolution of 1% Lagrangian radius for the simulation runs with initial conditions N=1 M, k= 0 and the adopted values of R_g and r_h/r_t (see labels).

ter, most of the nCRDs (corresponding to pre-CC systems: green lines) are clumped together and much shallower than those of the 6 CC or post-CC snapshots (red lines) as identified from the $r_{1\%}$ evolution shown in Figures 4.1−4.6. By construction, this implying a much smaller percentage of stars for fixed radial distance, especially in the innermost regions, suggesting that the initial conditions have played a role in keeping them dynamically young. Based on previous analyses, we expect that this behavior can be also due to the presence of stellar mass BHs at the center, which prevent the progressive segregation of cluster stars avoiding the successive dynamical evolutionary phases. It is also noteworthy that there are four snapshots classified as pre-CC (from here on called “dynamically young") that closely follow the nCRDs of dynamically evolved systems (see the four green lines superposed to the red lines

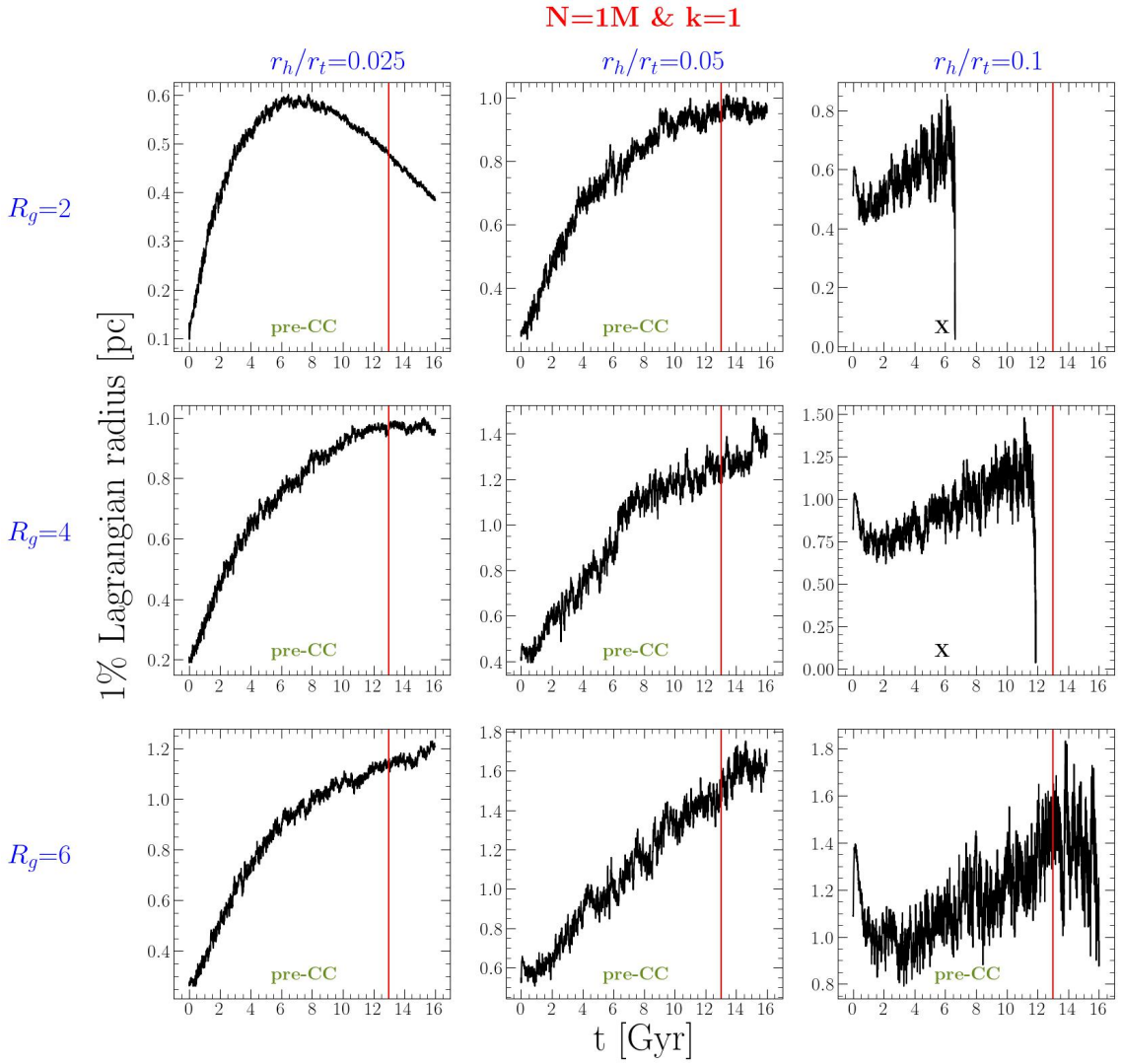

Figure 4.6: Time evolution of 1% Lagrangian radius for the simulation runs with initial conditions N=1 M, k= 1 and the adopted values of R_g and r_h/r_t (see labels).

in the figure). These correspond to simulations that, at 13 Gyr have not reached CC yet, but are indeed very close to it, while we classify as pre-CC clusters all the snapshots that, based on the time evolution of their 1% Lagrangian radius, lie before CC, irrespective of their closeness to it. This likely indicates that a dynamical classification based on a visual inspection of the time dependence of $r_{1\%}$ is not accurate enough, and further call for the need of more precise diagnostics of the dynamical a star cluster dynamical age.

The evidence that, based on their morphology, the analyzed nCRDs tend to separate in two different groups indicates that the three nCRD parameters defined in Section 3.3.2 can be used also in the present study, to quantify the morphological nCRD differences and use them as dynamical diagnostics of the considered 13 Gyr

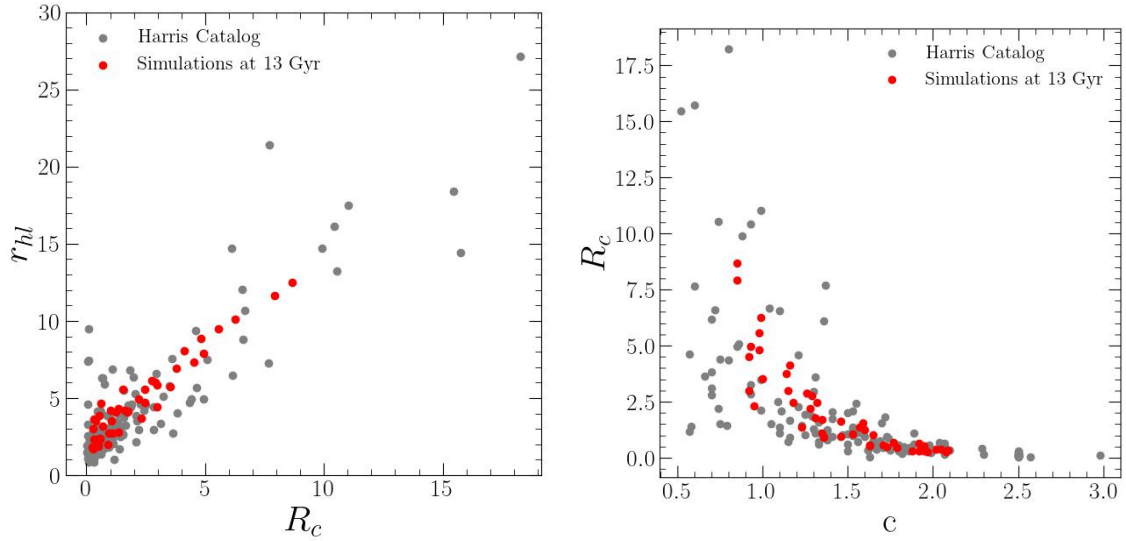

Figure 4.7: Half-light radius (r_{hl}) plotted against core radius (left panel), and core radius plotted against concentration parameter (right panel) for the 46 time simulation snapshots at 13 Gyr analyzed in this study (red circles), compared to those measured in the GGC population (from Harris 1996).

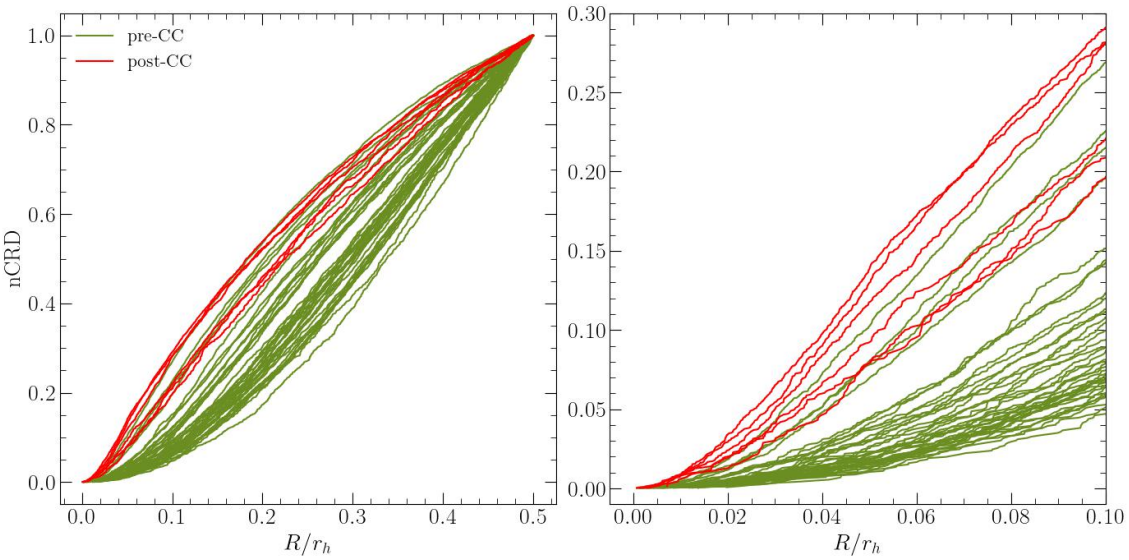

Figure 4.8: Left panel: Normalized cumulative radial distributions (nCRDs) of the stars brighter than $V = V_{TO} + 0.5$ and located within $0.5 \times r_h$ from the center for all the analysed snapshots. Right panel: zoom into the inner region of the nCRDs shown in the left panel. The color code is as follows: green for dynamically young (per-CC) snapshots and red for dynamically old (CC and post-CC) snapshots.

snapshots. For the reader's convenience, here we recall the definition of the three parameters:

- A_5 is the area subtended by each nCRD between the center and a projected distance equal to 5% r_h (hence, between $x = 0$ and $x = 0.05$, with $x = R/r_h$);
- P_5, is the value of the nCRD at 5% r_h ($x = 0.05$), which corresponds to the fraction of selected stars located within this distance from the centre;
- $S_{2.5}$ is the slope of the straight line tangent to the nCRD at 2.5% r_h (at $x = 0.025$). More specifically, it is the slope of the tangent to the third-order polynomial function that best-fits the nCRD (the fit being introduced to smooth out the noisy behavior of the nCRD itself).

Before computing the three parameters for the survey simulations, we introduce the reference models and simulation samples that are used for the comparison with previous findings and the proper interpretation of the results.

4.3.2 Reference models and samples

As discussed in Chapter 3, clusters of BF0, BF10, BF20 and DRr simulations that are evolving in different dynamical phases tend to occupy different regions in the plots that show one nCRD parameter against the other (see Figs. 3.5−3.7). We can therefore exploit their distribution in these diagrams to define boundaries aimed at differentiating star clusters in different dynamical phases. In Figures 4.9, 4.10, and 4.11 we plot the three parameters against each other superposing the values previously measured in the BF0 (circles), BF10 (triangles), BF20(squares) and DR (diamonds) simulations using the same color code as in Fig.2.1 for the different dynamical phases. As apparent, the snapshots that are in early dynamical stages and in pre-CC phases (green and cyan symbols, respectively) occupy the lower left part of the plots, together with all the snapshots of the DRr simulations (indigo diamonds) that, due to the large population of retained BHs, essentially show no dynamical evolution. Conversely, the snapshots in CC and post-CC phases occupy the upper right part of the plots. There is also an intermediate overlapping region where a few pre-CC, CC and post-CC snapshots are found to lie together. Based on this evidence, we drew a boundary region (green shaded) safely including only dynamically young snapshots (namely, all the DRr simulations, and the early and pre-CC snapshots of BF0, BF10 and BF20), and another region (red shaded) conservatively including only CC and post-CC snapshots from all the previous simulations. Specifically, boundary for dynamically young systems is set at $A_5 \leqslant 0.0015$, $P_5 \leqslant 0.085$, $S_{2.5} \leqslant 1.9$, while the boundary for CC and post-CC clusters corresponds to $A_5 \geqslant 0.0019$, $P_5 \geqslant 0.095$, $S_{2.5} \geqslant 2.4$. Of course, these boundaries are somehow arbitrary and not strictly rigid, but they are meant to serve as reference and guides for the interpretation of the results obtained from the survey simulations, checking their conformity with those discussed in the previous chapter.

As reference models for the survey simulations, we consider the King models, which are known to well describe the dynamical state of typical globular clusters. Following

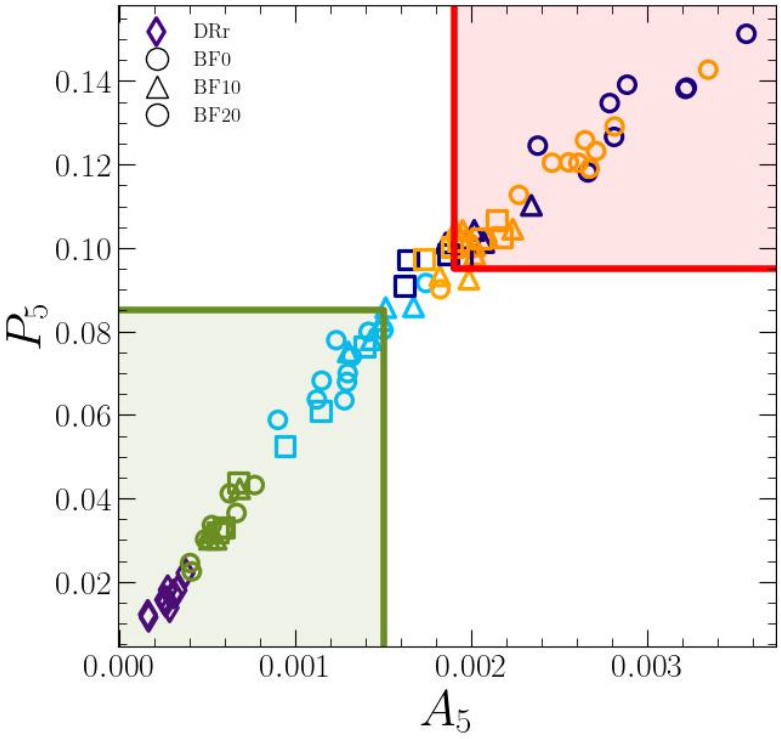

Figure 4.9: A_5 parameter plotted against P_5 parameter for the reference simulations BF0 (circles), BF10 (triangles), BF20 (squares) and DRr (diamonds) from Chapter 3. The color code of the symbols is as in the Fig.2.1. The boundary region including only dynamically young systems (DRd, pre-CC and post-CC snapshots of the reference simulations) is shaded in green. The one populated by only dynamically old systems in the reference simulations is shaded in red.

the analysis presented in Section 3.4, we computed the three dynamical parameters by directly integrating the density profile of a sequence of King models with concentration parameter c varying between 1 and 2.5, in steps of 0.05. They are plotted against each other (i.e., A_5 against P_5, A_5 against $S_{2.5}$, and P_5 against $S_{2.5}$) in left, central and right panels of Figure 4.12, respectively. These sequences will serve as reference models for the survey simulations, as the King family usually represents star clusters in a state of dynamical equilibrium, before CC: hence, deviations of the nCRD parameters from the King model sequence can provide insights into the dynamical state of the cluster.

4.3.3 nCRD parameters of survey simulations

In this section, equipped with boundaries to distinguish dynamically young from dynamically old clusters, and with the King model sequences to be used as reference models, we present and discuss the values of three nCRD parameters computed for the 13 Gyr snapshots of the survey simulations. Since these were performed for

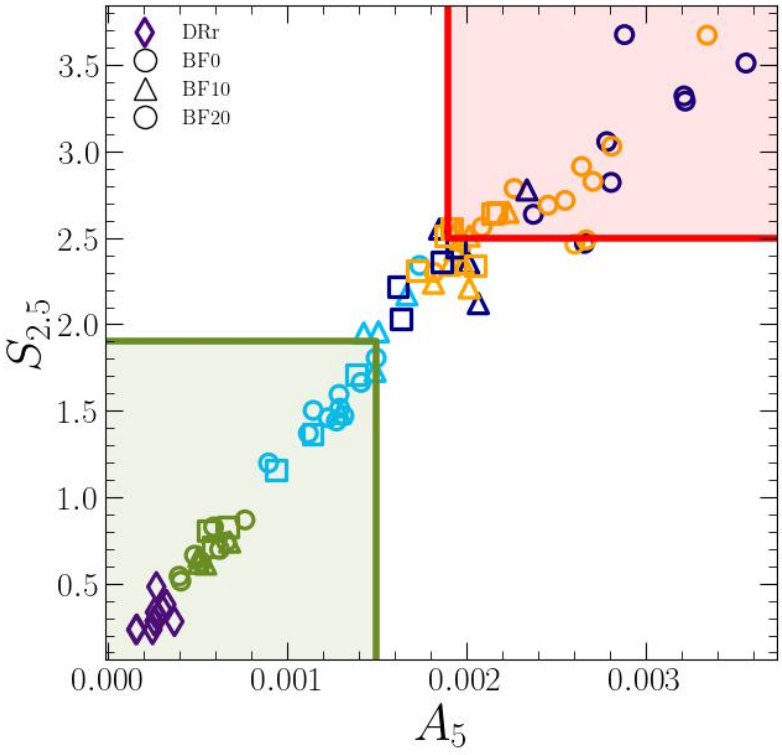

Figure 4.10: As in Fig. 4.9 but for A_5 plotted against $S_{2.5}$.

different initial conditions, as a first step we discuss the results obtained in terms of the adopted variations of each parameter, namely, the total number of stars N, the BH kick velocity prescription (k), the galactocentric distance (R_g), and the ratio between the half-mass and the tidal radii (r_h/r_t; see Table 4.1). It is however worth to keep in mind that it is challenging to disentangle the individual impact of initial conditions on the dynamics, as this is ultimately determined by the combination of them.

Impact of N

Figure 4.13 shows the three parameters plotted against each other with color coding for different values of the initial total number of particles: purple for N=500K, green for N=750K and orange for N=1M. For reference, we also plot the King model sequence (grey empty circles) and the adopted boundaries for dynamically young and dynamically old systems (olive green and red shaded region, respectively), as defined in Section 4.3.2 based on the results obtained from the simulations discusses in Chapters 2 and 3. The snapshots that include an IMBH ($M > 100 M_{\odot}$) at 13 Gyr are represented by squares in each color. As a general consideration, the majority of the snapshots fall in the dynamically young region (inside the green shaded boundary) and are distributed along the King sequence, while only a few (5 out of 46) are in the dynamically old region. This is well consistent with the shapes

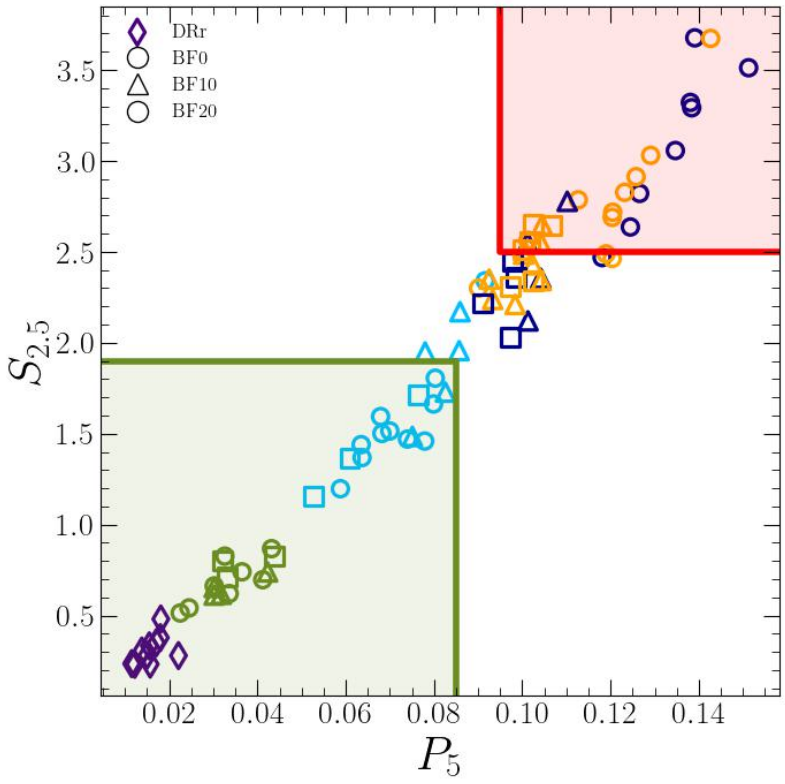

Figure 4.11: As in Fig. 4.9 but for P_5 plotted against $S_{2.5}$.

of the nCRDs discussed in Section 4.3.1, and will be further commented below. Here we note that the snapshots are distributed in these plots irrespective of their initial numbers of stars, with just a mild indication that the most massive systems (N=1M) tend to not reach the highest values of A_5, P_5 and $S_{2.5}$. This suggests that N doesn't have a significant impact on the clusters' dynamical history.

Impact of k

Figure 4.14 shows the three parameters plotted against each other with color coding for different k values (black for k=0, gold for k=1), along with the King model sequences (grey empty circles) and the boundaries for dynamically young and dynamically old regions (olive green and red shaded region, respectively). In this case, a clear dependence of the results on the adopted value of k is apparent. While the snapshots with k=0 (black circles) cover the entire range of values of the nCRD parameters, those with reduced BH kick velocity (k=1, golden circles) are all clumped in lower left corner of the plots indicating their young dynamical evolutionary state. As discussed in Chapter 3, this is due to the effects of the retained BH population, which acts as energy source for the core, delaying the collapse and making it shallower. Notably, a couple of these simulations reach very small values of A_5, P_5 and $S_{2.5}$, which, in previous studies, had been found in the DRr run only (see the purple

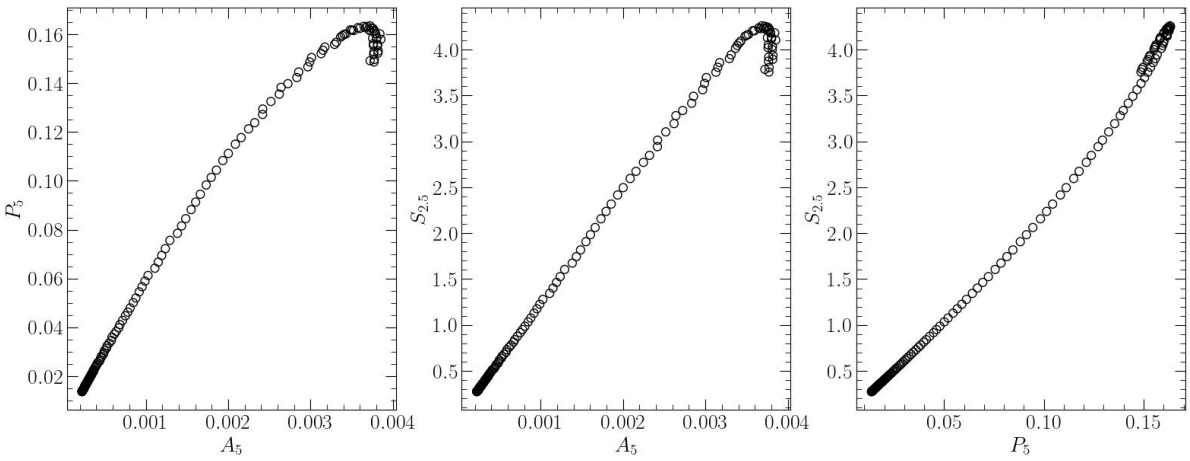

Figure 4.12: A_5 against P_5, A_5 against $S_{2.5}$ and P_5 against $S_{2.5}$ as derived by directly integrating the density profiles of King models with concentration parameter c varying from 1 to 2.5.

diamonds in Figures 4.9–4.11). This suggests that, as in DRr, also in these simulations the BHs have been retained within the system for a significant amount of time. It is also worthy to stress that a k=1 snapshot falls in dynamically old region (golden circle in red shaded region). This is simulation N500_k1_Rg2_rp0.025, the same that was named "DRe" in Section 3.5. As discussed there, this behavior is due to the fact that the cluster ejects all the DRs within the first 5 Gyr of its evolution, and it's inner regions therefore have enough time to substantially contract and reach CC around 13 Gyr. Finally, we note that no IMBHs are formed in simulations with k=1, although the opposite conclusion could have been expected in the presence of a reduced kick velocity of DRs.

Impact of R_g

Figure 4.15 is analogous to the two previous one, except for the fact that it is color-coded for different values of the initial galactocentric distance of each simulation: pink for R_g=2 kpc, orange for R_g=4 kpc, and green for R_g=6 kpc. The distribution of the parameters shows a mild dependence on R_g, in the sense that most of the simulations started with large galactocentric distance (R_g = 6 kpc) populate the lower-left corner of the diagram and the smallest values of the nCRD parameters are measured only in these systems. On the other hand, the region of dynamically old systems (red shaded) is mainly populated by clusters with R_g = 4 kpc. All the snapshots hosting an IMBH after 13 Gyr of evolution have been started at closest distance from the Galactic center among those explored in this survey (R_g = 2 Kpc).

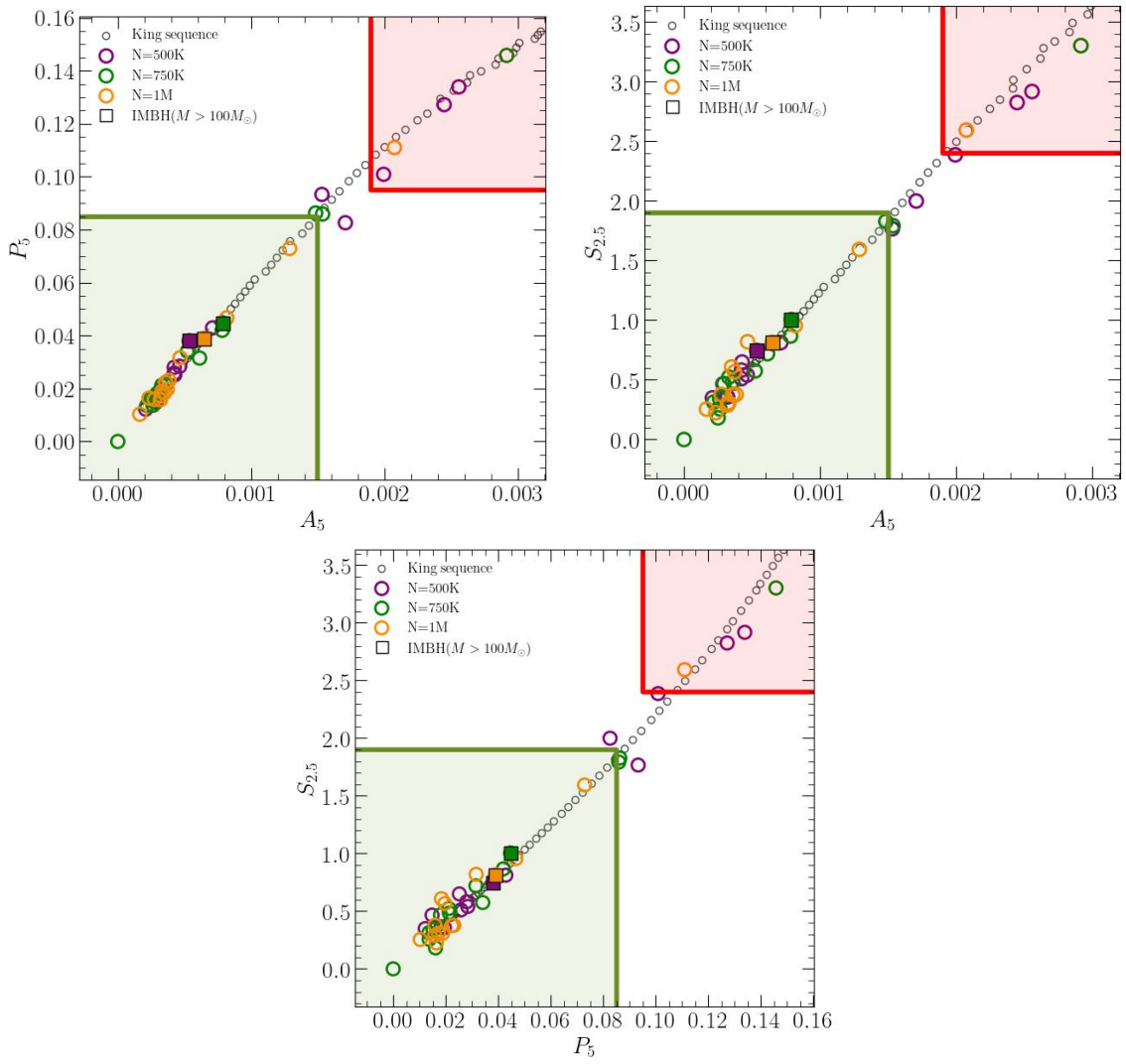

Figure 4.13: A_5 against P_5, A_5 against $S_{2.5}$, and P_5 against $S_{2.5}$ measured in the survey simulations and plotted with different colors depending on the initial number of stars N: purple for N=500K, green for N=750K, and orange for N=1M. The squares in each color represent snapshots with an IMBH at 13 Gyr. The olive green and red shaded regions are the boundaries for dynamically young and dynamically old systems, as defined in Section 4.3.2 and Figures 4.9–4.11. The king model sequences, defined in the same section, are shown as grey empty circles.

Impact of r_h/r_t

Figure 4.15 shows the results color coded for different values of r_h/r_t: red for r_h/r_t= 0.025, cyan for r_h/r_t= 0.05, and light green for r_h/r_t= 0.1. This parameter measures the compactness of the cluster, with lower values of r_h/r_t referring to the most compact systems, and vice versa. Figure clearly shows that only simulations that started with r_h/r_t= 0.025 (the most compact in the survey) reach the dynamically

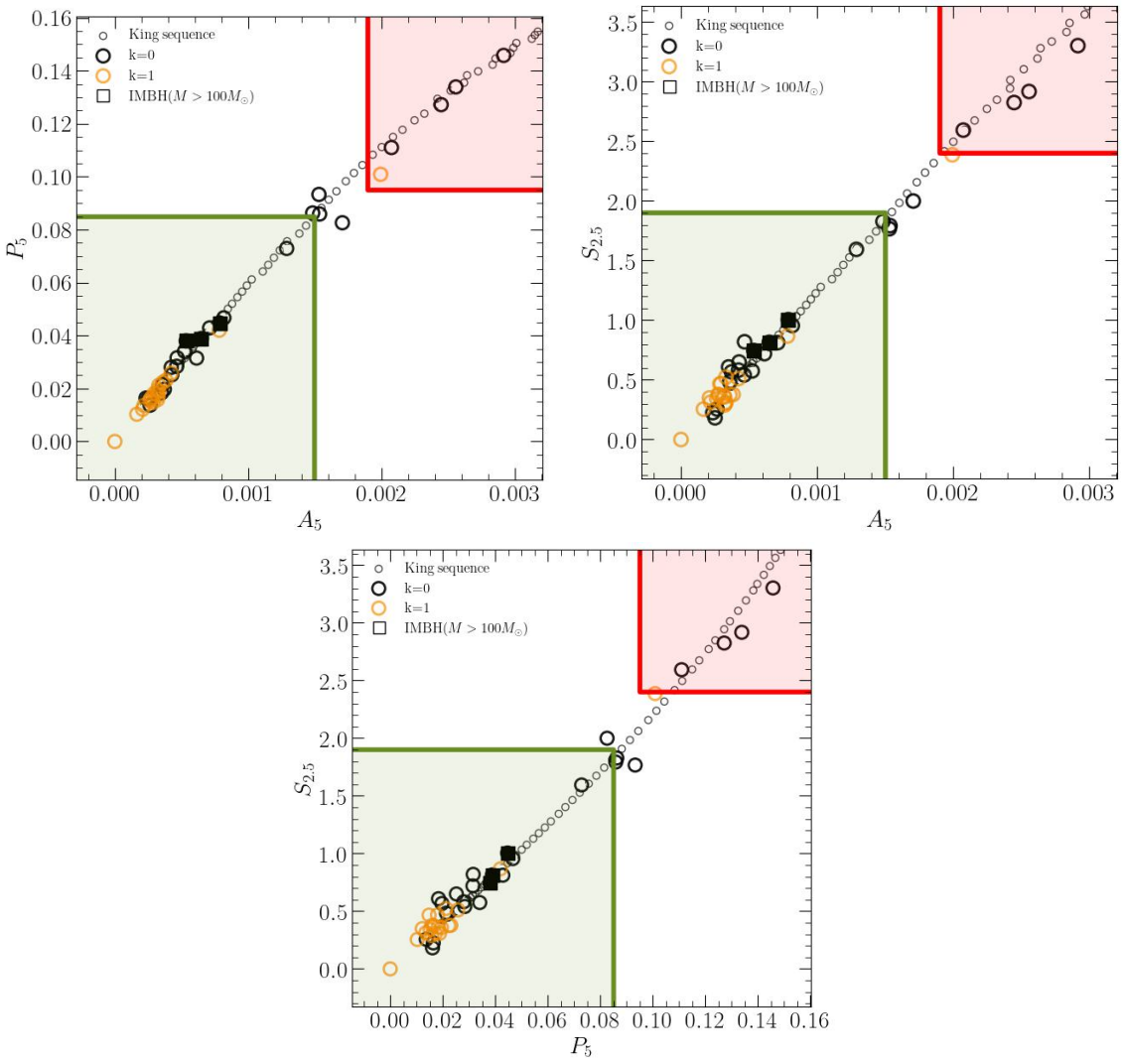

Figure 4.14: As in Fig.4.13, but color-coded for different values of k: black for k=0, gold for k=1.

old region in the plots. For higher values of r_h/r_t, the snapshots tend to occupy the dynamically young region in most of the cases. So, the initial compactness of star clusters seems to have a non-negligible influence on their subsequent dynamical evolution. Also in this case, a consideration about IMBHs is worth to be added: only clusters that were originally the most compact ($r_h/r_t = 0.025$) turn out to host an IMBH at an age of 13 Gyr.

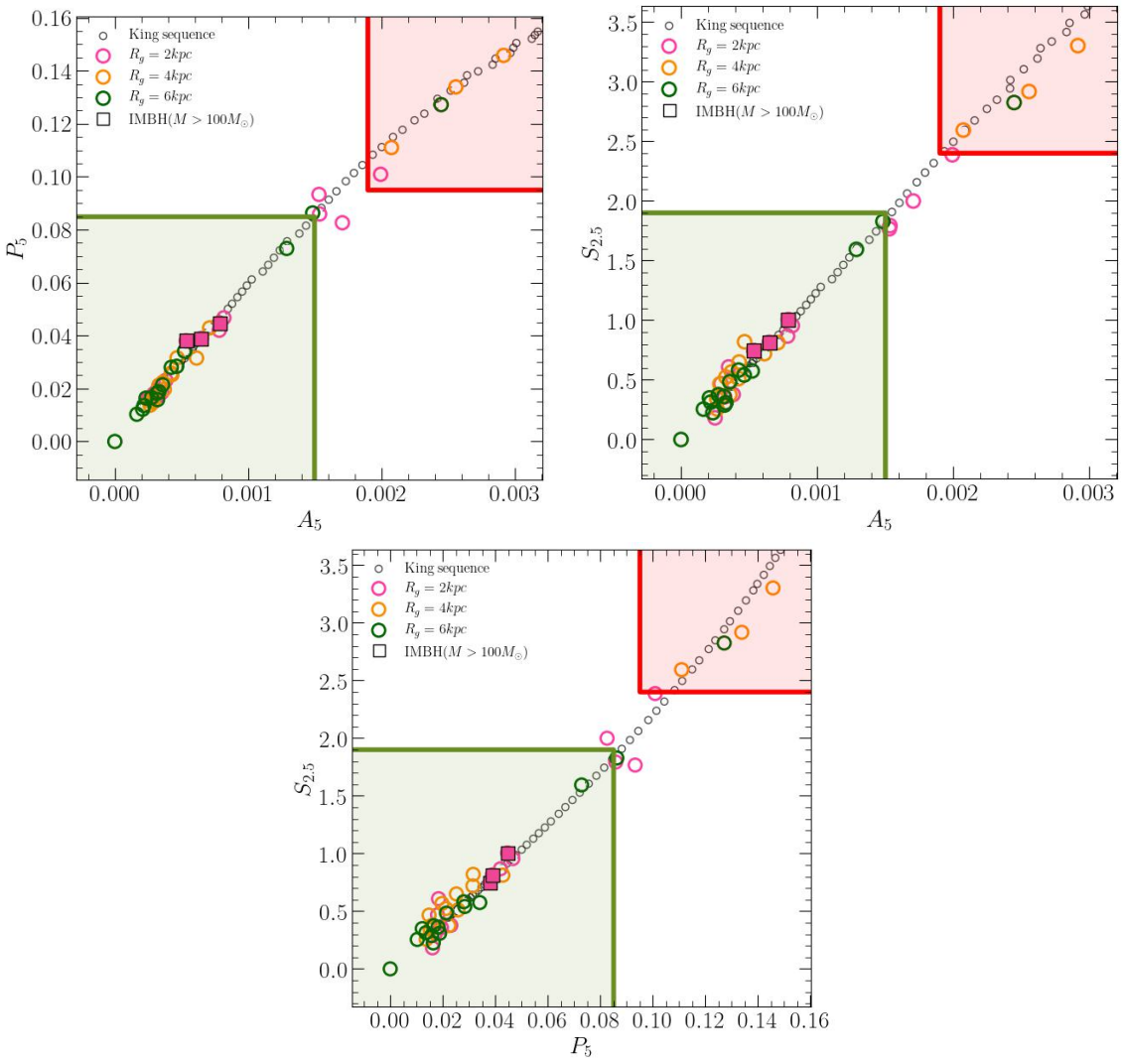

Figure 4.15: As in Fig.4.13 but for different values of R_g. The color code is as follows: pink for R_g=2kpc, orange for R_g=4kpc and green for R_g=6kpc.

4.3.4 nCRD parameters as diagnostics of dynamical evolution

Figure 4.17 shows the three parameters plotted against each other with color coding for dynamically young clusters (olive green) and dynamically old snapshots (red circles and stars), as classified from the behaviour of their 1% Lagrangian radius discussed in Section 4.1 (see also Figs. 4.1–4.6). We recall that the adopted reference boundaries (green and red shaded areas in the figure) have been chosen on the basis of the results obtained from the simulations discussed in Chapters 2 and 3, consisting of snapshots extracted from different chronological times during the cluster evolution. Conversely, the nCRD parameters plotted in the figure have been all measured

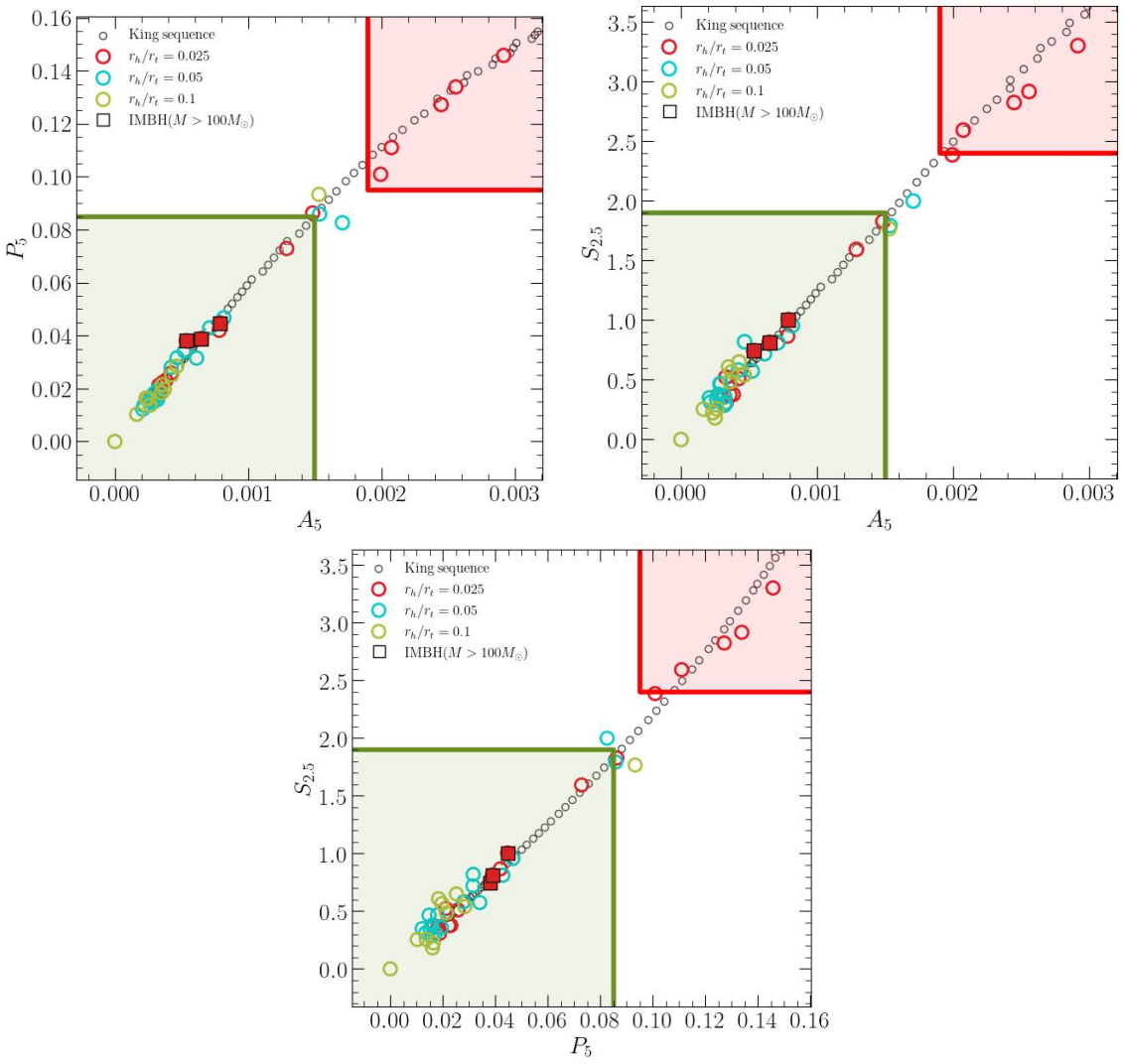

Figure 4.16: As in the Fig.4.13, but for different values of r_h/r_t, color coded as follows: red for r_h/r_t= 0.025, cyan for r_h/r_t= 0.05 ,and light green for r_h/r_t= 0.1.

in snapshots extracted at the same age (13 Gyr) from the survey simulations. Hence, it was not obvious *a priori* that the new results followed so closely the previous ones, with the boundary region of dynamically young systems (green shaded area) being populated exclusively by snapshots that have been classified so also in the survey simulations, and with the boundary region of dynamically old systems (red shaded area) including only CC and post-CC clusters of the survey simulations (there is just one exception, which is discussed below). Hence, the figure clearly demonstrates the suitability of the adopted boundaries to substantially distinguish between dynamically young and dynamically old snapshots of the survey simulations. In turn, this strongly indicates that the nCRD parameters are indeed powerful tools to determine the dynamical age of even real GCs, which started from a variety of different initial

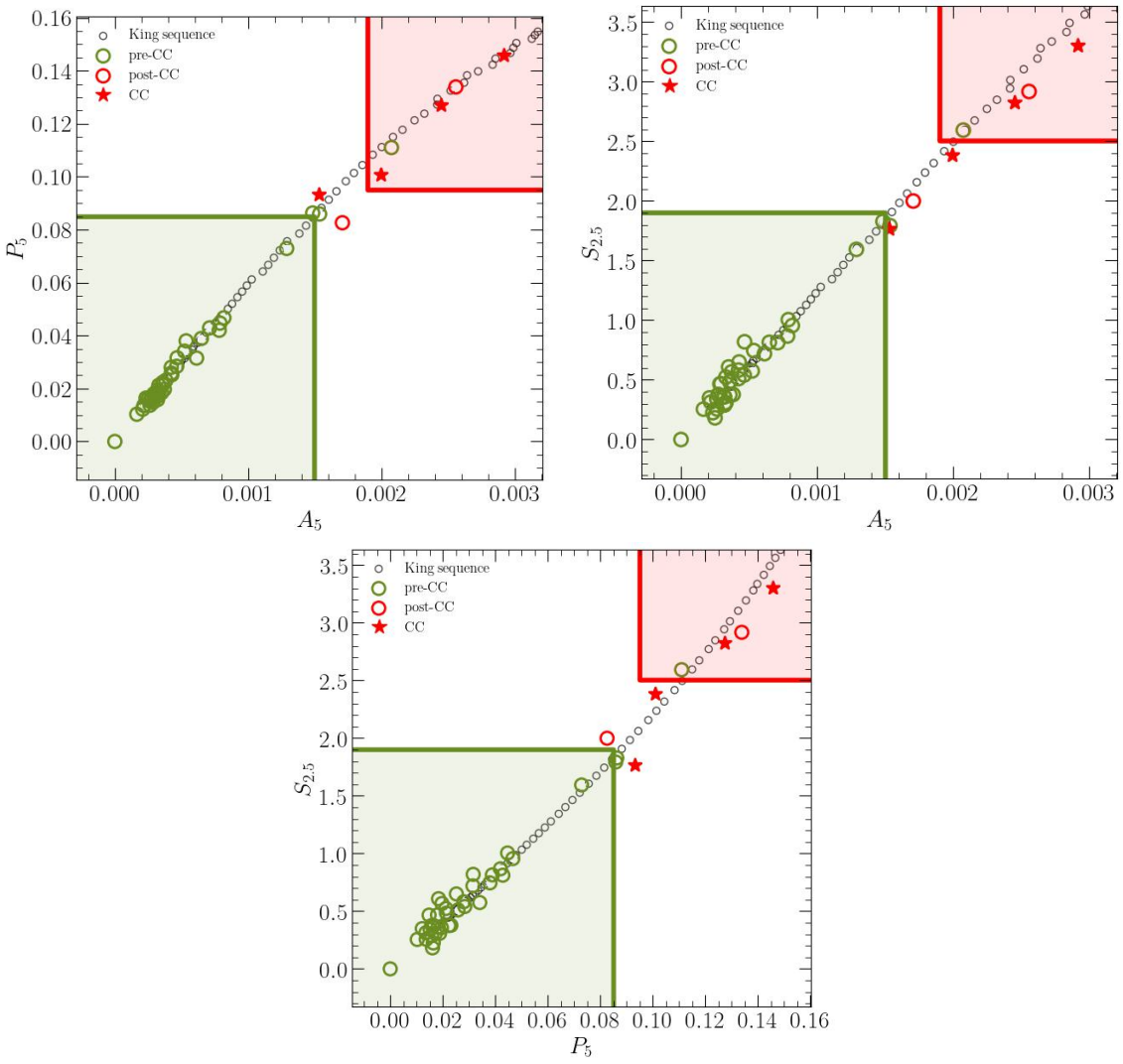

Figure 4.17: A_5 against P_5, A_5 against $S_{2.5}$, and P_5 against $S_{2.5}$ measured in the survey simulations, with the color code indicating different dynamical phases: olive green for dynamically young snapshots, red for dynamically old systems (red stars for the clusters that are very close to CC or in the CC phase, red circles for the post-CC ones).

conditions and currently have all the same chronological age of $\sim$ 13 Gyr. The only exception to this notable agreement is simulation N1_k0_Rg4_rp0.025, which is classified as dynamically young but falls in the boundary region of dynamically old clusters (green circle in the red shaded area). However, it is worth to stress that it is close to the edge of this boundary region, and it also shows a quite steep evolution of $r_{1\%}$ (see Fig. 4.5), suggesting that it is on the verge of core collapsing. Figure 4.17 also shows that there are few simulations in the area between the two boundary regions, and they are classified both as dynamically young (green circles:

simulations N750_k0_Rg6_rp0.025 and N750_k0_Rg2_rp0.05), and as dynamically old (red star: N500_k0_Rg2_rp0.1, and red circle: N500_k0_Rg2_rp0.05). Even this result is in agreement with what was found from the previous simulations: as shown in Figures 4.9–4.11, this region is populated by intermediate-age, CC, and post-CC snapshots (cyan, yellow, and blue symbols, respectively) of the BF0, BF10, and BF20 simulations. Indeed, the edges of the two adopted boundary regions have been chosen exactly from this evidence.

The analysis of Figure 4.17 therefore indicates that the general conclusions drawn in Chapters 2 and 3 about the use of the three nCRD parameters as dynamical indicators perfectly holds also for star clusters originated from different initial conditions and observed at the same chronological age (as it is the case for the population of Galactic GCs). This means that the observed clusters whose values of A_5, P_5 and $S_{2.5}$ that fall in the green or in red shaded region unambiguously indicate that the surveyed cluster is dynamically young or dynamically old, respectively. On the other hand, if an observational measure fall in the area between the two boundary regions, the only solid conclusion is that the cluster is not in an early dynamical stage, but there seems to be no means to distinguish whether it is on the verge of core collapse, or it has already experienced CC, or it is even in a post-CC stage.

A deeper examination of the figure, however, reveals that in this "region of ambiguity" the dynamically old snapshots (red stars and circles) do not align with the King model sequence, whereas the dynamically young ones lie on it. An analogous behavior is indeed observed also within the two boundary regions: the green circles in the green shaded area tend to align along the King sequence, while the red symbols in the red shaded region tend to not follow it. This is consistent with the well-known behavior of the density profile, which is properly described by the King model family in dynamically young systems, but significantly deviates from it in advanced stages of dynamical evolution (see Section 1.2.1 and Fig. 2.2). The comparison with the expectations from King models is better highlighted in Figure 4.18, which shows the three nCRD parameters obtained for survey simulations plotted against their respective concentration parameter as determined by the best-fit King model to their density profile (colored symbols), along with the same parameters obtained by directly integrating the density profile of a sequence of King models with concentration parameter c varying between 1 and 2.5, in steps of 0.05 (grey empty circles). As apparent, the values obtained for the dynamically young snapshots (green circles) well follow those expected for King models up to c$\simeq$ 1.8. Conversely, the values of A_5, P_5 and $S_{2.5}$ measured in dynamically old systems (red symbols) systematically and significantly exceed those expected for a King model with the same concentration c.[1] Very interestingly, also the dynamically young system that falls within the high

[1] Curiously, the excesses of A_5 and P_5 found for the three most evolved systems compensate each other and make these snapshots align along the King sequence in the top-left panel of Fig. 4.17. However, they align with King models of higher concentration than measured in the simulation density profiles.

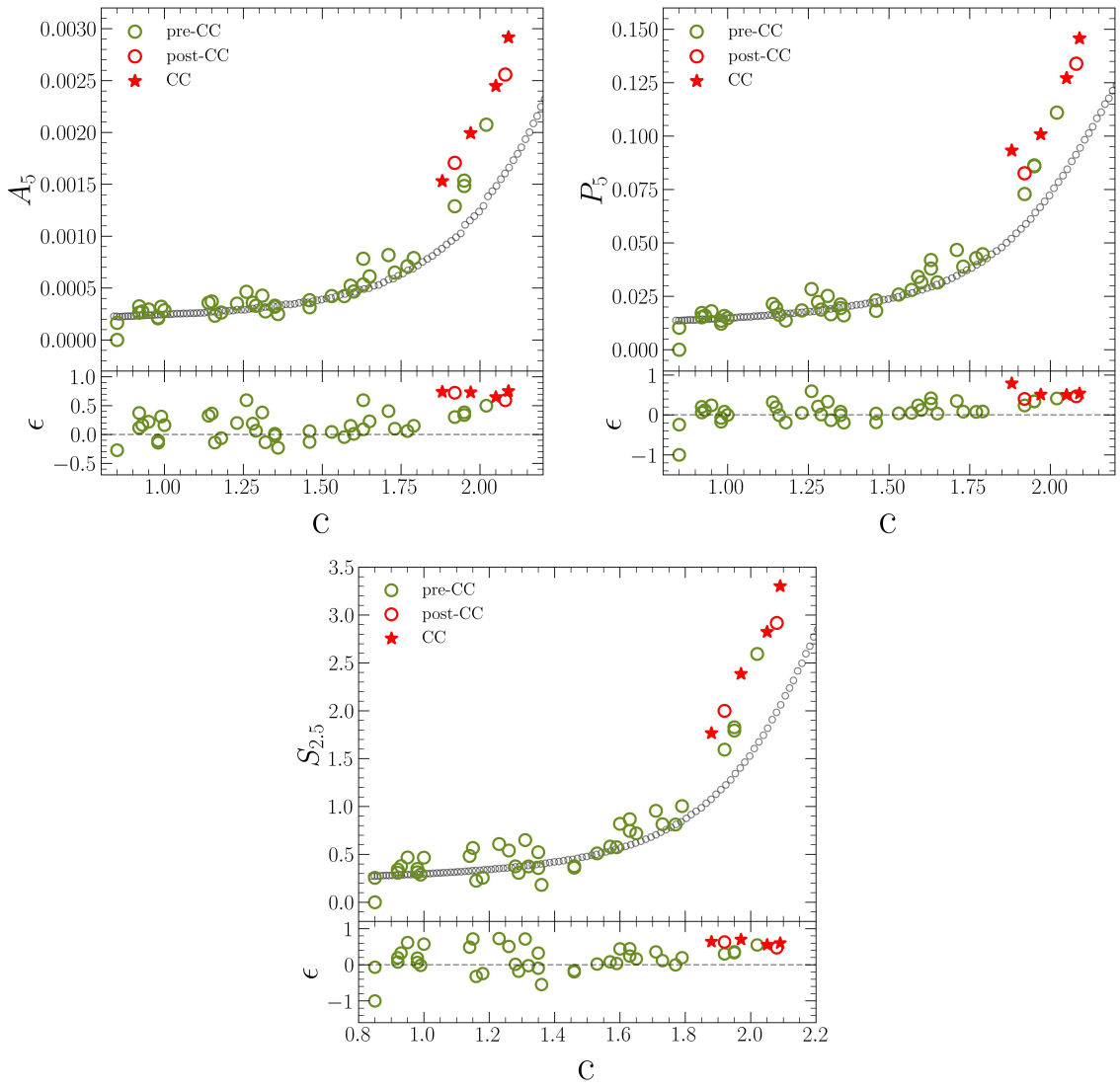

Figure 4.18: A_5, P_5 and $S_{2.5}$ measured in the survey simulation snapshots (colored symbols, as in Fig. 4.17) plotted against their concentration parameter, as obtained from the best-fit King model to their density profile. The same parameters obtained by directly integrating the density profile of King models with concentration c varying in the range 1 and 2.5, in steps of 0.05, are also plotted is grey empty circles. The bottom panel in each figure shows the residuals between the measured nCRD parameter and the value expected for a king model with the same concentration c.

dynamical evolution boundary (green circle in the red shaded region in Fig. 4.17) and the 4-5 snapshots lying the "region of ambiguity" between the two boundaries all show significant deviations from the King model sequence at c> 1.8 in Fig. 4.18. This clearly shows that the comparison between the values of A_5, P_5 and $S_{2.5}$ measured from the observed nCRD, and those expected from a King model having the

same concentration parameter as that obtained from the fit to the observed density profile can be used as an additional diagnostic tool to pinpoint systems that are in an advanced stage of dynamical evolution, although they formally have not reached CC yet.

4.4. Discussion and summary

In this chapter we have presented the values of the three nCRD parameters measured in 46 snapshots extracted at the same evolutionary time (13 Gyr) from a survey of simulations (MOCCA code) started from different initial conditions (N, k, R_g and r_h/r_t). The snapshots have been analyzed following the same methods usually implemented in observational studies. They are representative of the Galactic GC population in terms of King concentration, core and half-light radii, as derived from the King fit to their projected density profile.

From the time evolution of their 1% Lagrangian radii, we classify them as pre-CC, CC and post-CC. Taking advantage of the results obtained from the simulations with different primordial binary fractions and DRs, described in Chapter 3, we define boundaries for dynamically young and dynamically old snapshots in the plots of A_5 against P_5, A_5 against $S_{2.5}$, and P_5 against $S_{2.5}$. Additionally, the three parameters measured for King models with concentration c varying in the range 1 and 2.5, in steps of 0.05 are used as reference models (King sequence) in the aforementioned three plots of parameters.

The comparison of the location in these plots of the nCRD parameters computed for the snapshots of the survey simulations, with the adopted boundary regions for dynamically young and dynamically old snapshots, and the King reference sequence, enables us a thorough examination of capability their to pinpoint the dynamical stage of the simulated clusters. From these plots, we observe that the majority of the survey simulation snapshots fall inside the boundary for dynamically young snapshots, and only few snapshots (7 out of 46) fall in the dynamically old region or are classified as CC or post-CC in the area between the two boundaries. Curiously, this is similar to the fraction (15-20%) of GGCs classified as dynamically old.

Close examination of these plots in terms of each initial conditions indicates that the nCRD parameters show a mild dependency on the initial number of stars (N) and the galactocentric distance (R_g), whereas they strongly depend on the adopted BH kick velocity prescription (k) and, less so, on the initial compactness parameter (r_h/r_t). In particular, clusters with k=0 cover the entire range of values of the three parameters, while the ones with reduced kick velocity for BHs (k=1) all have low values of the three parameters. This is indicative of young dynamical ages, which are explainable as due to the heating effect of the BH population retained in them. Only one of the snapshot with k=1 falls in the dynamically old region. This has been extensively described in Chapter 3 as “DRe simulation", which ejects all the BHs early on in it’s

life and has enough time to undergo two-body relaxation significantly to reach CC around 13 Gyr. In addition, the clusters with higher values of r_h/r_t tend to occupy the dynamically young region in most of the cases. Noteworthy, IMBHs are always formed in simulations with no DR retention ability (k=0), shorter galactocentric distance (R_g= 2 kpc), high compactness (r_h/r_t= 0.025), and they always occupy the dynamically young region indicating their young dynamical age.

The analysis of the same plots also reveals that their dynamical classification closely follows that of all previous simulations (described in Chapters 2 and 3), as traced by the adopted reference boundaries. Although both classifications are based on the time evolution of $r_{1\%}$, this result was not obvious *a priori*, because the snapshots analyzed here are extracted at the same age (13 Gyr) from several clusters with different initial conditions and different dynamical evolutionary histories, while all the previous studies dealt with snapshots extracted for a few representative cases at very different ages, from $\sim$ 3 to $\sim$ 13 Gyr. This result, in spite of some exceptions, broadly suggests that, from an observational point of view, the nCRD parameters can be effectively used to determine the dynamical age of real GCs, despite their different initial conditions.

In agreement with what is observed in the previous analyses, the snapshots that fall in the "ambiguous region" between the two adopted boundaries can be in pre-CC, CC and post-CC stages. Notably, however, the inspection of the $r_{1\%}$ time evolution of the snapshots lying in the ambiguous region and classified as pre-CC reveals that they likely are on the verge of collapsing, certainly never being in early dynamical phases.

We finally emphasize that both the snapshots that fall within the dynamically old boundary, and those lying in the ambiguous region show significant deviations from the King model sequence, in the direction of having larger values of A_5, P_5, and $S_{2.5}$ than expected from a King model with their same concentration parameter c. This attribute could be exploited to infer the advanced dynamical age of the clusters even if they are in ambiguous region, and calls for deeper investigations (in terms, e.g., of current fraction of binary systems, neutron stars, and black holes) to try and identify the main responsible(s) for the position of the nCRD parameters in these diagrams.

Chapter 5

Conclusions

5.1. Summary

Understanding the dynamical evolution of GCs brings crucial information on the formation and evolutionary processes of these systems (thus, in turn, on the assembly history of their host galaxy), as well as on their present-day physical and observational properties. For instance, the rate of stellar interactions (both collisions and mass transfer in binary systems) is thought to be larger in high density environments, and the long term dynamical evolution tends to increase the central density of GCs. Hence, the formation rate of stellar exotica, as blue straggler stars, cataclysmic variable stars, and interacting binaries containing black holes and neutron stars, should increase in late dynamical stages, thus demonstrating the impact that the internal dynamical evolution can have on the stellar population content of the host cluster. In turn, the presence of these objects, especially binaries of compact objects, in the cluster core can act as energy source and quench mass segregation. In addition, an effect of core expansion due to stellar-mass BHs has been invoked to explain the correlation between core radius and age observed in the Large Magellanic Cloud star clusters (Mackey & Gilmore, 2003; Mackey et al., 2008). However, Ferraro et al. (2019) showed that the large and small core radii measured for the old GCs in the sample can be more naturally explained by different dynamical ages, with the dynamically older systems having smaller core radii than the younger ones. This further demonstrates the importance of understanding which dynamical stage a GCs is in.

Many dynamical indicators have been proposed in the recent years, either based on peculiar populations of heavy stars (as blue stragglers) that are sensitive tracers of the dynamical friction efficiency (e.g., Ferraro et al., 2012, 2018a, 2019; Lanzoni et al., 2016), or based on the internal mass and kinematic structure of each system (e.g., Baumgardt & Makino, 2003; Tiongco et al., 2016; Bianchini et al., 2016; Webb & Vesperini, 2017; Bianchini et al., 2018). The approach most commonly adopted to estimate the clusters' dynamical ages and establish their current dynamical phase

relies on the properties of the projected density profile of the system and its comparison with King (1966) models. In particular, a steep central cusp in the projected density profile is used to identify CC and post-CC clusters. However, the cusp not only becomes shallower in core re-expansions during the post-CC evolution, but it can also be hardly detectable from observational data, especially in very dense and distant systems. This might be the reason why a low fraction (15-20%) of GGCs is classified as CC, in spite of their the central relaxation time being significantly shorter than their age in most of the cases. This calls for more robust and reliable diagnostics, which is indeed the specific goal of this thesis.

In this work, we propose new observational indicators of the dynamical evolutionary states of GCs based on the inner radial distribution of cluster stars, and we explore their possible dependence on cluster properties such as primordial fractions of binaries and DRs, and various initial conditions. For this purpose, we used Monte Carlo simulations performed with the MOCCA code, which closely follow the dynamical evolution of GCs. With the final aim to use the new diagnostics on observed GCs, we analyze the simulations at various phases of their evolution from an observer's perspective.

By extracting totally 38 time snapshots from a simulation started with dimensionless central potential $W_0 = 6$, 500K stars, and no primordial binary fraction, we first investigated the star density profile and the density cusp diagnostic that is used in most observational works as indicators of the dynamical state of the cluster, confirming that it is always present in highly evolved systems, but it can be hard to detect in the post-CC phase. Then, from the same set of time snapshots, we found that the normalized cumulative radial distribution drawn by the stars located within one half of the half-mass radius ($0.5r_h$) from the center shows a clear sensitivity to the dynamical evolution of the system, becoming progressively steeper for increasing dynamical age in the innermost cluster regions and thus indicating that the morphology of the nCRD could be used as diagnostics of the dynamical state of the cluster. We thus performed an extensive exploration of new possible parameters that could quantify the nCRD morphological differences. This lead us to define three new diagnostics: A_5, which is the area subtended by the nCRD between the cluster centre and 0.05 rh; P_5, which is the number of stars within 0.05 rh; and $S_{2.5}$, which is the slope of the straight line tangent to the nCRD at 0.025 r_h. The time evolution of these three parameters enables us to clearly distinguish pre-CC clusters from post-CC clusters. In fact, their values remain low and constant in the early evolutionary phases, they progressively increase with time and reach a maximum at CC, then vary around large values during the gravothermal oscillations, never decreasing to the initial low values.

We then extended the same analysis and test the new diagnostics on a set of five additional Monte Carlo simulations of GCs: three simulations (namely, BF0, BF10, BF20) have different initial binary fractions (0%, 10%, 20% respectively), the other two simulations (namely, DRr and DRe) started with a reduced kick velocity for stel-

lar mass black holes. We found that the time variations of the three parameters are most pronounced for the BF0 simulation and less pronounced in simulations BF10 and BF20. Nevertheless, the three nCRD parameters allow the distinction between clusters in early and in advanced dynamical stages also with non-zero primordial binary fractions. In the case of simulations with reduced kick velocity for black holes, if a significant number of these compact objects is retained for a large fraction of the cluster life (as in the DRr run), the three nCRD parameters do not evolve with time and maintain values lower than observed in all previous simulations, because black holes act as energy sources and don't let the cluster evolve dynamically. Conversely, in the simulation that ejects most of the black holes at a young age (DRe), the three parameters show similar trends as in the cases with no dark remnants, where the cluster undergoes dynamical evolution without any hindrance from additional energy sources (retained black holes).

As further step of this investigation, to accommodate the fact that the GCs in our galaxy all have essentially the same, old age, but are observed in different stages of their internal dynamical evolution, we analyzed a survey of 46 simulations whose "observed" properties (King concentration, core and half-light radii) match those of the population of GGCs. Being generated from a broad range of different initial conditions, these simulated clusters are subject to different rates of internal dynamical evolution, but they have been all considered at the same chronological age of $\sim 13 Gyr$. Some of these clusters harbour dark remnants (black hole sub-systems and IMBHs) which have a major effect on long term dynamics. To verify the ability of the previously defined nCRD parameters as dynamical indicators, here we mainly use plots showing one parameter against another (A_5 against P_5, A_5 against $S_{2.5}$, and P_5 against $S_{2.5}$) where we draw reference boundaries for dynamically young and dynamically old snapshots based on the results from Chapter 3, and reference sequences of the same parameters as obtained by direct integration of King models. We see that for the majority of the survey simulation snapshots, the dynamical classification based on $r_{1\%}$ closely follows the reference boundaries, with small and large values of the nCRD parameters falling, respectively, in the dynamically young and dynamically old boundary regions. The dependency of these parameters on the adopted BH kick velocity prescription is quite evident, as all the snapshots with DRs have low values of the parameters due the heating effect of the BH population retained. Similar results are found in the cases of snapshots with IMBHs. Adding on to these results, we also found that the dynamically old snapshots and those falling in the region between the two reference boundaries (which are classified both as pre-CC, and as CC or post-CC clusters) significantly deviate from the King model sequence, having higher values of A_5, P_5 and $S_{2.5}$ than expected from the King models corresponding to their best-fit King concentration. This evidence, in agreement with the steep time-dependence of their 1% Lagrangian radius, suggests that even the ones that are classified as pre-CC are, indeed, in an advanced stage of dynamical evolution.

5.2. Discussion and Future Perspectives

Overall, the investigation performed so far shows that the three newly define nCRD parameters are powerful tools to differentiate dynamically-old from dynamically-young clusters, irrespective of their initial conditions at formation. Compared to dynamical evolution diagnostics previously defined in the literature (as the central density cusp, radial variations of the stellar mass function, the presence of orbital anisotropy, the velocity dispersion profile of different stellar mass groups, the segregation of blue straggler stars; e.g, Baumgardt & Makino 2003; Tiongco et al. 2016; Bianchini et al. 2016; Bianchini et al. 2018; Webb & Vesperini 2017; Ferraro et al. 2018a), the main advantage of these parameters is that they are much easier to measure from observations and require no arbitrary assumptions, like, e.g., the choice radial binning, or of the radial distance within which to define the density cusp. With respect to the detection of a central density cusps, A_5, P_5, and $S_{2.5}$ also appear to be a sort of magnifiers able to pinpoint clusters with density profiles deviating from the King model distribution well before the cusp is measurable from observation.

Likely, their potential will even further increase as soon as more work, both theoretical and observational, is done. In particular, the few "ambiguous" cases, especially the pre-CC clusters that fall in the dynamically-old region and in the area between the two adopted boundaries, suggest that a classification just based on the time behavior of the 1% Lagrangian radius is too rough. A deeper investigation of the results in the light of the present-day cluster properties (e.g., the binary fraction, the number of BHs and neutron stars, the total mass or central density, etc., at 13 Gyr) is also needed to clarify how they impact the dynamical evolution of the host system. In the same perspective, it is important to take into proper account the rate at which DRs are ejected from the cluster, as well as the epoch when an IMBH forms in the center. This could allow a more reliable and finer ranking of GCs in terms of their stage of internal dynamical evolution, than what currently feasible just on the basis of $r_{1\%}$. Of course, also the determination from the same simulations of the other diagnostics proposed in the literature and their comparison with the nCRD parameters is crucial to both clarify the potential of each indicator, and to get deeper insights on GC dynamical evolution. From the theoretical point of view, we also foresee to analyze additional simulations started from different initial conditions, with the aim to properly sample the entire range of structural parameters covered by GGCs (see Fig. 4.7).

Forthcoming work will be dedicated to determine the three nCRD parameters in a large sample of observed star clusters. This requires photometric observations *(i)* with a high enough angular resolution to resolve individual stars even in the innermost cluster regions, *(ii)* sampling each system at least out to $0.5 \times r_h$, and *(iii)* deep enough to reach a few magnitudes below the MS-TO. These requirements are achieved by most HST and adaptive-optics assisted observations currently avail-

able for many GCs, thus making the determination of the three parameters from observations relatively straightforward, although particular care is needed to deal with typical observational difficulties as the photometric incompleteness, differential reddening and Galactic field contamination.

The first crucial question to answer is whether or not the values measured from observational data are consistent with those obtained from the simulations. Preliminary indications (obtained from a Master Thesis recently discussed at the University of Bologna) suggest that this is indeed the case, confirming that the nCRD parameters can be used for the dynamical classification of "real" GCs. Then, also from the observation point of view, it will be crucial to compare the dynamical ranking based on the nCRD parameters, with that inferred from other diagnostics. In particular, we plan to compare them with the values of the A^+ parameter (Alessandrini et al., 2016), which has been already measured in $\sim 1/3$ of GGCs (Ferraro et al., 2018a) and in 5 old clusters in the Large Magellanic Cloud (Ferraro et al., 2019), and in 2 young clusters in the Small Magellanic Cloud (Dresbach et al., 2022).

By quantifying the level of central segregation of blue straggler stars, the A^+ parameter provides a proper ranking of GCs in terms of their dynamical age, as testified by its strong correlation with the central relaxation time t_{rc} (or the number of t_{rc} experienced since cluster formation, $N_{\rm relax}$; see the right panel of Fig. 1.5). The scatter of this correlation might indicate that t_{rc} is a not a very precise measure of the dynamical age of star clusters, consistently with the fact that it is obtained through equation (1.4) under strong simplifying assumptions, as spherical symmetry, absence of orbital anisotropy and rotation, and a cluster well described by a King model. Hopefully, the nCRD parameters will show a thinner correlation with A^+, implying that we finally have found powerful diagnostics of dynamical evolution that are both reliable and precise, and also easy to determine from observations.

Appendix A

NGC 6440

Mainly based on:
Pallanca, Lanzoni, [...], Bhat, et al. (2021), ApJ, 913, 137

This chapter is meant to show an example of determination of the star density profile applied to observational data for one of the Milky Way GCs (namely, NGC 6440). This is indeed the same procedure adopted for the analysis of the Monte Carlo simulation time snapshots in the previous chapters, which allowed us to estimate the King model parameters (especially the half-mass radius) that are needed for the determination of the new dynamical indicators. The accurate characterization of observed GCs in terms of structural properties, dynamical status and internal kinematics is a crucial step to understand the complex dynamical processes that occur in them. Here, the case of observed GC in galactic bulge, NGC 6440 has been presented where we determine the gravitational center, projected density profile, and structural parameters from resolved star counts. The systematic use of Hubble Space Telescope (HST) and, more recently, adaptive optics assisted observations has opened the possibility of constructing projected density profiles directly from star counts even for the innermost regions of high-density stellar systems, not only in the Galactic halo and bulge (e.g., Ferraro et al. 2009b; Saracino et al. 2015; Ferraro et al. 2021), but also beyond the Milky Way (Lanzoni et al., 2019). In spite of this, the vast majority of GC structural and morphological parameters currently available in largely used catalogs (e.g., Harris 1996; Mackey & Gilmore 2003; McLaughlin & van der Marel 2005) are still derived from surface brightness (SB) profiles. In previous works (see Ferraro et al. 1999b; Lanzoni et al. 2007a,c,b, 2010; Lanzoni et al. 2019; Miocchi et al. 2013), it has been demonstrated that the advantage of determining the cluster structural parameters from individual star counts instead of SB. By construction, SB profiles directly depend on the luminosity of the surveyed stars and can therefore be artificially distorted by the sparse presence of luminous sources (see, e.g., Noyola & Gebhardt, 2006, for the discussion of methods trying to correct for this problem) and/or reddening bubbles within the field of view (FOV). Instead,

this has no impact on the density distribution obtained from resolved star counts since every object has the same weight independently of its luminosity. In addition, if proper motions can be measured, field stars (that may be particularly bright and substantially contribute to SB) can be explicitly excluded from the determination of the number count density profile. Hence, although SB can be helpful in cases of severe photometric incompleteness of the catalogs (e.g., Santos et al., 2020), it should be always used with caution, and number counts generally represent the most robust way for determining the cluster structural parameters (e.g. Lugger et al., 1995; Ferraro et al., 1999b). Moreover, once the cluster core is full resolved into individual stars, the determination of the center of gravity of the system becomes possible by simply averaging the coordinates of the detected stars. Indeed, we were among the first teams in promoting and adopting the center of gravity, instead of the center of luminosity, as optimal proxy of the cluster center (Montegriffo et al. 1995, see also Calzetti et al. 1993). However, apart from a few studies regarding individual or very small sets of clusters (e.g. Salinas et al., 2012), these techniques have not be fully exploited in the literature yet, because constructing complete samples of stars in the highly crowded central regions of GCs is not an easy task (Ferraro et al., 1997b,a; Raso et al., 2017).

Our group already published resolved star density profiles for stellar systems in different dynamical stages of their evolution (both pre- and post-core collapse GCs; see Lanzoni et al., 2010; Miocchi et al., 2013, and Ferraro et al., 2009a; Dalessandro et al., 2013, respectively), both in the Galaxy and in the Large Magellanic Cloud (Lanzoni et al., 2019). Here we present the determination of the star density profile and the structural parameters for the bulge GC NGC 6440, for which we recently built a high-resolution extinction map able to correct for the strong differential reddening effects in the direction of the cluster (Pallanca et al., 2019). The appendix is organized as follows. In Section A we describe the used dataset and the main steps of the data analysis. The procedure adopted to determine the gravity center is reported in Section A. In Section A we describe the method used to obtain the observed star count profile and the determination of the structural parameters through its fit with the King model family. Section A reports the estimate of the distance modulus and the age. The identification of the RGB-bump and the comparison with the literature is presented in Section A. Finally, in Section A we discuss the main results and we summarise the conclusions.

Observations and data analysis

To properly sample the entire radial extension of NGC 6440, in the present work we used a combination of high-resolution and wide-field images, complemented with catalogs from public surveys.

The highly crowded central regions of the system have been investigated by means of HST data, consisting in a series of deep images acquired with the Wide Field Camera

3 (WFC3) through different filters (especially, F606W and F814W) and in various epochs (see Table 1). This is essentially the same dataset used in Pallanca et al. (2019) to construct the extinction map in the direction of the cluster. Hence more details can be found there. Here we just remind that this dataset provides us with two different samples: (a) the *HST-PM sample* including all the stars with measured proper motion (PM), thus allowing the decontamination from possible non-cluster members (Galactic field stars), and (b) the *HST-noPM sample* including also the stars observed in only one epoch (hence, with no PM measure) and covering a larger area on the plane of the sky.

For the intermediate cluster region, we used ground-based data acquired with the FOcal Reducer/low dispersion Spectrograph 2 (FORS2) mounted at the ESO Very Large Telescope at Paranal Observatory (Chile) and retrieved from the ESO Science Archive. The FORS2 imaging detector consists of a mosaic of two 2000x4000 pixel MIT CCDs (15 μm/pixel) that combines a relatively large FOV ($6.8' \times 6.8'$) and reasonably high-resolution capabilities (pixel size of $\sim 0.25''$) for the standard resolution set up. The core of the cluster is roughly located at the center of the FORS2 FOV. Only one image in the $V_{\rm BESS}$ and one in the $I_{\rm BESS}$ filters were available for NGC 6440.

To properly sample the cluster outskirts and beyond, we retrieved (from *https://catalogs.mast.stsci.edu/panstarrs/*) the Pan-STARRS catalog for a circular region of $700''$ radius centered on NGC 6440. The Panoramic Survey Telescope and Rapid Response System (Pan-STARRS) is a wide-field photometric survey operated by the Institute for Astronomy at the University of Hawaii, performed with a 1.4 Gigapixel camera (GPC1) mounted at a 1.8 meter telescope, in five broad-band filters (g, r, i, z, y). For the present analysis we used only i and r data.

The detailed description of the data analysis procedure for the HST dataset can be found in Pallanca et al. (2019). Here we just summarize the main steps. The photometric analysis has been carried out by using the DAOPHOT package (Stetson, 1987). The point spread function (PSF) for each image has been modelled on several bright and isolated stars, by using the DAOPHOTII/PSF routine. Then PSF-fitting photometry has been performed independently on all the images by imposing a source detection threshold more than 5-σ above the background level and, a master list has been produced considering as reliable sources all the objects measured in more than half of the images in at least one filter. We then run the ALLFRAME package (Stetson, 1987, 1994) that simultaneously determines the brightness of the stars in all the frames, while enforcing one set of centroids and one transformation between all the images. Finally, the magnitudes obtained for each star have been normalized to a reference frame and averaged. The photometric error was derived from the standard deviation of the repeated measures. The instrumental magnitudes have been calibrated to the VEGAMAG system by using the photometric

zero points reported on the WFC3 web page[1]. Geometric distortions have been corrected following the prescription of Bellini et al. (2011) and then reported to the absolute coordinate system (α, δ) as defined by the World Coordinate System by using a sample of stars in common with the publicly available Gaia DR2 catalog (Gaia Collaboration et al., 2016a,b). The resulting astrometric accuracy turns out to be $< 0.1''$.

A similar procedure was adopted in the analysis of the FORS2 wide-field dataset. In summary, per each exposure we modelled the PSF by using dozens of bright, isolated and non saturated stars and we applied such model to all the sources detected at 3-σ above the background level. In a second step we created a master list containing all the detected sources and for each object we forced the fit in both filters. The further step consisted in the creation of the catalog listing all the magnitudes measured in both filters. Finally, the instrumental positions have been reported to the absolute coordinate system by using a sample of stars in common with the Gaia DR2 catalog. In order to make the three catalogs homogeneous in magnitude, we calibrated the V_{BESS} and I_{BESS} magnitudes of FORS2 onto the HST F606W and F814W magnitudes, respectively, by using color equations obtained from a large number of stars in common between the two datasets. Then, we used the stars in common between Pan-STARRS and FORS2 to homogenize the r and i magnitudes of the former with the FORS2 magnitudes previously calibrated onto HST. Hence, at the end of the procedure, the magnitudes measured in the three datasets are all homogeneous and calibrated in the same (HST) system. From now on, we use the symbols V_{606} and I_{814} to indicate both the HST magnitudes, and the magnitudes of the other two datasets calibrated onto the F606W and the F814W bands, respectively.

Four catalogs have been obtained from the available datasets. The *HST-PM* catalog includes all the stars measured in the portion of the cluster where multi-epoch WFC3 images have been acquired. It has been corrected for differential reddening (see Pallanca et al., 2019) and decontaminated from Galactic field stars via PM analysis. It counts 137194 stars. The *HST-noPM* catalog is made of all the stars detected in the portion of the cluster surveyed by all the available WFC3 observations. It reports the observed magnitudes (with no correction for differential reddening) for a total of 174418 objects. The *FORS2* catalog contains 27487 stars measured in a roughly square region of $200''$ size around the cluster center. The *Pan-STARRS* catalog lists 40419 stars within a circle of $700''$ radius.

Figure A.1 shows the spatial distribution of all the stars included in each of the four catalogs (blue dots), with respect to the cluster center. The corresponding color-magnitude diagrams (CMDs), which are plotted in Figures A.2 and A.3, are deep enough to trace the (cluster and field) stellar populations down to 3-4 magnitudes below the cluster Red Clump. Of course, an increasing population of field stars appears and becomes dominant with respect to cluster members for increas-

[1] http://www.stsci.edu/hst/wfc3/phot_zp_lbn

Instrument Survey	Program ID	PI	Filter	$N_{exp} \times T_{exp}$
WFC3 [1]	GO 11685	Van Kerkwijk	F606W	1×392 s + 1×348 s
			F814W	1×348 s + 1×261 s
WFC3 [1]	GO 12517	Ferraro	F606W	27×392 s
			F814W	27×348 s
WFC3 [1]	GO 13410	Pallanca	F606W	5×382 s
			F814W	5×222 s
			F656N	10×934 s
WFC3 [1]			F606W	5×382 s
			F814W	5×222 s
			F656N	10×934 s
WFC3 [1]			F606W	5×382 s
			F814W	4×222 s + 1×221 s
			F656N	6×934 s + 2×864 s +2×860 s
WFC3 [1]	GO/DD 15403	Pallanca	F606W	2×382 s
			F814W	1×223 s + 1×222 s
			F656N	2×969 s + 2×914 s
FORS2	077.D-0775(B)	Saviane	V_BESS	1×30 s
			I_BESS	1×30 s
GPC1 [2]			r	
			i	

Table A.1: Summary of the used dataset. [1]=Pallanca et al. (2019), [2]=Pan-STARRS.

ing distances from the cluster center, i.e., from the HST, to the FORS2, to the Pan-STARRS dataset.

Determination of the center of gravity

As discussed in many previous works (see, e.g., Montegriffo et al., 1995; Ferraro et al., 1997b, 1999b), dealing with resolved stars for the determination of the cluster center avoids introducing the bias induced by the possible presence of a few bright stars, which can generate a SB peak in an off-set position with respect to the true gravitational center. Here we thus took advantage of the *HST-PM* catalog, which properly samples the central region of the cluster, is corrected for the effects of differential reddening, and has been decontaminated from field star interlopers (see Figure A.3). We used the same iterative procedure already adopted, e.g., in Lanzoni et al. (2007a,c, 2010); Lanzoni et al. (2019), where the gravitational center (C_{grav}) is determined by averaging the (x, y) coordinates on the plane of the sky of all the stars observed in a selected range of magnitude and within a circle of radius r

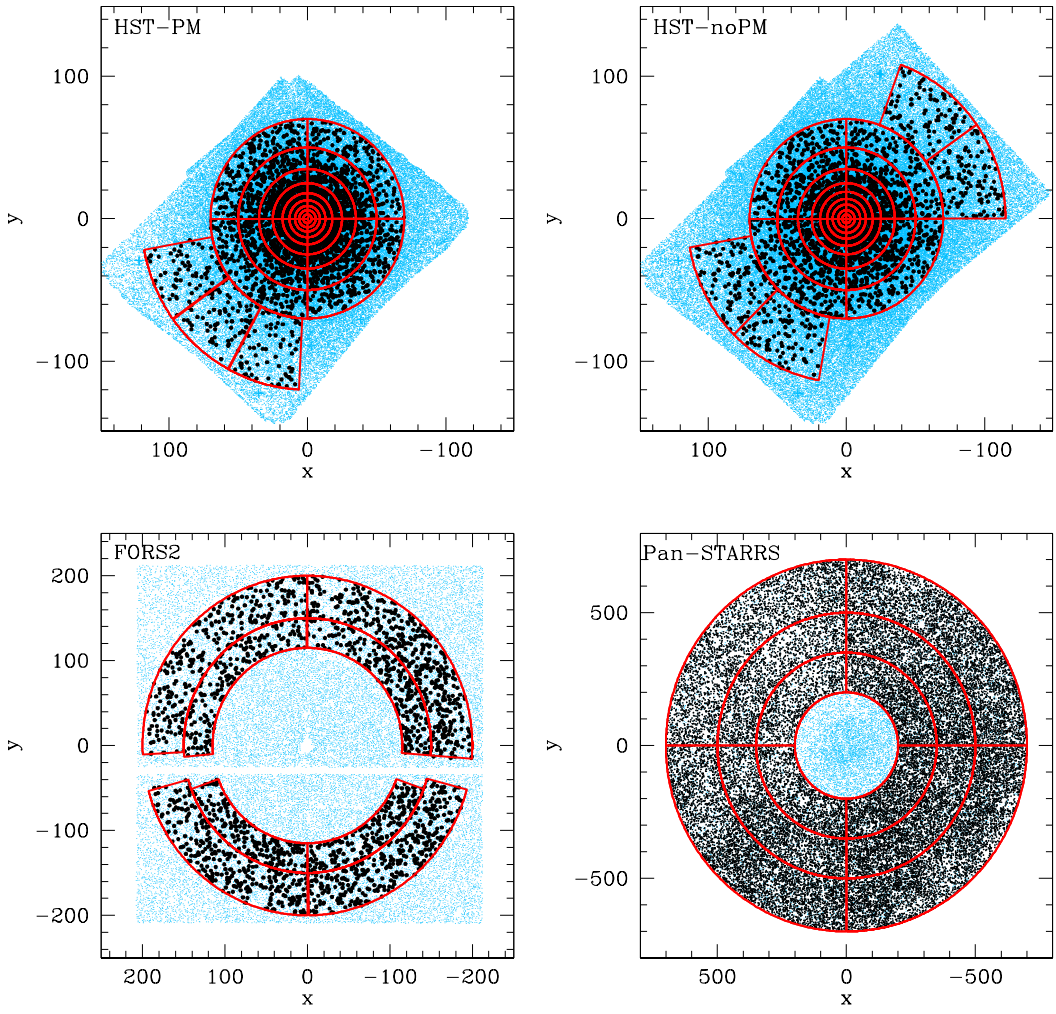

Figure A.1: Spatial distribution of all the observed stars in each catalog (blue dots), with respect to the newly determined cluster center (see Table A.2). The black dots correspond to the objects used to determined the cluster density profile: stars with $I_{814} < 19$ beloging to the HST-PM catalog (used to build the density profile shown in red in Figure A.4) and stars with $I_{814} < 18.5$ in the other three datasets (used for the density profile shown in black in Figure A.4). The red lines delineate the annuli and sub-sectors used to construct the density profile.

centered on a first-guess value (tipically, the center quoted in the literature). We always adopt different values for the magnitude-cut and radius r, both to check the occurrence of possible dependencies of the result on these assumptions, and to estimate the uncertainty on the final position of $C_{\rm grav}$. As discussed in Miocchi et al. (2013), the adopted values of r always exceed the core radius (r_c) quoted in

the literature, to guarantee that the averaging procedure acts in a region where the density profile decreases with radius, i.e., is no more uniform (as it is, instead, in the innermost region). Taking into account that the literature values of r_c vary from $\sim 5''$ to $\sim 8''$ (see Table 2), we adopted $r = 15''$, $20''$, $30''$. As magnitude-cuts, we used reddening corrected $I_{814,0} < 18, 18.2, 18.5$, thus selecting approximately equal-mass samples, since the difference in mass between the stars at the main-sequence turnoff level and those in evolved evolutionary phases is quite small (within a few 0.01 $M_\odot$). For every pair of magnitude-cut and r values, $C_{\rm grav}$ has been determined iteratively starting from the center quoted in the Harris (1996, 2010 edition) catalog and assuming that convergence is reached when ten consecutive iterations yield values of the cluster center that differ by less than $0.01''$ among them. As gravitational center of NGC 6440, we finally adopted the average of the values of $C_{\rm grav}$ obtained from this procedure, namely: $\alpha = 17^{\rm h}48^{\rm m}52.84^{\rm s}$ and $\delta = -20^\circ 21' 37.5''$, with an uncertainty of $\sim 0.3''$. This is $\sim 2''$ east and $\sim 0.6''$ south from the center quoted in the Harris (1996) catalog. Such a difference can have a non negligible impact on the derived shape of the star density profile and, more in general, on the study of the radial behavior of any stellar population within the cluster potential well.

Star count density profile

In order to build the projected star density profile, $\Sigma_*(r)$, along the entire cluster radial extension, we combined the available photometric data-sets as follows: the *HST-noPM catalog* covers the innermost cluster regions ($\leqslant 115''$), the *FORS2 catalog*, where the center remains unresolved because of stellar crowding, is used to sample the intermediate regions ($115'' < r \leqslant 200''$), and the *Pan-STARRS catalog* refers to the outermost cluster regions ($200'' < r \leqslant 700''$). We considered only stars brighter than $I_{814} < 18.5$ (i.e., ~ 2 mag above the main-sequence turnoff; black dots in the top-right and bottom panels of Figure A.1 and in Figure A.2), because this limit ensures comparable levels of (high) photometric completeness, in combination with high enough statistics (thousands of stars) in all the catalogs. Following the standard procedure already adopted in several previous works (see Lanzoni et al., 2019 and references therein), we divided each photometric sample in several concentric annuli centered on $C_{\rm grav}$ (see Figure A.1), and split each annulus into an adequate number of sub-sectors (typically four). The number of stars lying in each sub-sector was counted, and the star surface density was obtained by dividing these values by the corresponding sub-sector area. The stellar density in each annulus was then obtained as the average of the sub-sector densities, and the standard deviation was adopted as the uncertainty.

The observed stellar density profile is shown in Figure A.4 (upper panel), where different symbols refer to different catalogs (empty circles for HST, triangles for FORS2 and squares for Pan-STARRS) and the radius associated with each annulus

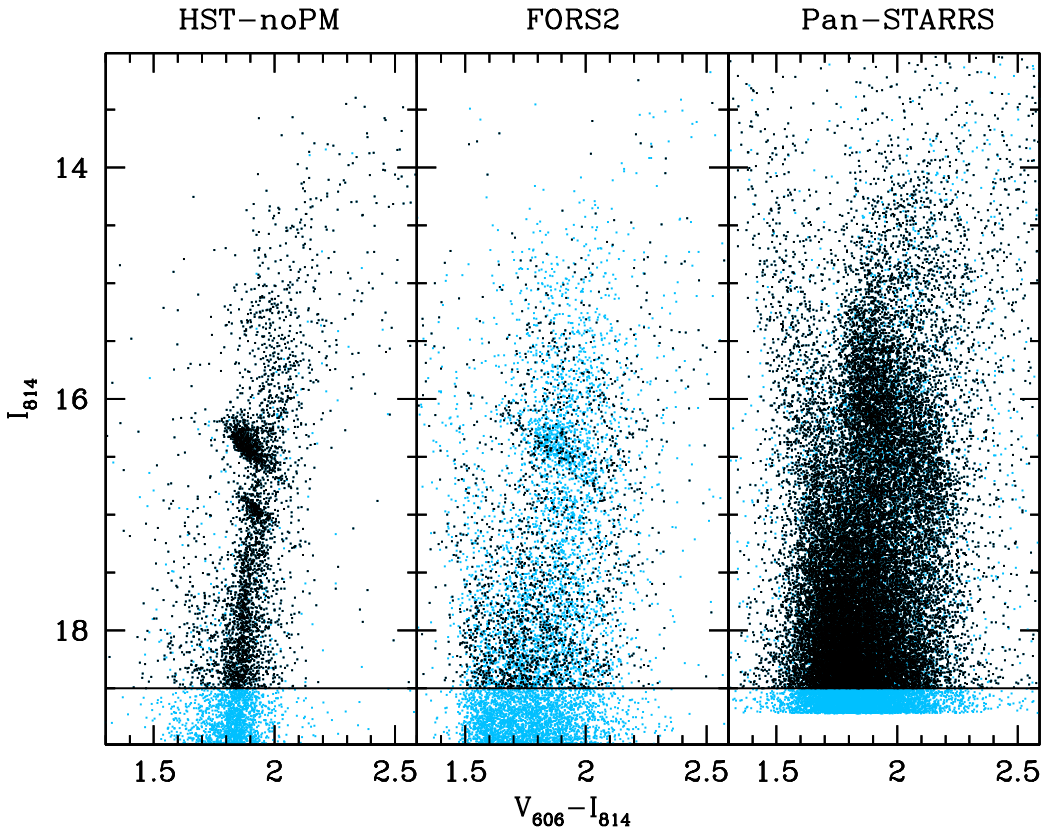

Figure A.2: CMDs of NGC 6440 obtained from the *HST-noPM*, *FORS2* and *Pan-STARRS* catalogs discussed in the text (left, central, and right panel, respectively). The entire samples of surveyed stars are plotted in light blue, while the black dots highlight the stars used for the construction of the density profile.

is the midpoint of the radial bin. As can be seen, the contribution of the Galactic field starts to be evident for distances from the cluster center larger than $r > 100''$ (i.e. in the FORS2 data-set) and becomes dominant for $r > 200''$ (Pan-STARRS catalog). As expected, the spatial distribution of field stars is approximately uniform on the considered radial scale, thus producing a well defined plateau in the outermost portion of the density profile. Hence, the level of Galactic field contamination has been estimated by averaging the data-points aligned in the plateau (see the dashed line in Figure A.4) and the (decontaminated) cluster profile, obtained after subtraction of the Galaxy background level, is finally shown in Figure A.4 (top panel; filled symbols). As apparent, after the field subtraction, the profile remains almost unchanged at small radii, which are in fact dominated by the cluster population, while it significantly decreases in the most external regions, where it turns

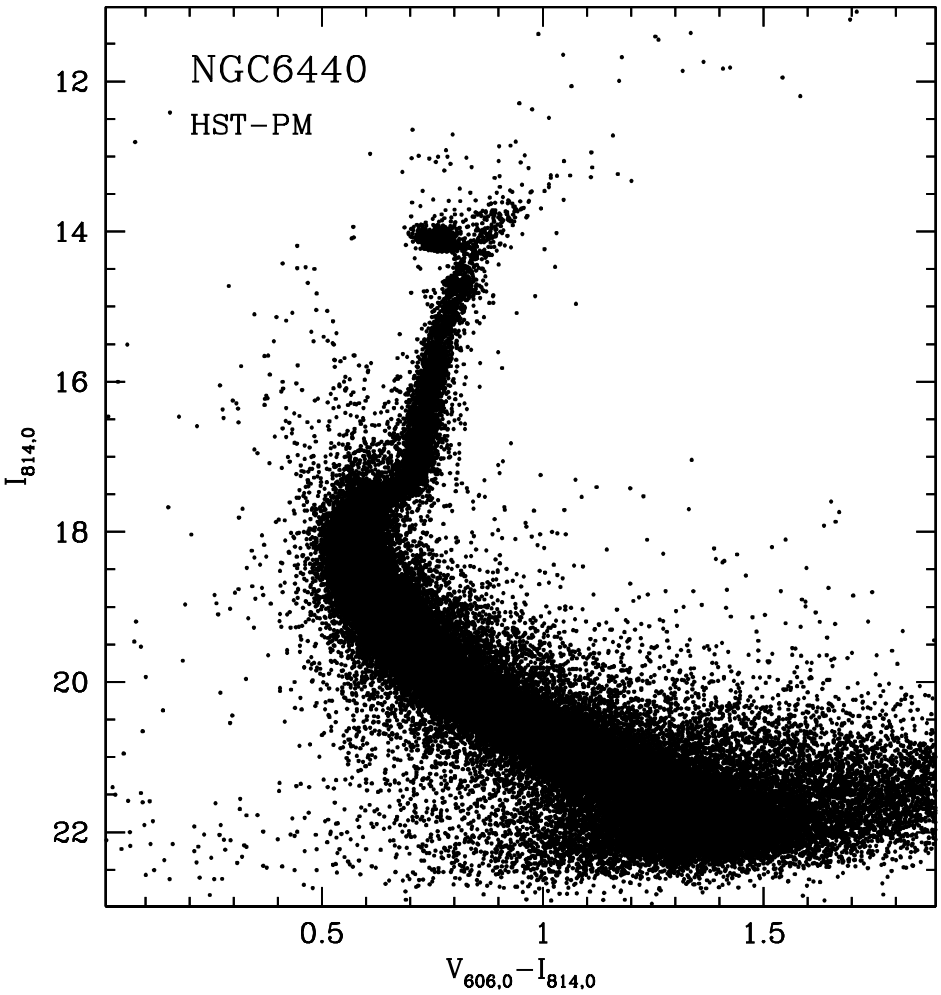

Figure A.3: CMD of NGC 6440 from the *HST-PM* catalog. Only high-quality stars are plotted. Non-member stars (as determined from the proper motion analysis) have been removed. The magnitudes are corrected for the effect of reddening (Pallanca et al., 2019).

out to be significantly below the Galactic background. This clearly indicates that an accurate measure of the field level is crucial for the reliable determination of the outermost portion of the density profile.

The background subtraction has a well-perceivable effect also in the region sampled by HST data. We thus took advantage of the *HST-PM* catalog, which is already cleaned from Galactic field interlopers, to double check the reliability of the adopted decontamination procedure. Thanks to the high level of completeness of the HST

Table A.2: Identity card of NGC 6440: new determinations of its basic parameters.

Parameter	Estimated value
Center of gravity	$\alpha_{\rm J2000} = 17^{\rm h}48^{\rm m}52.84^{\rm s}$
	$\delta_{\rm J2000} = -20^\circ21\prime37.5\prime\prime$
Reddening law	$R_V = 2.7$
Color excess	$E(B-V) = 1.26 - 1.28$
Distance modulus	$\mu_0 = 14.6 \pm 0.1$
Distance	$d = 8.3 \pm 0.4$ kpc
Age	$t = 13 \pm 1.5$ Gyr
RGB bump	$M_{\rm V_{606}}^{Bump} = 1.12 \pm 0.12$
	$M_J^{Bump} = -0.37 \pm 0.12$
	$M_K^{Bump} = -0.94 \pm 0.12$
Dimensionless central potential	$W_0 = 8.10^{0.20}_{-0.20}$
Concentration parameter	$c = 1.86^{0.06}_{-0.06}$
Core radius	$r_c = 6.4^{0.3}_{-0.3}$ arcsec $= 0.26^{0.01}_{-0.01}$ pc
Half-mass radius	$r_h = 50.2^{5.2}_{-4.5}$ arcsec $= 2.02^{0.21}_{-0.18}$ pc
Effective radius	$r_e = 36.8^{3.7}_{-3.2}$ arcsec $= 1.48^{0.15}_{-0.13}$ pc
Truncation radius	$r_t = 481.4^{43.9}_{-42.3}$ arcsec $= 19.4^{1.8}_{-1.7}$ pc
Central relaxation time	$\log(t_{rc}/{\rm yr}) = 7.4$
Half-mass relaxation time	$\log(t_{rh}/{\rm yr}) = 9.0$

observations, we constructed the cluster density profile by using stars down to the sub-giant branch (i.e., 0.5 magnitudes deeper than the sample used in the previous procedure; black dots in the top-left panel of Figure A.1), thus benefitting from a much larger statistics. Figure A.4 (bottom panel) shows the density profile obtained from the *HST-PM* catalog (in red), vertically shifted to match the one obtained with the procedure described above (in blue): as can be seen, the two profiles are essentially identical in the common region, thus confirming the solidity of the adopted field decontamination approach.

In order to derive the physical parameters of the program cluster, we fit the observed star density profile with the family of King (1966) models in the isotropic, spherical and single-mass approximation. They constitute a *single*-parameter family, since their shape is uniquely determined by the dimensionless parameter W_0, which is proportional to the gravitational potential at the center of the system, or, alternatively, to the "concentration parameter" c, defined as $c \equiv \log(r_t/r_0)$, where r_t and r_0 are the tidal and the King radii of the cluster, respectively.

The best-fit King model has been determined by exploring a grid of W_0 values varying between 0.4 and 12 in steps of 0.05, and selecting the solution that minimizes the χ^2 residuals between the observed and the theoretical density profiles (see Miocchi et al., 2013 and Lanzoni et al., 2019 for a detailed description of the adopted procedure and the method used to estimate the uncertainties). The resulting values

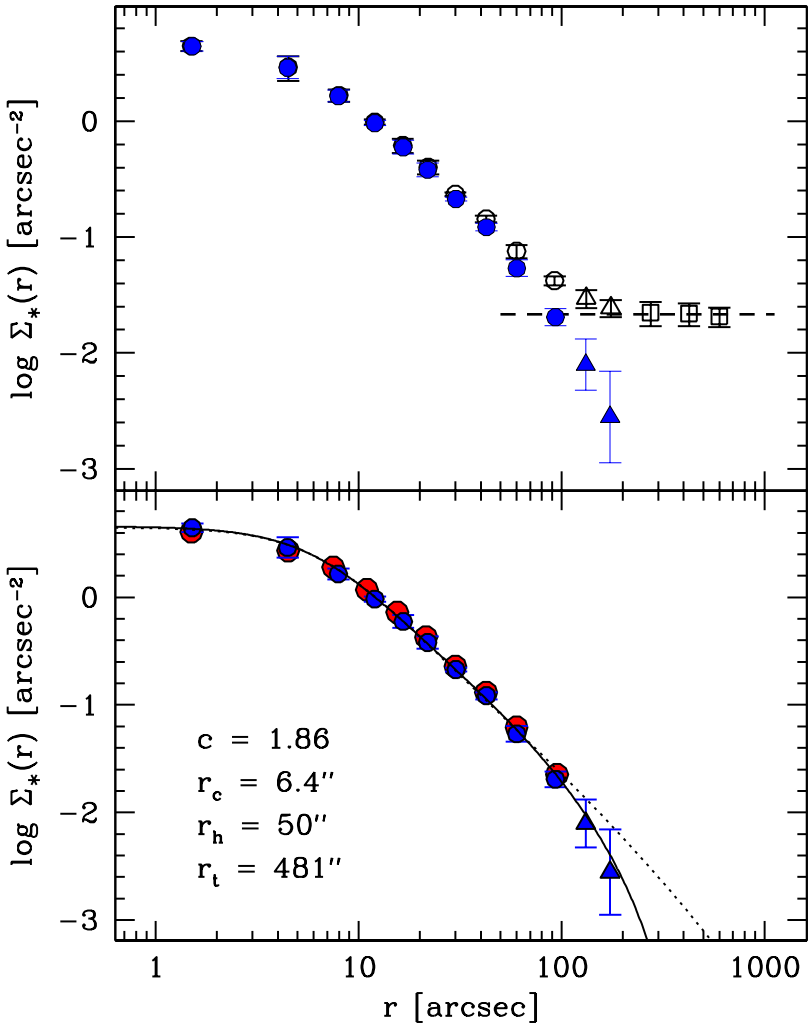

Figure A.4: *Top:* Observed star density profile of NGC 6440 obtained from resolved star counts by combining three different catalogs: *HST-noPM* (empty circles), *FORS2* (empty triangles) and *Pan-STARRS* (empty squares). The filled blue symbols correspond to the cluster density profile obtained after subtraction of the Galaxy field contribution (dashed line). *Bottom:* Cluster density profile shown in the top panel (blue symbols) compared to that obtained from the *HST-PM* catalog (red circles). As can be seen the agreement is very good, thus guaranteeing the reliability of the applied background subtraction (see text). The black line shows the best-fit King model profile. The corresponding values of the concentration parameter (c) and a few characteristic scale-lengths (in arcseconds) are also labelled. The dotted line shows the best-fit Wilson model.

of W_0, concentration parameter, core, half-mass and tidal radii are: $W_0 = 8.10$, $c = 1.86$, $r_c = 6.4''$, $r_h = 50.2''$, $r_t = 481.4''$, respectively, with the uncertainties quoted in Table A.2. The effective radius, defined as the radial distance including half the total number counts in projection (and corresponding to the projected half-light radius if SB, instead of resolved star density, is considered) is $r_e = 36.8''$. The comparison with previous determinations in the literature shows significant discrepancies for all the parameters. In particular, the Harris catalog reports the values estimated by McLaughlin & van der Marel (2005), who found $c = 1.62$, $r_c = 8.1''$, $r_h = 44.8''$, $r_{\rm eff} = 28.8''$, and $r_t = 354.9''$ (the values originally quoted in pc have been converted into arcseconds by using the cluster distance provided in that paper: $d = 8.4$ kpc). Hence, we find that NGC 6440 is more centrally concentrated than previously thought, with a smaller core radius and larger truncation radius, translating in a larger concentration parameter. The comparison with the values quoted by Baumgardt & Hilker (2018) is less straightforward because N-body simulations, instead of King models, are used there to fit the observation, and no uncertainties are provided. However, the provided values of core, half-mass and effective radii are consistent with ours within 10-20%. We also stress that SB (instead of number count) profiles and an offset position of the cluster centre are used in those studies, thus likely accounting for the different results. The density profile of some GCs is found to be best reproduced by Wilson (1975), instead of King (1966), models (see, e.g., McLaughlin & van der Marel, 2005; Miocchi et al., 2013). We thus compared the observations also with the Wilson (1975) model family, finding the best solution for $c = 3.30$, $r_c = 6.6''$ and $r_t \sim 230'$ (see the dotted line in the bottom panel Figure A.4). Although the core radius is very similar to that obtained from the King fit, the Wilson model (that, by construction, provides a smoother cutoff at the limiting radius) severely overestimate the observed stellar density in the external portion of the profile. This is in agreement with the fact that NGC 6440 is orbiting the Bulge of our galaxy, where tidal truncation is expected to be more relevant than for faraway halo GCs.

The distance modulus and the age of NGC 6440

The distance modulus and the age of resolved stellar populations (as Galactic GCs) can be estimated through the comparison between the observed CMD and theoretical stellar isochrones, the main obstacle being the well known degeneracy of these parameters with the metallicity and the reddening.

In the case of NGC 6440, the metallicity is relatively well known since the first low-resolution spectroscopic measures (see Armandroff & Zinn 1988; Origlia et al. 1997; Frogel et al. 2001), indicating an overall iron abundance of the order of 1/3 - half solar. More recent high-resolution spectroscopy of small samples of giants measured in the IR (Origlia et al., 2008b) and in the optical band (Muñoz et al., 2017) confirmed a considerable iron content ([Fe/H]$= -0.5, -0.6$) with some $\alpha-$enhancement

($[\alpha/Fe] = +0.3$), corresponding to a global metallicity[2] [M/H]~ -0.4.

The accurate estimate of the reddening, instead, is complicated by the fact that NGC 6440 is located close to the Galactic plane and toward the bulge, where the extinction law likely deviates from the canonical and commonly assumed behavior. An extensive discussion about extinction and reddening is presented in McCall (2004). Particular attention, however, has to be given to the extinction toward the inner Galaxy, where the R_V value is not constant and can significantly vary along different directions (e.g., Popowski, 2000; Udalski, 2003; Nataf et al., 2013b; Alonso-García et al., 2017, and references therein). Indeed, as discussed in Nataf et al. (2013b); Casagrande & VandenBerg (2014), and recently confirmed by Ferraro et al. (2021) and C. Pallanca et al. (2021, in preparation), the region toward the Galactic center seems to be better described by an extinction law with a significantly smaller value of R_V (even down to $R_V = 2.5$). Conversely some other authors found larger R_V values ($R_V = 3.2$) to be more appropriate (e.g., Bica et al., 2016; Kerber et al., 2019). Hence, as already discussed by Udalski (2003), the proper dereddening of a particular field in the Galactic bulge might be difficult without prior determination of R_V along its line of sight.

The best way to constrain R_V in a specific direction is by simultaneously investigating the IR and the optical CMDs, which are, respectively, weakly and strongly sensitive to the true extinction law. To this purpose we used a combination of optical and IR catalogs of NGC 6440.

The adopted HST optical catalog was presented in Pallanca et al. (2019), while the IR one is based on deep J and K_s observations obtained with GeMS/GSAOI (S. Saracino et al., 2021, in preparation). For a proper comparison with stellar isochrones, we first corrected the CMDs obtained from these catalogs for the effect of differential reddening, which broadens and distorts the evolutionary sequences. To this end, we applied the procedure fully described in Pallanca et al. (2019) to the HST dataset. Briefly, we determined the reference mean ridge line of NGC 6440 using a sample of well-measured stars. Then, for every star in the HST catalog we selected a sample of close sources, thus defining a "local-CDM". Finally, we estimated the value δE(B-V) necessary to superpose the reference mean ridge line onto the local-CMD and assigned this value to the corresponding investigated star. By construction, the δE(B-V) values thus obtained express the differential component of the reddening within the sampled FOV and can be positive or negative. This quantity, multiplied by the coefficient appropriate for the considered filter, is added to the observed magnitudes to get differential reddening corrected (DRC) magnitudes: $I_{814,DRC}$, $V_{606,DRC}$ (see Figure A.5). Finally, for all the stars in common with the GeMS/GSAOI sample, the estimated values of δE(B-V) have been used to correct also the IR magnitudes and build the corresponding differential reddening corrected

[2]The global metallicity has been calculated trough the relation reported by Ferraro et al. (1999a) and assuming $[Fe/H] = -0.56$ (Origlia et al., 2008b)

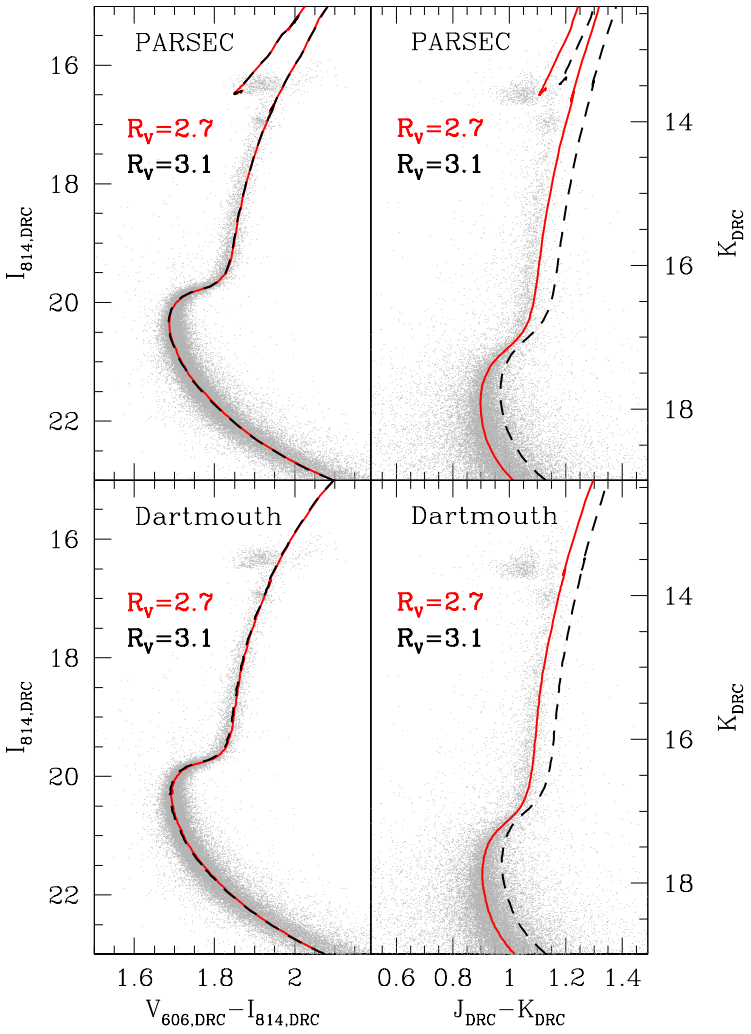

Figure A.5: Comparison between the differential-reddening corrected CMD of NGC 6440 (grey dots) and theoretical isochrones computed for $R_V = 3.1$ (black dashed lines) and for $R_V = 2.7$ (red lines). The left and right panels show, respectively, the optical and the IR CMDs. The top panels refer to PARSEC isochrones, while the bottom panels show Dartmouth models. No solution able to properly fit the optical and the IR CMDs simultaneously is found for $R_V = 3.1$, while if $R_V = 2.7$ is assumed, both models well reproduce the observations for an age of 13 Gyr, a distance modulus of 14.60 and $E(B-V) = 1.26$-1.28. The fact that the RGB looks steeper than the model in the IR CMDs may be due to nonlinearity effects of the GeMS/GSAOI photometry (see Saracino et al., 2016).

CMD: K_{DRC}, $(J\text{-}K)_{DRC}$ (Figure A.5).

To estimate the distance modulus and the age of NGC 6440, while constraing R_V, we then compared the differential reddening corrected CMDs with a set of PARSEC (Bressan et al., 2012) and Dartmouth (Dotter et al., 2008) isochrones of different ages computed for [M/H]= -0.4 in the four photometric bands of interest, namely, the WFC3 V_{606} ad I_{814} filters, and the 2MASS J and Ks filters. To place the isochrones in the differential reddening corrected CMDs, we determined the values of the (temperature- and gravity-dependent) extinction coefficients in the four bands (namely, $R_{V_{606},i}$, $R_{I_{814},i}$, $R_{J,i}$ and $R_{Ks,i}$) for each i^{th} combination of effective temperature and surface gravity along every isochrone (Casagrande & VandenBerg, 2014). This has been done by interpolating the values calculated for the MARCS grid (Gustafsson et al., 2008) under the assumption of the cluster metallicity and the Cardelli et al. (1989) extinction law with $R_V = 2.5$ and $R_V = 3.1$. A linear interpolation between these two limits then allowed us to determine the temperature- and gravity-dependent coefficients for intermediate values of R_V (between 2.5 and 3.1, stepped by 0.1).

We found that, under the assumption of $R_V = 3.1$, no combination of parameters is able to reproduce the optical and the IR CMDs simultaneously. In particular, a combination that well fits the optical CMD corresponds to an excessively bright and red isochrone in the IR, for both the considered models (see the black dashed lines in Figure A.5). The problem becomes progressively milder for decreasing values of R_V, and the best solution is found for $R_V = 2.7$. Interestingly, similarly small values are needed to properly reproduce the observations of other GCs in the Galactic bulge (Ferraro et al., 2021, see also Pallanca et al. 2021, in preparation). The red lines shown in Figure A.5 correspond to PARSEC and Dartmouth isochrones (upper and lower panels, respectively) computed under the assumption of $R_V = 2.7$, for an age of 13 Gyr, a distance modulus $\mu_0 = 14.60$ and an absolute color excess that is just slightly different between the two models: $E(B-V) = 1.28$ and 1.26, respectively. In particular, this combination of parameters not only well reproduces the horizontal branch magnitude level (see the PARSEC isochrones in the figure), but also best-fits the SGB/MS-TO region, which is the most sensitive to age variations. The best-fit solution has been evaluated through a χ^2 analysis, by determining, for each SGB/MS-TO star, the difference between its observed color and the color at the same magnitude level along the isochrones of 11, 12, 13 and 14 Gyr. As already done in previous works (Ferraro et al., 2021; see also Saracino et al., 2016) the χ^2 parameter has been computed as the ratio between the square of this difference and the color along the isochrone, summed over all the selected stars. The best-fit model to the optical CMD and the χ^2 values as a function of the investigated ages are plotted, respectively, in the top and bottom panels of Figure A.6. Taking into account the various uncertainties and degeneracies entering the fitting procedures, conservative estimates of the errors on the distance modulus and age are 0.1 mag and 1.5 Gyr, respectively.

Several previous works in the literature have been devoted to the determination of

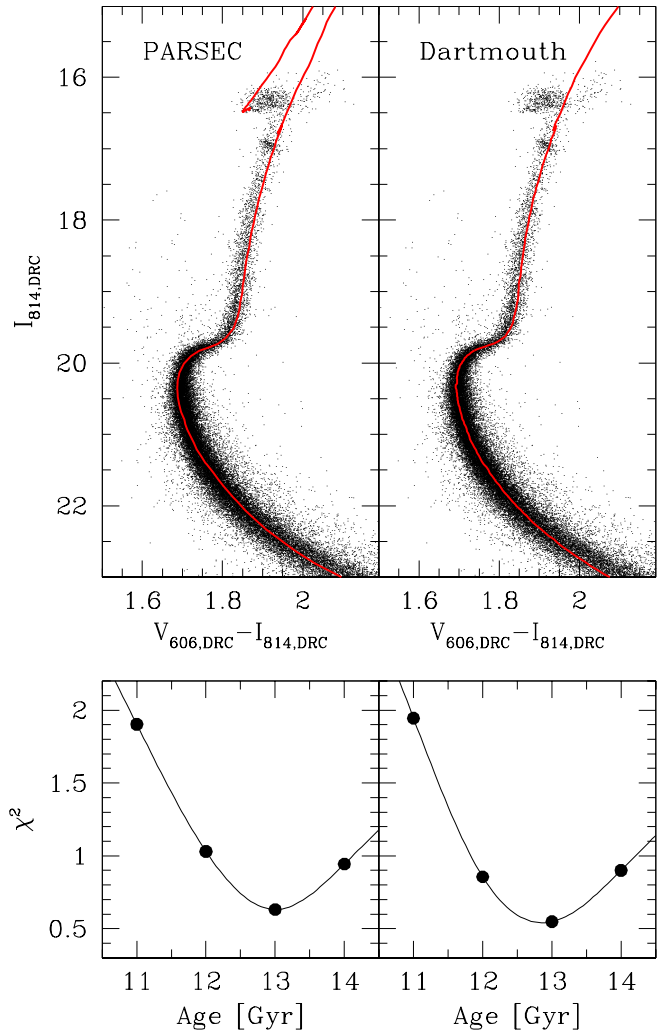

Figure A.6: *Top panels:* differential-reddening corrected CMD of NGC 6440 with the best-fit isochrone from the PARSEC (left) and the Dartmouth (right) models superimposed as red lines (the same as in Figure A.5). *Bottom panels:* value of the χ^2 parameter (see text) obtained from the fit of the SGB/MS-TO region through PARSEC (left) and Dartmouth (right) isochrones of 11, 12, 13, and 14 Gyr, as a function of the model age. The minimum of the χ^2 parameter is found for an age of 13 Gyr.

these parameters for NGC 6440. The study by Ortolani et al. (1994) is based on optical photometry, while the others have been performed in the IR, and in all cases the standard reddening law has been assumed. The only exception is the investigation of Kuchinski & Frogel (1995), who combined IR data with V band photometry and suggested that the anomalous colors observed for this cluster might require

a non-standard reddening law. This is in agreement with our finding, although a detailed comparison between the proposed reddening laws in not obvious. Given the different R_V adoption, the comparison among various reddening determinations in the literature has to be done in terms of the extinction coefficient A_V, instead of the color excess E(B-V), which is linked to the former by the following relation: $A_V = R_V \times$ E(B-V). Minniti (1995) quote E(J-K)=0.57 and comment that this value is in good agreement with that of Ortolani et al. (1994), who found E(B-V)=1 and adopt $R_V = 3$, corresponding to $A_V = 3$. Valenti et al. (2004a) quote E(B-V)=1.15 and adopt $R_V = 3.1$, thus providing $A_V = 3.56$. From the Harris compilation, $A_V = 3.32$ is obtained for the standard value of R_V. The value estimated in the present study ($A_V = 2.7 \times 1.27 = 3.43$) therefore is within the range spanned by the results of previous works, which however do not correct for differential reddening, nor take into account the optical and IR CMDs simultaneously. Also the distance modulus here determined is in reasonable agreement with previous determinations and included between them: $\mu_0 = 14.64$ and 14.58 in Ortolani et al. (1994) and Valenti et al. (2004a), respectively. Finally, an age of 11^{+3}_{-2} Gyr was estimated by Origlia et al. (2008a) from pioneering adaptive optics photometry, and 13 Gyr is the value adopted by Muñoz et al. (2017) to fit the observed CMD with theoretical isochrones. These are both consistent with our determination of 13 ± 1.5 Gyr.

The RGB-bump

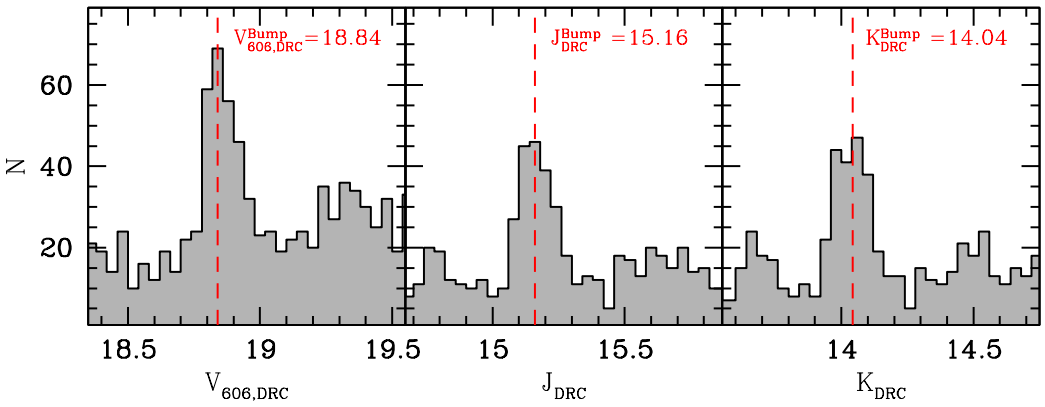

Figure A.7: Differential luminosity function of RGB stars classified as cluster members and photometrically well measured. The detected peaks (marked by the dashed red lines) correspond to the RGB-bump magnitude in the three photometric bands (see labels).

The high-quality of the CMDs presented in this work allows us to easily identify a well known evolutionary feature along the RGB: the so-called RGB bump. This feature appears in the CMD as a well defined clump of stars along the RGB. This

evolutionary feature flags the moment when the H-burning shell reaches the H discontinuity left by the inner penetration of the convective envelope (see the seminal works by Fusi Pecci et al. 1990, Ferraro et al. 1991, 1992b,a and Ferraro et al. 1999a, 2000; see also the compilation by Zoccali et al. 1999, Riello et al. 2003 and Valenti et al. 2004b, and more recently by Nataf et al. 2013a). Figure A.7 shows the differential luminosity function of the bright RGB stars in the differentially-corrected V_{606}, J, K bands. The well-defined peaks at $V_{606,DRC} = 18.84 \pm 0.05$, $J_{DRC} = 15.16 \pm 0.05$, $K_{DRC} = 14.04 \pm 0.05$ correspond to the RGB bump. Adopting the extinction and the distance reported in Table A.2, we transformed the above values into absolute magnitudes obtaining $M^{Bump}_{V_{606}} = 1.12 \pm 0.12$, $M^{Bump}_{J} = -0.37 \pm 0.12$ and $M^{Bump}_{K} = -0.94 \pm 0.12$. In Figure A.8 we show the comparison among these measures and previous determinations in the literature. In particular in the bottom and central panels of Figure A.8 we show the nice agreement of the RGB bump magnitude in the IR bands with the estimates and the relations quoted in Valenti et al. (2004b). The situation appears to be much more complex in the optical V_{606} band, since the magnitude level found in the present study appears significantly brighter than that obtained by Nataf et al. (2013a), who quote $M^{Bump}_{V_{606}} = 1.48$. While the adopted extinction law and distance modulus are just slightly different between the two studies, most of the discrepancy is due to the observed RGB bump magnitude: $V_{606} = 19.431 \pm 0.021$ in Nataf et al. (2013a), $V_{606} = 18.9$ in our study. In addition, a metallicity as high as [M/H]=+0.03 has been assumed in that work.

Nevertheless, we note that the new determination of the RGB bump combined with the adopted metallicity well follows the trend of the GC distribution reported by Nataf et al. (2013a).

SUMMARY AND CONCLUSIONS

This work provides updated values for the structural parameters and age of NGC 6440, a GC in the direction of the Galactic bulge that is relatively poorly investigated because of the strong and differential extinction along its line of sight. To our knowledge, these are the first determinations of the center and density profile of NGC 6440 based on resolved star counts, which are free from biases induced by the possible presence of few bright objects. The gravitational center of the cluster has been determined from the observed positions of PM-selected member stars, and it turns out to be significantly off (by $\sim 2''$ in right ascension) with respect to the value quoted in the literature (Harris, 1996), reporting the SB peak estimated by Picard & Johnston (1995). By making use of a suitable combination of high-resolution (HST) photometry and wide-field data (FORS2 observations and a Pan-STARRS catalogue), we then built the most radially extended surface density profile so far from resolved star counts. With respect to the work of McLaughlin & van der Marel (2005, see also the Harris catalog), which is based on the previous estimate of the cluster center and uses the SB distribution instead of number counts, the best-fit

King model to the projected density profile derived in this work reveals that NGC 6440 has a significantly larger concentration parameter, a smaller core radius, and a larger overall extension (truncation radius) on the plane of the sky. The updated values of the cluster center and structural parameters are listed in Table A.2.

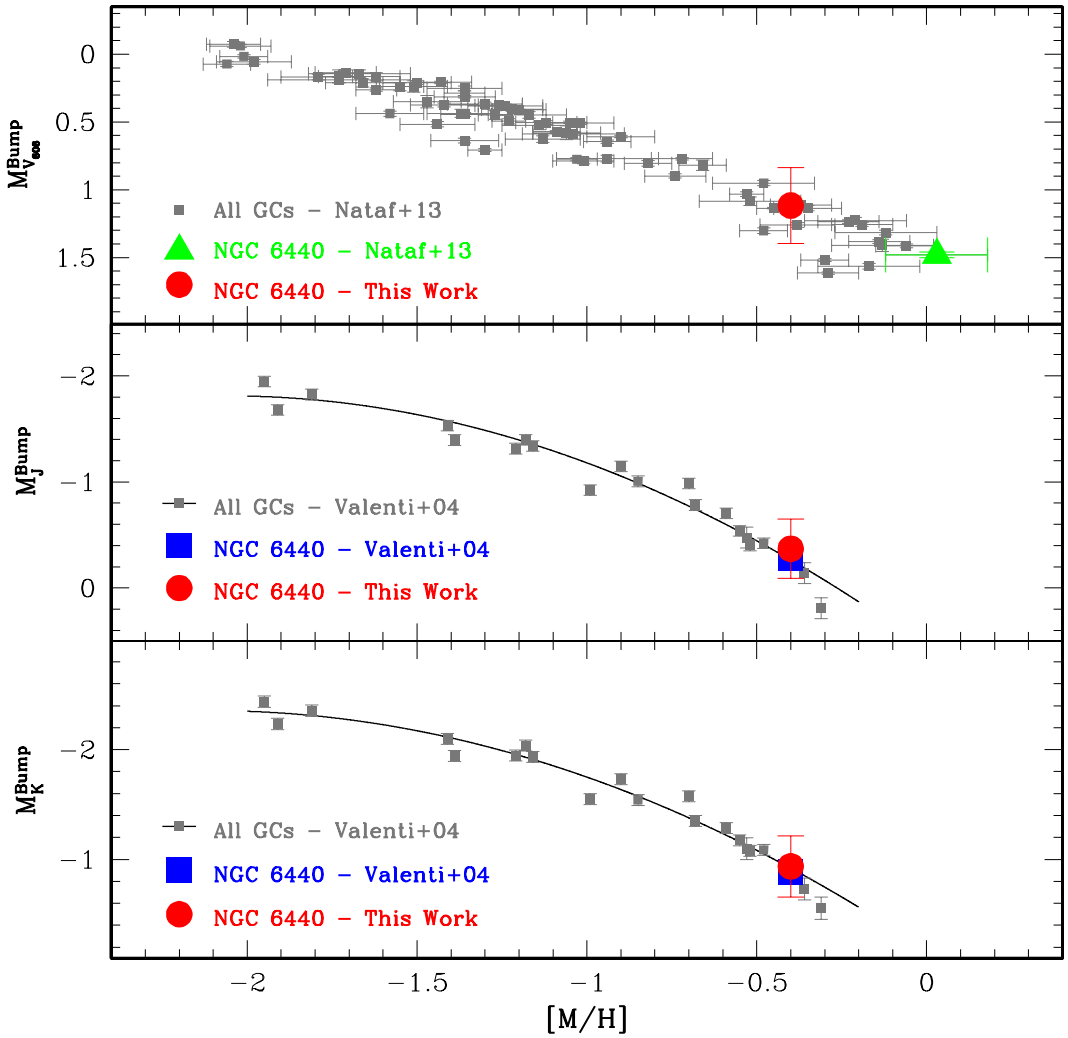

Figure A.8: Absolute magnitude of the RGB-bump in the V_{606}, J and K bands (from top to bottom) as a function of the GC global metallicity [M/H]. The gray symbols are from the literature (see labels). The blue squares and the green triangle mark the location of NGC 6440 according to literature (Nataf et al., 2013a; Valenti et al., 2004b) while the red circle mark the values determined in this work.

By taking advantage of the PM selection, we built a sample of cluster member stars with both optical (HST) and IR (GeMS/GSAOI) magnitudes, that we properly corrected for the effect of differential reddening. We then used stellar isochrones,

from both the PARSEC (Bressan et al., 2012) and the Dartmouth (Dotter et al., 2008) models, to simultaneously reproduce the optical and the IR CMDs (which are strongly and weakly dependent on reddening, respectively). Adopting extinction coefficients that depend on the stellar surface temperature and gravity, we explored extinction laws with R_V ranging from 2.5 to 3.1, and we found that $R_V = 2.7$ is required to fit both to the optical and the IR CMDs. This confirms (see also Popowski, 2000; Nataf et al., 2013b; Casagrande & VandenBerg, 2014) that the extinction law in Galactic regions close to the plane and in the direction of the bulge requires an R_V value significantly different from the "canonical" 3.1. The best-fit to the CMDs (in particular to the horizontal branch level, and the SGB/MS-TO region that strongly depends on the age of the stellar population) provided us also with the cluster age ($t = 13 \pm 1.5$ Gyr), distance modulus ($\mu_0 = 14.60 \pm 0.1$, corresponding to a distance of 8.3 kpc, with a conservative uncertainty of ~ 0.4 kpc), and absolute color excess, $E(B-V) = 1.26 - 1.28$, which corresponds to a V-band extiction coefficient $A_V = 3.34$. These values are all within the ranges spanned by previous determinations in the literature (see Section A). In particular, the age estimate here obtained for NGC 6440 is the most accurate so far (although the uncertainty is still quite large: 1.5 Gyr). Figure 9 shows the age-metallicity distribution for the bulge GCs with available age estimate, where NGC 6440 is marked as a large red square. The data for the other clusters are mainly from Saracino et al. (2019, see their Figure 16) and Oliveira et al. (2020, see their Figure 12) with the addition of the recent age determination of NGC 6256 (Cadelano et al., 2020). We also mark the age-metallicity of the oldest stellar population in the two Bulge Fossil Fragments (BFF; namely Terzan5 and Liller1) so far discovered into the bulge (Ferraro et al., 2009b, 2016, 2021). The BFFs (Ferraro et al., 2009b, 2016; Origlia et al., 2011; Massari et al., 2014) are systems that, in spite of their appearance as genuine GCs, host multi-age stellar populations and could be the remnants of massive clumps that contributed to form the bulge at the epoch of the Galaxy assembly. As apparent, these systems all have old ages, well consistent with those of the majority of bulge GCs and Galactic field stars observed in different directions toward the bulge (e.g., Zoccali et al., 2003; Clarkson et al., 2011; Valenti et al., 2013). The weighted mean age of the entire sample (now including a total of 18 GCs and 2 BFFs) is 12.7 ± 0.2 Gyr, which is ~ 0.5 Gyr older than the value quoted in Saracino et al. (2019) on the basis of a sub-sample of 14 objects.

The superb quality of the obtained CMDs allows an accurate determination of the RGB-bump. This value, combined with the spectroscopic estimate of the cluster metallicity, makes NGC 6440 to perfectly fit into the bump-metallicity relation defined by Galactic GCs.

The new determinations of the cluster structural parameters, distance and reddening allow us to also update the value of relaxation time of NGC 6440, which characterizes the dynamical evolutionary stage of the system. It quantifies the timescale needed by two-body interactions (causing kinetic-energy exchanges among stars) to

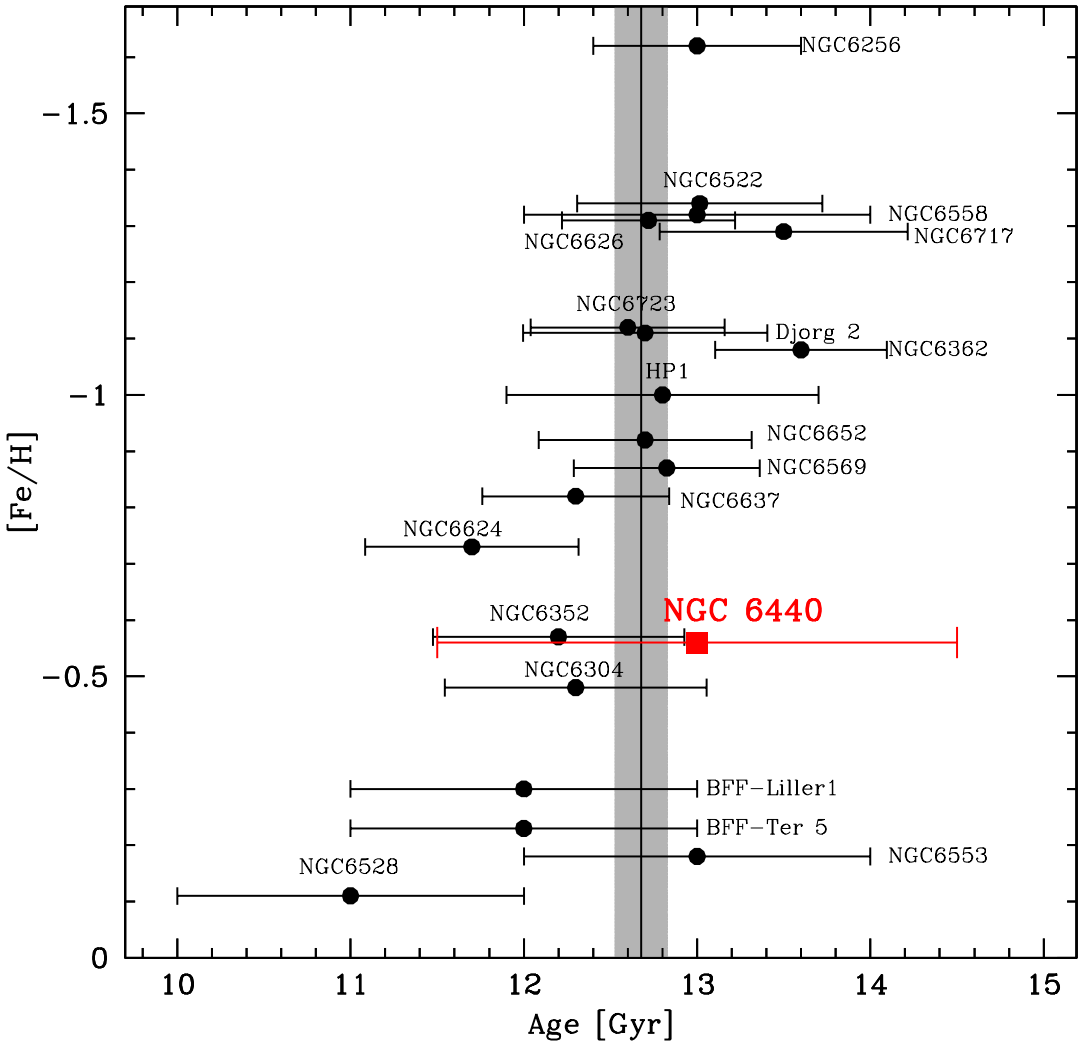

Figure A.9: Age-metallicity distribution for the bulge GCs with age estimate available. NGC 6440 is marked as a large red square. Data for the other clusters are mainly from Saracino et al. (2019, see their Figure 16) and Oliveira et al. (2020, see their Figure 12) with the addition of the recent age determination of NGC 6256 (Cadelano et al., 2020). We also plotted the age-metallicity of the oldest stellar population in the two Bulge Fossil Fragments (BFF; namely Terzan5 and Liller1) so far discovered into the bulge (Ferraro et al., 2009b, 2016, 2021). The grey vertical strip marks the weighted average and 1σ uncertainty (12.7 ± 0.2 Gyr) of the entire sample.

bring the cluster toward a thermodynamically relaxed state. This quantity has been used to validate the so-called A^+ parameter, quantifying the level of central segregation of blue straggler stars within a GC (Alessandrini et al., 2016), as a powerful

empirical diagnostic of the dynamical age of the host system (e.g., Ferraro et al., 2018a, 2019; Lanzoni et al., 2016; Ferraro et al., 2020). Primarily depending on the local density, the value of the relaxation time changes with the radial distance from the cluster center. To estimate the central relaxation time (t_{rc}) we used equation (10) of Djorgovski (1993). For the half-mass relaxation time (t_{rh}) we followed equation (8-72) of Binney & Tremaine (1987). The latter parameter can be estimated also from eq. (11) of Djorgovski (1993) once the first coefficient (8.993×10^5 in the equation) is substituted by its proper value (2.055×10^6; see Binney & Tremaine, 1987; McLaughlin & van der Marel, 2005). We also emphasize that the projected half-light radius r_e (instead of the three-dimensional half-mass radius r_h) is often used in this estimate (see, e.g., Harris, 1996; McLaughlin & van der Marel, 2005), under the implicit assumption that these radial scales are equal. However, depending on the value of the concentration paramenter, the ratio between the effective and the half-mass radii varies between 0.73 and 0.76. As a consequence, since t_{rh} scales with half-mass radius at the power of 3/2, the relaxation time obtained by adopting r_e (t_{re}) is $\sim 35\%$ shorter than that calculated by using r_h. Assuming the absolute $V-$band magnitude and central SB quoted for NGC 6440 in the Harris (1996) catalog, and the same values adopted there for the average stellar mass ($0.3 M_\odot$) and V-band mass-to-light ratio ($M/L_V = 2$), the new determinations of the structural parameters, distance, and extinction quoted in Table A.2 bring to $\log(t_{rc}) = 7.4$ and $\log(t_{rh}) = 9.0$ (in units of year). If the effective radius is used in place of r_h (as it is done, e.g., in the Harris catalog and in McLaughlin & van der Marel, 2005), the relaxation time becomes smaller than 1 Gyr: we find $\log(t_{re}) = 8.8$, which is 37% shorter than t_{rh}. For comparison, the central relaxation time quoted in the Harris (1996) catalog is $\log(t_{rc}) = 7.6$, i.e., a factor of ~ 1.6 longer than our determination, and the median relaxation time (8.62 in logarithimic units) is a factor of ~ 1.5 shorter than our value of t_{re}, mainly reflecting the scale-length differences discussed above, while the assumption of different extinction law and color excess has a negligible impact on the result. These values suggest that NGC 6440 is in a dynamically evolved stage (its age being much longer than the relaxation times), although the A^+ parameter has not been determined yet for this system, because a safe selection of its blue straggler population has been hampered so far by the large contamination from Galactic field stars and the severe and differential reddening conditions along its line of sight.

Bibliography

Aarseth, S. J. 2003, Gravitational N-Body Simulations

—. 2012, MNRAS, 422, 841, doi: 10.1111/j.1365-2966.2012.20666.x

Alessandrini, E., Lanzoni, B., Ferraro, F. R., Miocchi, P., & Vesperini, E. 2016, ApJ, 833, 252, doi: 10.3847/1538-4357/833/2/252

Alonso-García, J., Minniti, D., Catelan, M., et al. 2017, ApJ, 849, L13, doi: 10.3847/2041-8213/aa92c310.48550/arXiv.1710.04854

Applegate, J. H. 1986, ApJ, 301, 132, doi: 10.1086/163881

Arca Sedda, M., Askar, A., & Giersz, M. 2018, MNRAS, 479, 4652, doi: 10.1093/mnras/sty1859

Armandroff, T. E., & Zinn, R. 1988, AJ, 96, 92, doi: 10.1086/114792

Askar, A., Arca Sedda, M., & Giersz, M. 2018, MNRAS, 478, 1844, doi: 10.1093/mnras/sty1186

Askar, A., Bianchini, P., de Vita, R., et al. 2017, MNRAS, 464, 3090, doi: 10.1093/mnras/stw2573

Askar, A., Giersz, M., Pych, W., Olech, A., & Hypki, A. 2016, in Star Clusters and Black Holes in Galaxies across Cosmic Time, ed. Y. Meiron, S. Li, F. K. Liu, & R. Spurzem, Vol. 312, 262–263, doi: 10.1017/S1743921315007991

Bahcall, J. N., & Wolf, R. A. 1976, ApJ, 209, 214, doi: 10.1086/154711

Bastian, N., & Lardo, C. 2018, ARA&A, 56, 83, doi: 10.1146/annurev-astro-081817-051839

Baumgardt, H., & Hilker, M. 2018, MNRAS, 478, 1520, doi: 10.1093/mnras/sty105710.48550/arXiv.1804.08359

Baumgardt, H., & Kroupa, P. 2007, MNRAS, 380, 1589, doi: 10.1111/j.1365-2966.2007.12209.x

Baumgardt, H., & Makino, J. 2003, MNRAS, 340, 227, doi: 10.1046/j.1365-8711.2003.06286.x

Baumgardt, H., Makino, J., & Hut, P. 2005, ApJ, 620, 238, doi: 10.1086/426893

Baumgardt, H., & Vasiliev, E. 2021, MNRAS, 505, 5957, doi: 10.1093/mnras/stab1474

Beccari, G., Ferraro, F. R., Dalessandro, E., et al. 2019, ApJ, 876, 87, doi: 10.3847/1538-4357/ab13a4

Belczynski, K., Kalogera, V., & Bulik, T. 2002, ApJ, 572, 407, doi: 10.1086/340304

Bellini, A., Anderson, J., & Bedin, L. R. 2011, PASP, 123, 622, doi: 10.1086/65987810.48550/arXiv.1102.5218

Bettwieser, E., & Sugimoto, D. 1984, MNRAS, 208, 493, doi: 10.1093/mnras/208.3.493

Bhat, B., Lanzoni, B., Ferraro, F. R., & Vesperini, E. 2022, ApJ, 926, 118 (B22)

—. 2023, New Parameters for Star Cluster Dynamics: The Effect of Primordial Binaries and Dark Remnants, doi: 10.3847/1538-4357/acb434

Bhattacharya, D., & van den Heuvel, E. P. J. 1991, Phys. Rep., 203, 1, doi: 10.1016/0370-1573(91)90064-S

Bianchini, P., van de Ven, G., Norris, M. A., Schinnerer, E., & Varri, A. L. 2016, Monthly Notices of the Royal Astronomical Society, 458, 3644, doi: 10.1093/mnras/stw552

Bianchini, P., Webb, J. J., Sills, A., & Vesperini, E. 2018, MNRAS, 475, L96, doi: 10.1093/mnrasl/sly013

Bica, E., Ortolani, S., & Barbuy, B. 2016, PASA, 33, e028, doi: 10.1017/pasa.2015.4710.48550/arXiv.1510.07834

Binney, J., & Tremaine, S. 1987, Galactic dynamics

Boily, C. M., & Kroupa, P. 2003, MNRAS, 338, 673, doi: 10.1046/j.1365-8711.2003.06101.x

Breen, P. G., & Heggie, D. C. 2012, MNRAS, 420, 309, doi: 10.1111/j.1365-2966.2011.20036.x

Bressan, A., Marigo, P., Girardi, L., et al. 2012, MNRAS, 427, 127, doi: 10.1111/j.1365-2966.2012.21948.x10.48550/arXiv.1208.4498

Cadelano, M., Ferraro, F. R., Dalessandro, E., et al. 2022, ApJ, 941, 69, doi: 10.3847/1538-4357/aca016

Cadelano, M., Saracino, S., Dalessandro, E., et al. 2020, ApJ, 895, 54, doi: 10.3847/1538-4357/ab88b310.48550/arXiv.2004.06131

Calzetti, D., de Marchi, G., Paresce, F., & Shara, M. 1993, ApJ, 402, L1, doi: 10.1086/186685

Capuzzo-Dolcetta, R., Spera, M., & Punzo, D. 2013, Journal of Computational Physics, 236, 580, doi: 10.1016/j.jcp.2012.11.013

Cardelli, J. A., Clayton, G. C., & Mathis, J. S. 1989, ApJ, 345, 245, doi: 10.1086/167900

Casagrande, L., & VandenBerg, D. A. 2014, MNRAS, 444, 392, doi: 10.1093/mnras/stu147610.48550/arXiv.1407.6095

Chaboyer, B. 1998, Phys. Rep., 307, 23, doi: 10.1016/S0370-1573(98)00054-4

Chatterjee, S., Fregeau, J. M., Umbreit, S., & Rasio, F. A. 2010, ApJ, 719, 915, doi: 10.1088/0004-637X/719/1/915

Chernoff, D. F., & Djorgovski, S. 1989, ApJ, 339, 904, doi: 10.1086/167344

Chernoff, D. F., & Shapiro, S. L. 1987, ApJ, 322, 113, doi: 10.1086/165708

Chernoff, D. F., & Weinberg, M. D. 1990, ApJ, 351, 121, doi: 10.1086/168451

Chomiuk, L., Strader, J., Maccarone, T. J., et al. 2013, ApJ, 777, 69, doi: 10.1088/0004-637X/777/1/69

Clarkson, W. I., Sahu, K. C., Anderson, J., et al. 2011, ApJ, 735, 37, doi: 10.1088/0004-637X/735/1/3710.48550/arXiv.1105.4176

Cohen, R. E., Bellini, A., Libralato, M., et al. 2021, AJ, 161, 41, doi: 10.3847/1538-3881/abd036

Cohn, H., Hut, P., & Wise, M. 1989, ApJ, 342, 814, doi: 10.1086/167638

Dalessandro, E., Ferraro, F. R., Massari, D., et al. 2013, ApJ, 778, 135, doi: 10.1088/0004-637X/778/2/135

Davies, M. B., & Hansen, B. M. S. 1998, MNRAS, 301, 15, doi: 10.1046/j.1365-8711.1998.01923.x

Djorgovski, S. 1993, in Astronomical Society of the Pacific Conference Series, Vol. 50, Structure and Dynamics of Globular Clusters, ed. S. G. Djorgovski & G. Meylan, 373

Djorgovski, S., & King, I. R. 1984, ApJ, 277, L49, doi: 10.1086/184200

—. 1986, ApJ, 305, L61, doi: 10.1086/184685

Djorgovski, S., & Meylan, G. 1994, AJ, 108, 1292, doi: 10.1086/117154

Dotter, A., Chaboyer, B., Jevremović, D., et al. 2008, ApJS, 178, 89, doi: 10.1086/58965410.48550/arXiv.0804.4473

Dresbach, F., Massari, D., Lanzoni, B., et al. 2022, ApJ, 928, 47, doi: 10.3847/1538-4357/ac5406

Ferraro, F. R., Clementini, G., Fusi Pecci, F., & Buonanno, R. 1991, MNRAS, 252, 357, doi: 10.1093/mnras/252.3.357

Ferraro, F. R., Clementini, G., Fusi Pecci, F., Sortino, R., & Buonanno, R. 1992a, MNRAS, 256, 391, doi: 10.1093/mnras/256.3.391

Ferraro, F. R., Fusi Pecci, F., & Buonanno, R. 1992b, MNRAS, 256, 376, doi: 10.1093/mnras/256.3.376

Ferraro, F. R., Lanzoni, B., & Dalessandro, E. 2020, Rendiconti Lincei. Scienze Fisiche e Naturali, 31, 19, doi: 10.1007/s12210-020-00873-2

Ferraro, F. R., Lanzoni, B., Dalessandro, E., et al. 2019, Nature Astronomy, 3, 1149, doi: 10.1038/s41550-019-0865-1

Ferraro, F. R., Massari, D., Dalessandro, E., et al. 2016, ApJ, 828, 75, doi: 10.3847/0004-637X/828/2/7510.48550/arXiv.1609.01515

Ferraro, F. R., Messineo, M., Fusi Pecci, F., et al. 1999a, AJ, 118, 1738, doi: 10.1086/30102910.48550/arXiv.astro-ph/9906248

Ferraro, F. R., Montegriffo, P., Origlia, L., & Fusi Pecci, F. 2000, AJ, 119, 1282, doi: 10.1086/30126910.48550/arXiv.astro-ph/9912265

Ferraro, F. R., Paltrinieri, B., Fusi Pecci, F., et al. 1997a, ApJ, 484, L145, doi: 10.1086/310780

Ferraro, F. R., Paltrinieri, B., Rood, R. T., & Dorman, B. 1999b, ApJ, 522, 983, doi: 10.1086/30770010.48550/arXiv.astro-ph/9904196

Ferraro, F. R., Possenti, A., Sabbi, E., et al. 2003, ApJ, 595, 179, doi: 10.1086/377352

Ferraro, F. R., Paltrinieri, B., Fusi Pecci, F., et al. 1997b, A&A, 324, 915. https://arxiv.org/abs/astro-ph/9703026

Ferraro, F. R., Beccari, G., Dalessandro, E., et al. 2009a, Nature, 462, 1028, doi: 10.1038/nature08607

Ferraro, F. R., Dalessandro, E., Mucciarelli, A., et al. 2009b, Nature, 462, 483, doi: 10.1038/nature08581

Ferraro, F. R., Lanzoni, B., Dalessandro, E., et al. 2012, Nature, 492, 393, doi: 10.1038/nature11686

Ferraro, F. R., Lanzoni, B., Raso, S., et al. 2018a, ApJ, 860, 36, doi: 10.3847/1538-4357/aac01c

Ferraro, F. R., Pallanca, C., Lanzoni, B., et al. 2021, Nature Astronomy, 5, 311, doi: 10.1038/s41550-020-01267-y10.48550/arXiv.2011.09966

Forbes, D. A., & Bridges, T. 2010, MNRAS, 404, 1203, doi: 10.1111/j.1365-2966.2010.16373.x

Fregeau, J. M., Cheung, P., Portegies Zwart, S. F., & Rasio, F. A. 2004, MNRAS, 352, 1, doi: 10.1111/j.1365-2966.2004.07914.x

Freire, P. C., Gupta, Y., Ransom, S. M., & Ishwara-Chandra, C. H. 2004, ApJ, 606, L53, doi: 10.1086/421085

Frogel, J. A., Stephens, A., Ramírez, S., & DePoy, D. L. 2001, AJ, 122, 1896, doi: 10.1086/32307910.48550/arXiv.astro-ph/0101275

Fukushige, T., & Heggie, D. C. 1995, MNRAS, 276, 206, doi: 10.1093/mnras/276.1.206

—. 2000, MNRAS, 318, 753, doi: 10.1046/j.1365-8711.2000.03811.x

Fusi Pecci, F., Ferraro, F. R., Crocker, D. A., Rood, R. T., & Buonanno, R. 1990, A&A, 238, 95

Gaia Collaboration, Brown, A. G. A., Vallenari, A., & Prusti. 2016a, A&A, 595, A2, doi: 10.1051/0004-6361/20162951210.48550/arXiv.1609.04172

Gaia Collaboration, Prusti, T., de Bruijne, J. H. J., & Brown. 2016b, A&A, 595, A1, doi: 10.1051/0004-6361/20162927210.48550/arXiv.1609.04153

Gieles, M., Erkal, D., Antonini, F., Balbinot, E., & Peñarrubia, J. 2021, Nature Astronomy, 5, 957, doi: 10.1038/s41550-021-01392-2

Giersz, M. 1998, MNRAS, 298, 1239, doi: 10.1046/j.1365-8711.1998.01734.x

—. 2001, MNRAS, 324, 218, doi: 10.1046/j.1365-8711.2001.04337.x

—. 2006, MNRAS, 371, 484, doi: 10.1111/j.1365-2966.2006.10693.x

Giersz, M., Askar, A., Klencki, J., & Morawski, J. 2019, arXiv e-prints, arXiv:1904.03591. https://arxiv.org/abs/1904.03591

Giersz, M., & Heggie, D. C. 1994, MNRAS, 268, 257, doi: 10.1093/mnras/268.1.257

Giersz, M., Heggie, D. C., & Hurley, J. R. 2008, MNRAS, 388, 429, doi: 10.1111/j.1365-2966.2008.13407.x

Giersz, M., Heggie, D. C., Hurley, J. R., & Hypki, A. 2013, Monthly Notices of the Royal Astronomical Society, 431, 2184, doi: 10.1093/mnras/stt307

Giersz, M., Leigh, N., Hypki, A., Lützgendorf, N., & Askar, A. 2015, MNRAS, 454, 3150, doi: 10.1093/mnras/stv2162

Giesers, B., Dreizler, S., Husser, T.-O., et al. 2018, MNRAS, 475, L15, doi: 10.1093/mnrasl/slx203

Giesers, B., Kamann, S., Dreizler, S., et al. 2019, A&A, 632, A3, doi: 10.1051/0004-6361/201936203

Goodman, J. 1987, ApJ, 313, 576, doi: 10.1086/164998

Gratton, R. G., Fusi Pecci, F., Carretta, E., et al. 1997, ApJ, 491, 749, doi: 10.1086/304987

Grindlay, J., Portegies Zwart, S., & McMillan, S. 2006, Nature Physics, 2, 116, doi: 10.1038/nphys214

Gustafsson, B., Edvardsson, B., Eriksson, K., et al. 2008, A&A, 486, 951, doi: 10.1051/0004-6361:20080972410.48550/arXiv.0805.0554

Harfst, S., Gualandris, A., Merritt, D., & Mikkola, S. 2008, MNRAS, 389, 2, doi: 10.1111/j.1365-2966.2008.13557.x

Harris, W. E. 1996, AJ, 112, 1487, doi: 10.1086/118116

Heggie, D., & Hut, P. 2003, The Gravitational Million-Body Problem: A Multidisciplinary Approach to Star Cluster Dynamics

Heggie, D. C. 1975, MNRAS, 173, 729, doi: 10.1093/mnras/173.3.729

—. 2014, MNRAS, 445, 3435, doi: 10.1093/mnras/stu1976

Heggie, D. C., Trenti, M., & Hut, P. 2006, MNRAS, 368, 677, doi: 10.1111/j.1365-2966.2006.10122.x

Hénon, M. 1961, Annales d'Astrophysique, 24, 369

—. 1964, Annales d'Astrophysique, 27, 83

Hénon, M. H. 1971, Ap&SS, 14, 151, doi: 10.1007/BF00649201

Hills, J. G., & Day, C. A. 1976, Astrophys. Lett., 17, 87

Hobbs, G., Lorimer, D. R., Lyne, A. G., & Kramer, M. 2005, Monthly Notices of the Royal Astronomical Society, 360, 974, doi: 10.1111/j.1365-2966.2005.09087.x

Hurley, J. R., Pols, O. R., & Tout, C. A. 2000, Monthly Notices of the Royal Astronomical Society, 315, 543, doi: 10.1046/j.1365-8711.2000.03426.x

Hurley, J. R., Tout, C. A., & Pols, O. R. 2002, Monthly Notices of the Royal Astronomical Society, 329, 897, doi: 10.1046/j.1365-8711.2002.05038.x

Hypki, A., & Giersz, M. 2013, MNRAS, 429, 1221, doi: 10.1093/mnras/sts415

Joshi, K. J., Rasio, F. A., & Portegies Zwart, S. 2000, ApJ, 540, 969, doi: 10.1086/309350

Kerber, L. O., Libralato, M., Souza, S. O., et al. 2019, MNRAS, 484, 5530, doi: 10.1093/mnras/stz00310.48550/arXiv.1901.03721

King, I. R. 1966, The Astronomical Journal, 71, 64

Kremer, K., Rui, N. Z., Weatherford, N. C., et al. 2021, ApJ, 917, 28, doi: 10.3847/1538-4357/ac06d4

Kremer, K., Ye, C. S., Rui, N. Z., et al. 2020, ApJS, 247, 48, doi: 10.3847/1538-4365/ab7919

Kroupa, P. 1995, MNRAS, 277, 1491, doi: 10.1093/mnras/277.4.1491

—. 2001, MNRAS, 322, 231

Kroupa, P., Weidner, C., Pflamm-Altenburg, J., et al. 2013, in Planets, Stars and Stellar Systems. Volume 5: Galactic Structure and Stellar Populations, ed. T. D. Oswalt & G. Gilmore, Vol. 5, 115, doi: 10.1007/978-94-007-5612-0_4

Kuchinski, L. E., & Frogel, J. A. 1995, AJ, 110, 2844, doi: 10.1086/117733

Kulkarni, S. R., Hut, P., & McMillan, S. 1993, Nature, 364, 421, doi: 10.1038/364421a0

Lanzoni, B., Dalessandro, E., Ferraro, F. R., et al. 2007a, ApJ, 663, 267, doi: 10.1086/51859210.48550/arXiv.0704.0139

—. 2007b, ApJ, 668, L139, doi: 10.1086/522927

Lanzoni, B., Ferraro, F. R., Alessandrini, E., et al. 2016, ApJ, 833, L29, doi: 10.3847/2041-8213/833/2/L29

Lanzoni, B., Sanna, N., Ferraro, F. R., et al. 2007c, ApJ, 663, 1040, doi: 10.1086/518688

Lanzoni, B., Ferraro, F. R., Dalessandro, E., et al. 2010, ApJ, 717, 653, doi: 10.1088/0004-637X/717/2/653

Lanzoni, B., Ferraro, F. R., Dalessandro, E., et al. 2019, The Astrophysical Journal, 887, 176, doi: 10.3847/1538-4357/ab54c2

Libralato, M., Bellini, A., Piotto, G., et al. 2019, ApJ, 873, 109, doi: 10.3847/1538-4357/ab0551

Libralato, M., Bellini, A., van der Marel, R. P., et al. 2018, ApJ, 861, 99, doi: 10.3847/1538-4357/aac6c0

Lugger, P. M., Cohn, H. N., & Grindlay, J. E. 1995, ApJ, 439, 191, doi: 10.1086/175164

Lützgendorf, N., Kissler-Patig, M., Gebhardt, K., et al. 2013, A&A, 552, A49, doi: 10.1051/0004-6361/201220307

Lynden-Bell, D. 1962, MNRAS, 124, 279, doi: 10.1093/mnras/124.4.279

Lynden-Bell, D. 1967, in Les Nouvelles Méthodes de la Dynamique Stellaire, 163

Mackey, A. D., & Gilmore, G. F. 2003, MNRAS, 338, 85, doi: 10.1046/j.1365-8711.2003.06021.x

Mackey, A. D., Wilkinson, M. I., Davies, M. B., & Gilmore, G. F. 2007, MNRAS, 379, L40, doi: 10.1111/j.1745-3933.2007.00330.x

—. 2008, MNRAS, 386, 65, doi: 10.1111/j.1365-2966.2008.13052.x

Madau, P., & Rees, M. J. 2001, ApJ, 551, L27, doi: 10.1086/319848

Maraston, C. 1998, MNRAS, 300, 872, doi: 10.1046/j.1365-8711.1998.01947.x

Marín-Franch, A., Aparicio, A., Piotto, G., et al. 2009, ApJ, 694, 1498, doi: 10.1088/0004-637X/694/2/1498

Massari, D., Mucciarelli, A., Ferraro, F. R., et al. 2014, ApJ, 795, 22, doi: 10.1088/0004-637X/795/1/2210.48550/arXiv.1409.1682

McCall, M. L. 2004, AJ, 128, 2144, doi: 10.1086/424933

McCrea, W. H. 1964, MNRAS, 128, 147, doi: 10.1093/mnras/128.2.147

McLaughlin, D. E., & van der Marel, R. P. 2005, ApJS, 161, 304, doi: 10.1086/49742910.48550/arXiv.astro-ph/0605132

McMillan, S., Portegies Zwart, S., van Elteren, A., & Whitehead, A. 2012, in Astronomical Society of the Pacific Conference Series, Vol. 453, Advances in Computational Astrophysics: Methods, Tools, and Outcome, ed. R. Capuzzo-Dolcetta, M. Limongi, & A. Tornambè, 129, doi: 10.48550/arXiv.1111.3987

Merritt, D., Piatek, S., Portegies Zwart, S., & Hemsendorf, M. 2004, ApJ, 608, L25, doi: 10.1086/422252

Meylan, G., & Heggie, D. C. 1997, A&A Rev., 8, 1, doi: 10.1007/s001590050008

Miller, M. C., & Hamilton, D. P. 2002, MNRAS, 330, 232, doi: 10.1046/j.1365-8711.2002.05112.x

Minniti, D. 1995, A&A, 303, 468

Miocchi, P. 2007, MNRAS, 381, 103, doi: 10.1111/j.1365-2966.2007.12165.x

Miocchi, P., Lanzoni, B., Ferraro, F. R., et al. 2013, The Astrophysical Journal, 774, 151, doi: 10.1088/0004-637x/774/2/151

Montegriffo, P., Ferraro, F. R., Fusi Pecci, F., & Origlia, L. 1995, MNRAS, 276, 739, doi: 10.1093/mnras/276.3.739

Morscher, M., Pattabiraman, B., Rodriguez, C., Rasio, F. A., & Umbreit, S. 2015, ApJ, 800, 9, doi: 10.1088/0004-637X/800/1/9

Muñoz, C., Villanova, S., Geisler, D., et al. 2017, A&A, 605, A12, doi: 10.1051/0004-6361/20173046810.48550/arXiv.1705.02684

Nataf, D. M., Gould, A. P., Pinsonneault, M. H., & Udalski, A. 2013a, ApJ, 766, 77, doi: 10.1088/0004-637X/766/2/7710.48550/arXiv.1109.2118

Nataf, D. M., Gould, A., Fouqué, P., et al. 2013b, ApJ, 769, 88, doi: 10.1088/0004-637X/769/2/8810.48550/arXiv.1208.1263

Noyola, E., & Baumgardt, H. 2011, ApJ, 743, 52, doi: 10.1088/0004-637X/743/1/52

Noyola, E., & Gebhardt, K. 2006, AJ, 132, 447, doi: 10.1086/50539010.48550/arXiv.astro-ph/0604251

O'Leary, R. M., Rasio, F. A., Fregeau, J. M., Ivanova, N., & O'Shaughnessy, R. 2006, ApJ, 637, 937, doi: 10.1086/498446

Oliveira, R. A. P., Souza, S. O., Kerber, L. O., et al. 2020, ApJ, 891, 37, doi: 10.3847/1538-4357/ab6f7610.48550/arXiv.2001.08611

Origlia, L., Ferraro, F. R., Fusi Pecci, F., & Oliva, E. 1997, A&A, 321, 859

Origlia, L., Lena, S., Diolaiti, E., et al. 2008a, ApJ, 687, L79, doi: 10.1086/59335110.48550/arXiv.0809.3939

Origlia, L., Valenti, E., & Rich, R. M. 2008b, MNRAS, 388, 1419, doi: 10.1111/j.1365-2966.2008.13492.x10.48550/arXiv.0805.3442

Origlia, L., Rich, R. M., Ferraro, F. R., et al. 2011, ApJ, 726, L20, doi: 10.1088/2041-8205/726/2/L2010.48550/arXiv.1012.2047

Ortolani, S., Barbuy, B., & Bica, E. 1994, A&AS, 108, 653

Pallanca, C., Ferraro, F. R., Lanzoni, B., et al. 2019, ApJ, 882, 159, doi: 10.3847/1538-4357/ab35db10.48550/arXiv.1908.09708

Pallanca, C., Lanzoni, B., Ferraro, F. R., et al. 2021, ApJ, 913, 137, doi: 10.3847/1538-4357/abf93810.48550/arXiv.2104.09362

Pfahl, E., Rappaport, S., & Podsiadlowski, P. 2002, ApJ, 573, 283, doi: 10.1086/340494

Picard, A., & Johnston, H. M. 1995, A&AS, 112, 89

Pooley, D., Lewin, W. H. G., Anderson, S. F., et al. 2003, ApJ, 591, L131, doi: 10.1086/377074

Popowski, P. 2000, ApJ, 528, L9, doi: 10.1086/31242610.48550/arXiv.astro-ph/9910174

Portegies Zwart, S. 2019, A&A, 621, L10, doi: 10.1051/0004-6361/201833485

Portegies Zwart, S. F., Hut, P., Makino, J., & McMillan, S. L. W. 1998, A&A, 337, 363. https://arxiv.org/abs/astro-ph/9803084

Ransom, S. M., Hessels, J. W. T., Stairs, I. H., et al. 2005, Science, 307, 892, doi: 10.1126/science.1108632

Rantala, A., Naab, T., & Springel, V. 2021, MNRAS, 502, 5546, doi: 10.1093/mnras/stab057

Raso, S., Ferraro, F. R., Dalessandro, E., et al. 2017, ApJ, 839, 64, doi: 10.3847/1538-4357/aa689110.48550/arXiv.1704.01453

Repetto, S., Davies, M. B., & Sigurdsson, S. 2012, MNRAS, 425, 2799, doi: 10.1111/j.1365-2966.2012.21549.x

Riello, M., Cassisi, S., Piotto, G., et al. 2003, A&A, 410, 553, doi: 10.1051/0004-6361:2003127210.48550/arXiv.astro-ph/0308431

Rodriguez, C. L., Chatterjee, S., & Rasio, F. A. 2016a, Phys. Rev. D, 93, 084029, doi: 10.1103/PhysRevD.93.084029

Rodriguez, C. L., Morscher, M., Wang, L., et al. 2016b, MNRAS, 463, 2109, doi: 10.1093/mnras/stw2121

Salinas, R., Jílková, L., Carraro, G., Catelan, M., & Amigo, P. 2012, MNRAS, 421, 960, doi: 10.1111/j.1365-2966.2011.20354.x10.48550/arXiv.1112.1614

Santos, João F. C., J., Maia, F. F. S., Dias, B., et al. 2020, MNRAS, 498, 205, doi: 10.1093/mnras/staa242510.48550/arXiv.2008.04399

Saracino, S., Dalessandro, E., Ferraro, F. R., et al. 2015, ApJ, 806, 152, doi: 10.1088/0004-637X/806/2/152

—. 2016, ApJ, 832, 48, doi: 10.3847/0004-637X/832/1/4810.48550/arXiv.1609.02152

—. 2019, ApJ, 874, 86, doi: 10.3847/1538-4357/ab07c410.48550/arXiv.1902.05558

Sigurdsson, S., & Hernquist, L. 1993, Nature, 364, 423, doi: 10.1038/364423a0

Sills, A., Lombardi, James C., J., Bailyn, C. D., et al. 1997, ApJ, 487, 290, doi: 10.1086/304588

Sippel, A. C., & Hurley, J. R. 2013, MNRAS, 430, L30, doi: 10.1093/mnrasl/sls044

Spitzer, Lyman, J. 1969, ApJ, 158, L139, doi: 10.1086/180451

Spitzer, L. 1987, Dynamical evolution of globular clusters (Princeton University Press)

Stetson, P. B. 1987, PASP, 99, 191, doi: 10.1086/131977

—. 1994, PASP, 106, 250, doi: 10.1086/133378

Stodolkiewicz, J. S. 1982, Acta Astron., 32, 63

—. 1986, Acta Astron., 36, 19

Strader, J., Chomiuk, L., Maccarone, T. J., Miller-Jones, J. C. A., & Seth, A. C. 2012, Nature, 490, 71, doi: 10.1038/nature11490

Tiongco, M. A., Vesperini, E., & Varri, A. L. 2016, MNRAS, 461, 402, doi: 10.1093/mnras/stw1341

Trenti, M., Heggie, D. C., & Hut, P. 2007, MNRAS, 374, 344, doi: 10.1111/j.1365-2966.2006.11166.x

Trenti, M., Vesperini, E., & Pasquato, M. 2010, ApJ, 708, 1598, doi: 10.1088/0004-637X/708/2/1598

Udalski, A. 2003, ApJ, 590, 284, doi: 10.1086/37486110.48550/arXiv.astro-ph/0210367

Valenti, E., Ferraro, F. R., & Origlia, L. 2004a, MNRAS, 351, 1204, doi: 10.1111/j.1365-2966.2004.07861.x10.48550/arXiv.astro-ph/0403563

—. 2004b, MNRAS, 354, 815, doi: 10.1111/j.1365-2966.2004.08249.x10.48550/arXiv.astro-ph/0404403

Valenti, E., Zoccali, M., Renzini, A., et al. 2013, A&A, 559, A98, doi: 10.1051/0004-6361/20132196210.48550/arXiv.1309.4570

Verbunt, F., & Freire, P. C. C. 2014, A&A, 561, A11, doi: 10.1051/0004-6361/20132117710.48550/arXiv.1310.4669

Vesperini, E. 2010, Philosophical Transactions of the Royal Society of London Series A, 368, 829, doi: 10.1098/rsta.2009.0260

Vesperini, E., & Chernoff, D. F. 1994, ApJ, 431, 231, doi: 10.1086/174480

Vesperini, E., & Heggie, D. C. 1997, MNRAS, 289, 898, doi: 10.1093/mnras/289.4.898

Vesperini, E., & Trenti, M. 2010, ApJ, 720, L179, doi: 10.1088/2041-8205/720/2/L179

Wang, L., Spurzem, R., Aarseth, S., et al. 2015, MNRAS, 450, 4070, doi: 10.1093/mnras/stv817

—. 2016, MNRAS, 458, 1450, doi: 10.1093/mnras/stw274

Webb, J. J., & Vesperini, E. 2017, MNRAS, 464, 1977, doi: 10.1093/mnras/stw2513

Wilson, C. P. 1975, AJ, 80, 175, doi: 10.1086/111729

Ye, C. S., Fong, W.-f., Kremer, K., et al. 2020, ApJ, 888, L10, doi: 10.3847/2041-8213/ab5dc5

Zoccali, M., Cassisi, S., Piotto, G., Bono, G., & Salaris, M. 1999, ApJ, 518, L49, doi: 10.1086/31206410.48550/arXiv.astro-ph/9904183

Zoccali, M., Renzini, A., Ortolani, S., et al. 2003, A&A, 399, 931, doi: 10.1051/0004-6361:2002160410.48550/arXiv.astro-ph/0210660